TERAHERTZ FOR SUBSURFACE IMAGING AND METROLOGY APPLICATIONS

Dinh Thi NGUYEN

Submitted for the degree of Doctor of Philosophy

Heriot-Watt University

School of Engineering and Physical Sciences

Institute of Photonics and Quantum Sciences

September 2015

ABSTRACT

In the area of metrology and non-destructive testing, Terahertz wavelengths have been widely researched and used. However, the lack of 2D detectors working at room temperature and high power sources prevent the widespread application of Terahertz in industry. In that context, research on the development of new Terahertz equipment is moving at a fast pace. Within the scope of this thesis, applications of newly developed Terahertz technologies were explored using the scanning of single point detectors with the objective to establish the feasibility for their full-field applications in readiness for future 2D detectors. For the first time, a frequency tuneable, all-optical Terahertz source was implemented in multi-wavelength interferometry to overcome one wavelength ambiguity in precise thickness/distance measurements with sub-millimetre resolution. Phase-shifting digital holography is another interferometry technique which allows us to reconstruct not only the amplitude of one object, but also the phase and the depth of it, using existing mathematical algorithms. Digital holography was performed successfully at Terahertz wavelengths using a multiplier/mixer Terahertz source coupled with a single point pyroelectric detector for the applications of non-destructive testing and depth measurements. The novelty is that the phase-stepping technique for digital holography was implemented in THz frequencies for the first time to remove unwanted terms in the reconstructed image in order to improve image quality compare to conventional holography. In the current experiments, recording time for one set of phase-shifting holograms (4 holograms for 4 phase-steps algorithm) was 6 hours. When the technology is ready for 2D detectors, recording time of holograms could be reduced considerably, and the technique will play an important role in full-field applications in industry metrology and/or non-destructive testing and evaluation.

DEDICATION

To my daughter Lily,

my husband Viet,

and my parents

ACKNOWLEDGEMENT

I would like to express my sincere gratitude to my supervisor prof. Andrew J. Moore for his continuous support and encouragement during my PhD research and thesis writing. His immense knowledge and guidance helped me to overcome many challenges and sharpen the arguments of my research. Thank you very much for your patience, for all the ideas and helpful suggestions that I got.

My special thanks go to the Optical Diagnostic group members for the time working together in the lab, for the long conversations regarding the subjects of Physics and Optics. Without their help I would not be able to pass the first year of my PhD with enough acquired knowledge for the next years.

I also would like to thank to all the members of the Applied Optics and Photonics group for their help and support, for the “tea/coffee and donuts” chatting times and many other unforgettable memories.

I acknowledge the support of the staff and technicians of the Mechanical workshop for the quick processing of my orders and requests.

I thank the EPSRC for funding this work.

My great thank goes to my husband who has supported me in every aspect of life and in every decision that I have made. I thank Lily for being the source of my energy and motivation!

Finally, I would like to express my grateful to my parents who gave birth to me and grew me up to be who I am. I am deeply indebted to them.

ACADEMIC REGISTRY
Research Thesis Submission

Name*:*	Dinh Thi NGUYEN		
School/PGI:	EPS / IPaQS		
Version: *(i.e. First, Resubmission, Final)*	First	Degree Sought (Award **and** Subject area)	Doctor of Philosophy in Mechanical Engineering

Declaration

In accordance with the appropriate regulations I hereby submit my thesis and I declare that:

1) the thesis embodies the results of my own work and has been composed by myself
2) where appropriate, I have made acknowledgement of the work of others and have made reference to work carried out in collaboration with other persons
3) the thesis is the correct version of the thesis for submission and is the same version as any electronic versions submitted*.
4) my thesis for the award referred to, deposited in the Heriot-Watt University Library, should be made available for loan or photocopying and be available via the Institutional Repository, subject to such conditions as the Librarian may require
5) I understand that as a student of the University I am required to abide by the Regulations of the University and to conform to its discipline.

* *Please note that it is the responsibility of the candidate to ensure that the correct version of the thesis is submitted.*

Signature of Candidate*:*		Date:	

Submission

Submitted By *(name in capitals):*	DINH THI NGUYEN
Signature of Individual Submitting:	
Date Submitted:	

For Completion in the Student Service Centre (SSC)

Received in the SSC by *(name in capitals):*			
Method of Submission *(Handed in to SSC; posted through internal/external mail):*			
*E-thesis Submitted (**mandatory for final theses**)*			
Signature:		Date:	

Table of Contents

Abbreviation and Glossary

THz	: Terahertz
THz-TDS	: Terahertz time domain spectroscopy
OPO	: Optical parametric oscillator
OPTL	: Optically pumped Terahertz laser
FIRL	: Optically pumped far infrared laser
BWO	: Backward wave oscillator
PC	: Photoconductive antenna
EO	: Electro-optic
QCL(s)	: Quantum cascade laser(s)
DFG	: Different frequency generation
RTD	: Resonant tunnelling diode
IMPATT	: Impact ionisation avalanche transit-time diode
NDR	: Negative differential resistance
MMIC	: Microwave monolithic integrated circuit
TUNNET	: Tunnel injection transit time
MgO:$LiNbO_3$	: Magnesium Doped *Lithium Niobate*
Nd:YAG	: Neodymium-doped yttrium
NDT	: Non-destructive testing
DHI	: Digital holographic interferometry
LT-GaAs	: Low temperature grown GaAs
ZnTe	: Zinc Telluride
GaP	: Gallium phosphide
YSZ	: Yttria Stabilized Zirconia
YTZP	: Yttria Tetragonal Zirconia Polycrystal
MgPSZ	: Magnesia Partially Stabilized Zirconia
CCD	: Charge-coupled device
CMOS	: Complementary metal–oxide–semiconductor
Teflon	: Tetra-polyethylene
SNR	: Signal-to-noise ratio
CW	: Continuous wave
LO	: Local oscillator
RF	: Radio frequency

UV	: Ultraviolet
IR	: Infrared
IF	: Intermediate frequency
1D/ 2D/ 3D	: One dimensional/ Two dimensional/ Three dimensional
LIA	: Lock-in amplifier
NA	: Numerical aperture
SD	: Standard deviation
rms	: Root mean square
ms	: Millisecond
ps	: Pico-second
fs	: femto-second
μwave	: Microwave
μW / mW / kW	: Microwatt / Milliwatt / Kilowatt
UCA	: User Controlled Attenuation
MTF	: Modulation transfer function
C_f	: Contrast at one specific frequency
I_{mod}	: Modulation amplitude
λ	: Wavelength (lamda)
π	: pi number
M	: Magnification
NA_{obj}	: Numerical aperture of the objective
n_g	: Group refractive index
$\Delta\phi$	: Phase difference
dB	: Decibel
dBm	: Decibel-milliwatts
GUI	: Graphical User interface
I_{OB} / I_{RB}	: Object / Reference beam intensity
δ_ϕ	: Phase noise
δ_I	: Intensity noise
θ	: Theta angle
DC / AC	: Direct current / Alternative current

Chapter 1

INTRODUCTION

In the area of metrology and non-destructive testing, THz wavelengths have been widely researched and used. The potential advantages of THz radiation are well-known. Many common non-polar materials are semi-transparent at THz wavelengths including silicon, plastics, paper, cardboard, wood and clothing. The wavelength is long enough to avoid harmful ionising effects but short enough to provide sub-millimetre resolution for many imaging applications. Strong characteristic absorption wavelengths enable spectroscopic identification of specimens whilst polar liquids (e.g. water) and metals are opaque.

Although the term "terahertz technology" has appeared only recently, it has an older history than that but being identified by different names in the past, such as submillimetre wave, far infrared or T-Ray. Since the very first publications reported studies on the THz applications around the 1970s [1-2], the state of the art of THz measuring systems and their applications has advanced exponentially despite the relatively short period of only ~ 40 years. For example, just a decade later in the 1980s, THz optical rectification and photoconduction had been developed, which made it possible to generate very short THz pulses and detect it coherently in a system called "terahertz time domain spectroscopy" (THz-TDS) by using a single exciting laser [3-5]. This definitive progress generated a great deal of interest, which has been followed by many applications of THz-TDS in spectroscopy [6-8], imaging [9-10], medical diagnostics [11-13], metrology [10, 14], etc.

Even though the THz-TDS has become the most widely used technique so far, it still contains several limited aspects which relate to the low output power and slow imaging speed if spectroscopic information is not required. This limitation directs other efforts of the research community to develop new technology, methods and techniques for new applications in this domain. During the last 10 years, there have been rapid changes in THz technology, with new sources and detectors just becoming available

[15-16] (Appendix A.1 - A.4), opening up new fields of application. THz optical parametric oscillator (OPO) was invented in 1996 [17-18] and it is an all optical source, with a continuously tuneable range, from 1.03 – 2.14 THz and was then improved to 0.7 – 2.5 THz in a better, and more effective intra-cavity OPO [19]. The appearance of the new laser widely tuneable with higher intensity (μW) and a narrow-band output (THz-TDSs output is broadband) provides a wider choice for a large range of applications [20-23].

From the other side of the electromagnetic spectrum, microwave all-electronic sources seem to be the "wrong" direction for THz high spatial resolution because of the difficulties to extend to higher frequencies from the already established instruments [24-25]. However, THz-multipliers have made the long steps converting up from microwave frequencies to reach 200 GHz and up to 2.7 THz using two or more oscillation diodes [26-29]. Compactness, effective, low cost and room temperature operation, the THz-multipliers are rapidly growing in application range. Heimbeck et al. [30] used a 0.66 – 0.76 tuneable THz- multipliers source in a Mach-Zehnder interferometer setup for phase measurement application using off-axis digital holography and dual-wavelength reconstruction method. However, spatial filtering needs to be applied to remove the unwanted image orders, so it limits the resolution. Also using a THz-multiplier source operated at 360 GHz for phase measurement, Peter Foldesy [31] reported another approach to phase measurement by capturing the combined polarization of two orthogonally polarized reference and object waves to reconstruct the object phase based on the known phase-shift (90^o) between them.

Each type of THz source has its own advantages and disadvantages, with regard to their output power, room-temperature operation, cost effectiveness and wavelength tuneability [32]. To better understand the methods used, a general review along with the needed tools will be provided. Although metrology applications with THz have been widely studied, most of them used THz-TDS and/or single point scanning detector. The only report which used a 2D microbolometer array detector also used a free electron laser which generates very high output power that can be detected by the 2D detector without the need of cryogenic cooling [33]. The laser and the detector are too expensive to be applicable in normal applications and much less in industrial applications. The current lack of 2D detectors working at room temperature and high power sources restrict the wider application of THz metrology. Research on developing new THz equipment and exploring potential applications of the new THz technologies are moving

parallel in a fast pace. In the context of this research direction, the main contribution of this thesis is to explore the potential applications of newly available sources and single point detectors but the objective is to establish the feasibility for their full-field applications in readiness for future 2D detectors.

Within the thesis, the ability of using an all-optical THz intra-cavity OPO source in thickness measurement of opaque objects and in NDT of internal defects is demonstrated. The spectroscopic frequency scanning ability of THz OPO was also used to test the transmission properties of some materials for future interest. The thickness measurement and NDT of internal defects was undertaken for the first time using an all-optical THz source and these measurements have shown a correspondence between the measured and expected values. Unfortunately, instabilities in the THz OPO source meant that it was not suitable for interferometric phase measurements. Therefore a more traditional THz-multiplier source was used to demonstrate THz metrology techniques and potential applications, together with a pyroelectric detector. The output beam was fully characterised which enabled the spatial and axial resolutions of an imaging system to be predicted. Clearly this resolution is not as high as could potentially be achieved at higher THz frequencies (for example with the THz-OPO) but it enabled the principles to be established. Very few publications can be found in the literature that address digital holography at THz frequencies and no studies on THz phase-shifting digital holographic interferometry (DHI) have been published. In this thesis, phase-shifting digital holographic interferometry technique was implemented in THz regime for the first time, in which both intensity and phase reconstruction will be presented. Potential applications are for 3D imaging, NDT of internal defect and for thickness measurement.

This thesis is written in 6 chapters. The following chapter (Chapter 2) provides the basic foundation and the literature reviews. Chapter 3 covers the issues related to the use of a THz intra-cavity OPO laser, including for single point thickness measurement. Chapter 4 is devoted to the characterisation of the THz-multiplier source, and the investigation of some initial applications made with it, including full-field thickness measurements with a scanned single-point detector. Chapter 5 focuses on studying THz phase-shifting digital holographic interferometry using a THz-multiplier source where the technique is demonstrated at THz wavelength for the first time. The final conclusion of the thesis is presented in Chapter 6.

Chapter 2

LITERATURE REVIEW

2.1. THz REVIEW

In the electromagnetic spectrum, the terahertz (THz) region is defined as a gap between the millimetre wave and the infrared. In some papers [34-35], this region is placed in a range between 0.1 THz (10^{11} Hz) and 10 THz (10^{13} Hz); in other sources [36-37], this range is narrowed from 0.3 to 3 THz. We would define the THz range between 0.1- 10 THz (wavelength range between 0.03 mm to 3 mm) as it covers almost all the defined ranges in literature about THz. ***Figure 2.1*** shows the THz region in the electromagnetic spectrum. THz waves also have other names. As it is situated between microwaves and infrared, the radio frequency community call it submillimetre waves, the optical community call it far-infrared waves.

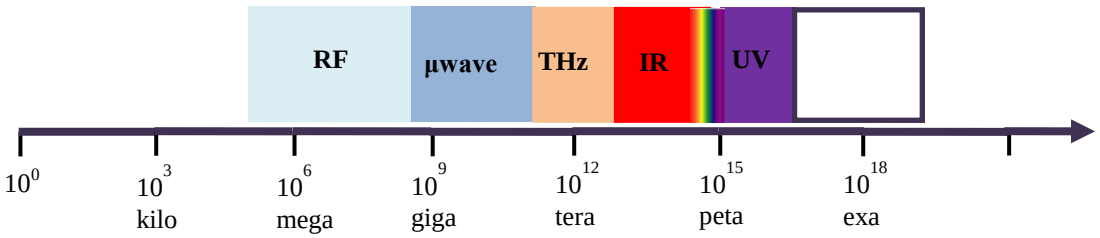

Figure 2.1. THz in the electromagnetic spectrum: RF is radio frequencies, μwave is microwave, IR is infrared, and UV is ultraviolet

The position of the THz region in the electromagnetic spectrum causes the THz radiation to possess the mixed properties of its neighbours (electronic and photonic domain). Among those properties, there are three major factors that make THz attractive to researchers: First of all, most non-metallic and non-polar materials are transparent at THz wavelengths, including silicon, plastics, paper, cardboard, wood, clothing, etc. This property opens up some potential applications for THz, such as metrology, non-

destructive testing or security checking. Secondly, strong characteristic absorption wavelengths enable the spectroscopic identification of specimens, whilst polar liquids (e.g. water) and metals are opaque. The wavelength is long enough to avoid harmful ionising effects, but short enough to provide sub-millimetre spatial resolution for many imaging applications. In addition, THz radiation is strongly absorbed by water in some windows of the range. Therefore in some applications, care needs to be taken to choose THz wavelengths to avoid water absorption caused by the moisture in the air to improve the signal-to-noise ratio (SNR) of the system.

THz technology focuses on developing effective THz sources and detectors for full field applications. In this chapter, an overview of the status of THz sources, THz detectors and their applications will be presented. In the following section and subsections, the categories of THz source and detector are introduced. At the end of each section, the suitability of the presented technology for individual application will be discussed. Then the potential metrology applications using the various introduced sources are reported in the final section.

2.2. THz SOURCES

A black-body emits THz radiation as part of its emitted spectrum. This phenomenon is demonstrated in the well-known Plank's law. So any heated source can be a THz source. However, this method to generate THz radiation is extremely ineffective because the thermal emission is very weak.

The technologies for THz sources are mainly based on two approaches, which are from its microwave and IR/photonic neighbouring regions. Therefore, the THz source technology will be separated into: vacuum tube sources, microwave technology based sources, optical based sources and hybrid techniques. These separated categories are managed to introduce in the following subsections.

2.2.1. Vacuum Electronics Based Sources

This type of source generates a monochromatic or broadband THz beam. The common design for this type of source is a vacuum tube, in which electron beams are accelerated while travelling inside, normally under a strong magnetic field. The physical principle for the THz emission in this case is based on the Maxwell's law, in classical electrodynamics, regarding moving charges. Consider an electron which is moving in free space. If it moves at a constant velocity, the field moves along with it, but does not

propagate: the electron does not radiate. Otherwise, when the electron is moving with acceleration, it produces an electromagnetic field that travels outward from its position. This electromagnetic wave carries energy and momentum away from the electron.

Among the THz sources of this type, there are the THz Synchrotron sources [38-40] which generate broadband THz radiation, or free electron lasers (FELs) [41] which generate a monochromatic, broadly tuneable THz beam. These sources offer very high output power (W to kW) but are bulky (building- sized), and very expensive (for the source itself and for their running costs). For these reasons, they are only available in very few laboratories in the world. For example the world's smallest Synchrotron MIRRORCLE-6X in Japan; the extremely high power ALICE synchrotron at the Daresbury Laboratory in Cheshire, England; the Dutch free electron laser FELIX in Utrecht, etc.

The backward wave oscillator (BWO) is another example of this type of source [42-43]. It is monochromatic, tuneable and compact, but generates a much lower output power (μW to mW) and only low frequencies (typically < 1 THz). Recently developed BWOs can reach 1.2 THz and are commercially available (Appendix A.5).

2.2.2. Microwave Technology

Many approaches have been applied to achieve an increase in frequency conversion up from millimetre wavelengths to THz frequencies. A valuable review about this THz technology is recommended in [37]. Even though it was written about 10 years ago, most information still holds true with all relevant updates to the THz technology.

There are many methods and techniques used which the most common ones are taken into account here such as: Gunn diodes [44], impact ionisation avalanche transit-time diode (IMPATT) diodes [45], and resonant tunnelling diodes (RTDs) [37]. A common factor in the operation of these diodes is that they are two terminal devices [25] operating under current-voltage relationships, particularly a negative differential resistance (NDR). For example, RTD [46-47] is formed of a single quantum well structure surrounded by very thin barrier layers. In a relaxing state, charge carriers (electrons) cannot transmit through the barriers. When a voltage is placed across a RTD, charge carriers "tunnel" through the well and emit THz wave when they go back to the valance band. This phenomenon is called the resonant tunnelling effect. THz photon energy is then equal to the energy value inside the quantum well.

These sources are compact, and efficient, but work at low frequencies only. The IMPATT and Gunn diodes produce ~ 50- 100 mW at 100 GHz, can reach a maximum of 140 GHz and are commercially available (Appendix A.1). Higher frequencies can be obtained by frequency multiplication, but at the expense of a significant reduction in power [48].

There are some other recently developed sources for THz such as microwave monolithic integrated circuit (MMIC) [49], or tunnel injection transit time (TUNNET). MMICs already can extend to 1 THz operation frequency but at very low power (***Figure 2.3*** below in page 12).

Frequency-multiplier from microwave synthesisers (20-40 GHz) is also another low-cost, but effective method to reach THz frequencies. This type of source will be used in experiments in Chapter 4 and Chapter 5 of this thesis. Current technology of THz-multiplier can generate frequencies as high as 2.5-2.7 THz at 4 μW [28, 50], 1.9 THz at 3 μW [27], 1.5 THz at 15 μW [51], 1.2 THz at 100 μW [26], all at room temperature operation. The powers can be improved, if working at low temperature [52].

2.2.3. Optical Based Sources

Optical based sources are more modern compared to those that come from the microwave side of the THz gap. Optically pumped THz laser (OPTL) and THz optical parametric oscillator (THz- OPO) are the most effective and commonly used as all-optical THz sources. Lead salt laser is another example, but it operates at a higher frequency range (> 10 THz) and needs cryogenic operation.

An OPTL, also known as a gas laser or a far infrared laser, is analogous to a conventional laser, in that, an optical field is applied to a gain medium, in this case is a gas, and causing it to become excited. The excited state then relaxes back through the emission of a photon. When the gain medium is located within a resonator, the feedback of the THz field results in the emission process becoming stimulated and hence a beam of high spatial quality and temporal coherence is obtained. A detailed description of this type of laser is written in a report from Coherent [16], and a good review by the same author can be found in [53]. OPTLs operate at discrete frequencies and in CW mode only, ranging from about 0.3 THz to 10 THz depending on model. Power levels of 1-20 mW and higher are common, depending on the chosen line. The laser has a long lifetime and is reliable and rugged; it is also commercially available and supplied by

DEOS, Edinburgh Instruments and MPB technologies. However, the laser is bulky and expensive for popular applications.

Parametric generation techniques were reported in the late 1960s to 1970s. The interaction is efficient, but most of the generated THz absorbed or totally reflected inside the nonlinear crystal, due to the large absorption coefficient and a large refractive index (~ 5.2 in the THz range). In 1996, K. Kawase et al. introduced a grating coupler (precisely cut with a cutting saw), on the $LiNbO_3$ crystal surface, to couple out the THz wave directly to free air [17-18]. Changing the incident angle of the pump by 1^o tunes the THz wave in range 1.03- 2.14 THz. Later, they improved the system by introducing a better rotating stage, coupled with the Si prism for an output range tuning of 0.91- 3 THz [54]. Advantages of the THz parametric oscillator are a combination of room temperature operation, wide tuneability and narrow linewidth [55-56]. A review of the group's work with this laser is published in [57].

In a publication in 2006, Malcolm Dunn and his group from the University of St Andrews improved Kawase's approach by introducing a novel intersecting cavity design that enables the nonlinear crystal $MgO:LiNbO_3$ to be placed within the cavity of the pump laser [19]. This improvement reduces the required pump energy by an order of magnitude which enables pumping with a more compact and efficient diode laser. The laser produces THz pulses of 1 W peak power and 5 nJ output energy, which is an order of magnitude higher compared to the extra-cavity devices. The spectral bandwidth of ~ 100 GHz was subsequently reduced to 1 GHz [58], and then to 100 MHz [59] and the nonlinear medium was improved for a more efficient generation of THz.

THz intra-cavity OPO has recently been made commercially available by M Squared Lasers. In Chapter 3 of this thesis, experiments were performed using a laser borrowed from the company as well as a development system at St Andrews University.

Figure 2.2 shows the schematic details of the M-squared laser. A Q-switched, Nd:YAG laser provided the pump-wave for the parametric oscillator. The Nd:YAG laser gain crystal was end-pumped by a fibre-coupled, quasi-continuous-wave diode laser operating at a wavelength of 808 nm. Standard quarter-wave Q-switching using an electro-optic Q-switch (QS) in combination with a quarter-wave plate ($\lambda/4$) and a linear polariser (P) produced pump-wave pulses of a typical duration of 10–20 ns. The Nd:YAG laser cavity is defined by mirrors M1 and M2. The nonlinear medium $Mg:LiNO_3$ providing the parametric gain was located within the pump laser cavity and the parametric oscillator cavity is defined by mirrors M3 and M4. A silicon prism array

attached to one side of the nonlinear medium coupled the terahertz output into free-space.

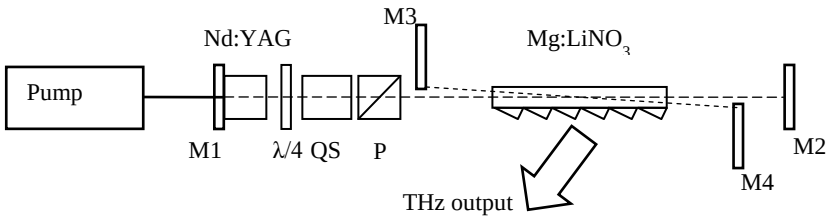

Figure 2.2. Schematic of the intra-cavity optical parametric THz laser.

The THz output frequency was adjusted by rotating mirrors M3 and M4 together to modify the angle between the idler-wave cavity and the pump-wave cavity: continuous wavelength selectivity in the range 0.7 to 2.5 THz was achieved by changing the angle of the pump beam in the non-linear crystal.

2.2.4. Hybrid Techniques

There are hybrid techniques for generating and detecting of THz radiation by both optically pumping and through electrical processing. Such sources coupled with the detecting of THz signal, both are by intense picosecond optical laser pulses, are commonly used in THz time domain spectroscopy (THz-TDS). As the generation and detection are used together, this section describes the full system including both the generating and detecting processes. There are two main techniques used in THz- TDS systems which are photoconductive antennas (PC) and the so-called electro-optic (EO) technique based on optical rectification.

Photoconductive antennas operate based on the Auston switch. Auston first reported an observation of producing a short electrical pulse by focusing intense picosecond (ps) optical radiation onto a $LiTaO_3Cu^{++}$ crystal. This observation is an optical rectification phenomenon but on an ion-doped polar crystal and by ultrashort laser pulse and resulted in an ultrashort electrical pulse [60-61]. Auston later was able to explain the phenomena theoretically [3, 62] and introduced the idea of using photoconductors instead of ion doped crystals for more efficient in generating signal [5]. The improvement in designing and searching for new materials led to the appearance of thin film low temperature grown GaAs (LT-GaAs) substrate coupled with

dipole antennas design [4, 63-64] which are commonly used nowadays. Typically in THz-TDS system by PC, an ultrashort laser beam is split into two beams which one of them is scanned through an optical delay line to gate coherently the generation and detection of THz beam in known phase. For the generation, one laser beam is incident to the photoconductor area of the PC. The photon energy is absorbed to create free electric charge carriers which are accelerated under electrical field of a bias voltage applied between the two dipole antennas. The acceleration of the electric charges results in the emission of a broadband electro-magnetic wave which covers the THz frequencies. The photoconductor material is chosen to have very short relaxation time (1 ps for LT-GaAs). For the detection, the electric charge carriers are created by shining of the second laser beam on the photoconductor area of a second PC. These charge carriers are driven by the electrical field of the incident THz beam and creates a current which the intensity can be measured by an ammeter placed between two dipoles of the second PC. By scanning mechanically the optical delay line of the detection laser beam, one can measure the intensity of the THz pulses at every known phase (which is later converted into time). Fourier transforming these THz time-domain pulses results in the frequency spectrum of the detected THz beam. This approach of generating and detecting of ultrafast electrical pulses by photoconductive antennas is known as "Auston Switch". A good historical review about this technique can be found in [65].

The electro-optic technique also uses ultrashort optical pulses for generating and detecting THz radiation, but by another effect. The generation is based on optical rectification [66] in an appropriate THz nonlinear crystal by intense optical pulses excitation [67-68]. Typical materials are zinc telluride (ZnTe), gallium phosphide (GaP), and gallium selenide (GaSe). The detecting process is called electro-optical sampling, which is based on the electro-optic Pockels effect in a THz birefringent material, typically by the same material used for emission. Nice historical review on this technique can be found in a recently written series by Siegel [69-70].

The photoconductive antennas are more "microwave/RF" type whereas the electro-optic follows a kind of all-optical approach. The generated THz radiation in TDS system is very broadband which covers a wide range from ~ 0.1 – 4 THz. The detection in THz-TDS is sensitive and coherent, which means that it can detect both the amplitude and the phase of the THz pulses. However, the emitted intensity is very low and the technique requires expensive intense ultrashort pumped lasers. THz-TDS has

been heavily developed and is dominant in most THz applications, from spectroscopy [71] to imaging [9-10].

2.2.5. Quantum Cascade Lasers

Quantum cascade lasers (QCLs) were first demonstrated in 1994 [72] but the operation frequency was in IR region at 71 THz. The laser is designed with multilayer of periodic thin film semiconductors to create many quantum wells along the length of the laser. Unlike conventional semiconductor lasers which the lasing process happens between different energy bands (conduction and valence bands) of a bulk semiconductor material and so-called inter-band transition, laser emission in QCLs occurs between discrete energy levels of one band (conduction band) of the quantum wells and so-called intersubband transition. The discrete energy levels in the quantum wells depend on the thickness of the quantum layers (quantum confinement effect) so they can be calculated and artificially engineered. The frequency of the QCLs therefore depends on the physical structure of the device and not on the natural property of the material. Another advantage of QCLs is that one electron can make emission of multiple photons by tunnelling from one well to the next, so the laser emission is very efficient. In addition, the QCLs are CW, room-temperature-operation (in mid-IR), high power of hundreds of milliwatts, small, low cost, roughness and durability. For those reasons, QCLs have become one of the most common laser sources for mid-infrared range [73].

It is considerably more difficult to produce lasers for the longer wavelengths as in the THz region. The THz photon energies are small making it difficult to design energy levels for electrons to selectively tunnel through the very close subbands. The energy loss increases proportionally with the square of the wavelength so waveguides are required [73-74]. The first THz QCL was reported only until 2001 [75]. The laser emitted 4.4 THz radiation (wavelength 67 μm); it operated in pulsed mode with peak power ~ 2 mW and at 50K operation temperature, though it still requires cryogenic cooling. Nowadays, operation frequency of QCLs are reported in the range of 0.84 – 5 THz [73, 76-77], at maximum operation temperatures 169 K pulsed and 117 K in continuous wave mode [78]. Output powers are as high as 250 mW pulsed or 130 mW in CW mode [73]. However, these figures are from different devices. Also, the availability of these QCLs is very local. The common operation range of available THz QCLs nowadays is between 3 - 4 THz and at 40 – 60 K maximum temperature.

2.2.6. Summary

In conclusion for this section, a summary of the output power versus frequency of different technologies are brought together in ***Figure 2.3*** [79]. In this figure, solid lines are for the conventional microwave sources and the ovals denote recently developed THz sources. The p-Germanium laser and different frequency generation (DFG), optical parametric oscillator are indicated by peak power; others are by continuous wave. The p-Germanium laser is among the ultra-high power laser group including free-electro lasers or synchrotron sources, they are also important to fundamental science but too bulky and expensive for general applications.

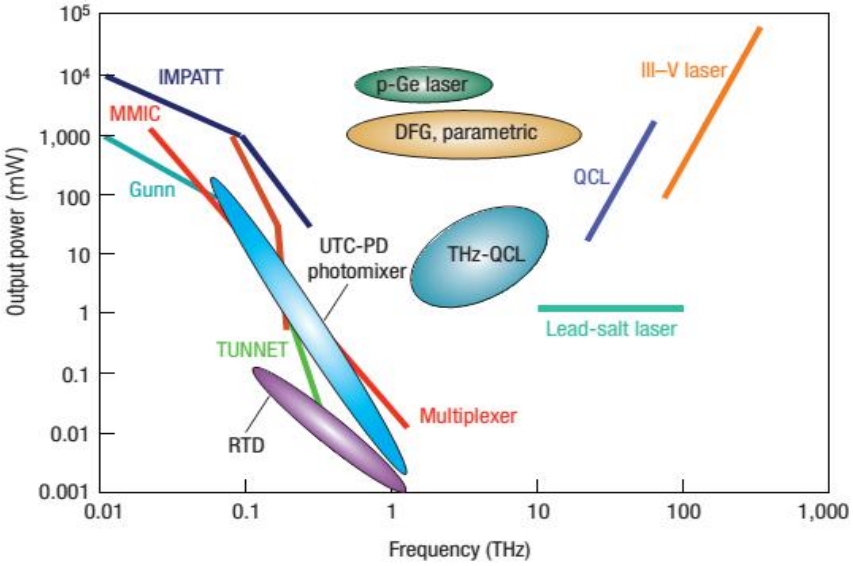

Figure 2.3: Power of different THz sources as a function of frequency, by Tonouchi [79]

Put aside the already heavily developed THz-TDS system, from the figure we can see clearly the three major approaches for developing THz sources: optical generation, solid state electronic techniques, and the recently developed THz QCLs. In terms of advances for metrology, the source should be narrow band, high power for future 2D detector application and of sufficiently high frequency to achieve a reasonable spatial resolution.

THz QCLs, which are a result of recent advances in nanotechnology, are still being refined in the THz region. Even though they are promising for the future, they are still not commercially available at reasonable power. At the present, THz QCLs cannot operate at frequencies as low as 2 THz and the lasers (QCLs) require cryogenic cooling for their operation.

From the optical side, the THz OPO is a promising candidate. Working at room temperature, the lasers can produce peak power as high as 1 W, bandwidth as narrow as 100 MHz, and tuneability from 0.7 – 3 THz. This source is investigated for metrology applications in Chapter 3.

The last approach for THz sources is from electronic devices which are entering the low end of the THz regime. Among those devices, THz-multiplier (multiplexer) is one of the most promising techniques. They can be phase-locked and very stable for phase/metrology measurement, also low cost, effective and room-temperature-operation. The recent technology can reach frequency as high as 2.7 THz at 4 μW. The source is adjustable for tuneability of frequencies from 0.1 THz to ~1 THz by adding more multipliers, so very flexible for future development of the measuring system. A THz-multipliers is used in Chapters 4 and 5 of the thesis, after the THz OPO was found to be unstable at the time it was tested.

2.3. THz DETECTORS

Difficulties in sensing THz radiation are due to low photon energies and a big diffraction limit (Airy disk diameter). Cryogenic cooling or long integration time are needed to increase the signal-to-noise ratio from the background thermal noise [37]. Many techniques are used in the detection of THz radiation and they can be separated into three main types: heterodyne detectors, direct detectors and coherent detectors.

Coherent detectors are mentioned above in the THz-TDS system. The original presentation was first reported by Auston et al. [80], again based on “Auston switch”. Much effort on improving the design and materials has resulted in the most common design using two antennas bridged by a thin film photoconductor (e.g. LT AlGaAs or Silicon-on-Sapphire) [4, 9, 63, 67]. THz radiation is detected by a second pair of ultrashort laser pulses to get the free electric charges in the photoconductor layer, between the antennas. Hence, the incident THz radiation drives the free electric charges to make a voltage between dipole antennas, which in turn can be measured by appropriate devices. Electro-optic sampling was reported in the same decade (1980s) [81-82], but only recently it became popular for ultrashort THz pulses detection [83-84]. The electro-optic sampling technique is based on Pockels effect of electro-optic materials. The electro-optic material becomes birefringent in the presence of the incident THz electric field. This event leads to a change in polarisation of a laser beam coming to the material, which can be measured by the aid of the polarisers and detectors

(e.g. photodiode). In comparison, electro-optic sampling provides a flat frequency spectrum and a true cross-correlation signal. The technique does not require an electrode contact or any wiring on the sensor crystal. In contrast, photoconductive sampling with a Hertzian dipole detector offers a superior sensitivity.

Heterodyne semiconductor detectors have been used for many years and they play an important role in radio applications, in Earth science and astronomy because of their simplicity and high sensitivity [37]. The detectors operate by shifting the detected signal into a lower (or higher) frequency range which can be detected by current technology. The shifting process is called heterodyning which is the beating together of two close frequencies in a mixer to yield some related frequencies. Those related frequencies include the sum, the difference and multiple of the original frequencies. In principle, one input frequency is the signal to be detected; the other is a reference frequency coming from a local oscillator (LO). The output of the mixer is filtered to isolate the desired frequency. The final result after the filter is called the intermediate frequency (IF). The IF is normally the difference frequency which is typically a much lower frequency than the signal (~ a few GHz for THz detection [85]). In this case the heterodyning is called down conversion and the IF frequency has an amplitude proportional to the amplitude of the signal and the same phase as the phase of the signal. These coherent properties make it possible to detect the amplitude and phase of the IF to provide information of the input signal.

Although the heterodyne technique is very sensitive, research on THz heterodyne detector focuses on finding the suitable components such as LO and mixer. State-of-the-art of mixers for THz heterodyne receivers is dominated by Schottky diodes or SIS mixers due to their low cost, effectiveness and simplicity. A suitable LO source requires the signal and the LO frequency to be close. Moreover, the two beam need to be similar in size and in properties such as beam radius curvature, transverse mode structure and their polarisation [86-88]. It is difficult to produce large format arrays for 2D detection with this technique.

Direct detectors which detect directly the intensity of THz radiation are the most straightforward sensors to extend to 2D arrays and this type of detectors are used in this thesis. The THz radiation is considered as high frequency (compared to microwaves), thermal absorption are commonly used technique for the direct detecting of THz radiation. This technique is based on the thermal effect of the THz radiation to the thermal materials to make the measurements, like Golay cell, pyroelectric detectors or

bolometers. Golay cells are sensitive and accurate but fragile and expensive. Pyroelectric detectors are currently not as sensitive as Golay cells but they are low cost and easy to use. Research is underway to develop 1 line or 2D THz pyroelectric detectors for THz. At room temperature, bolometers are not very sensitive to THz radiation. However, they can be more sensitive when using at low temperature. Extremely sensitive bolometers require cryogenic cooling and selective materials which are expensive.

2.3.1. Golay Cell

Golay cell detectors operate based on thermal absorption of gases in a chamber which results in the volume changing. The change in the volume is then detected, by detecting the reflection of light from a displaced mirror mounted on the back of the chamber. ***Figure 2.4*** depicts the schema of a typical Golay cell designed for THz detection. Basically it consists of a small closed metal chamber which is gas filled (e.g. with Xenon). The entrance window (front face) of the chamber is made of high absorption coefficient material sensitive in the THz range. The other end of the chamber is sealed with a displacing mirror. When THz radiation impinges on the entrance window, it heats the gas in the chamber causing the pressure to rise which moves the mirror. Light from a small light source is focussed on the mirror and is reflected to a photocell. Moving of the mirror changes the output of the cell which then can be detected conventionally (e.g. by a photodiode).

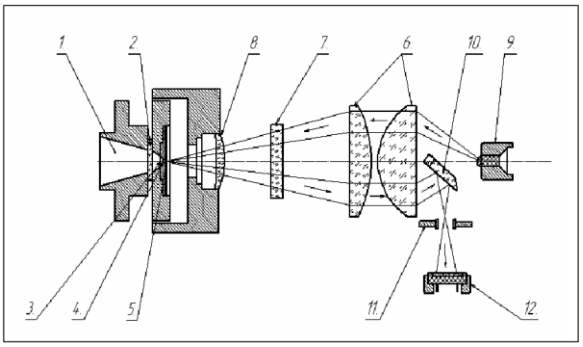

1: Entrance cone
2: Entrance window
3: Translucent film
4: Channel
5: Membrane mirror
6: Condenser
7: Optical raster
8: Plano convex lens
9: LED
10: Mirror
11: Diaphragm
12: Photodiode

Figure 2.4. Schema of a Golay cell detector for THz region from Tydex (Appendix A.3).

The Golay cell detector operates under room temperature and relatively high sensitivity ($NEP \approx 10^{-5} W/Hz^{1/2}$; the minimum detected power is typically sub nW to 10 μW), but it is very fragile because of the thin membranes and is also quite expensive

(~$12K to $15K). The response rate is approximately a few tens of millisecond. This type of detector was used in Chapter 3 while working with THz OPO laser.

2.3.2. Pyroelectric Detectors

Pyroelectric detectors are based on a thin film of pyroelectric crystal, which, under thermal absorption, its polarisation is changed instantaneously, as a function of the temperature changing rate of the crystal. Polarisation changing causes electric charge accumulation at the electrodes placed on two opposite sides of the crystal. This accumulation then can be measured by a voltmeter or other appropriate device.

Pyroelectric detectors respond to the rate of change of temperature; so the source must be pulsed, chopped or modulated. These detectors also operate at room temperature and the noise-equivalent-sensitivity (NEP) can be compared to that of the Golay cell, but response time is much lower (Golay cells ~ 25 ms, pyroelectric detectors ~ 100 ms). Recently, many companies (including startup companies) produce THz pyroelectric sensors [89], may be because of the potential extension to 2D array, of the simplicity in its fabrication and of its relatively low cost, especially when compared to other detectors such as Golay cells (~$100 to $2000). In Chapter 4 and 5 of the thesis, a pyroelectric detector was used together with the THz-multipliers for applications including interferometry and digital holography.

2.3.3. Summary

Coherent detection systems are sensitive. They have high dynamic range and ability to obtain both the amplitude and phase of the signal. However, the expense for being able to obtain both amplitude and phase of the signal is the time consuming. For example, in the case of THz-TDS detectors, time consuming comes from the need of scanning point by point for every THz waveform. In the case of heterodyne detection, it is difficult to find a suitable component for LO source. Finally, it is difficult to implement this type of detector in 2D array due to their operational and structural properties.

Meanwhile, direct detection offers sufficient resolution and is preferable for applications where the intensity sensitivity is more important than spectral sensitivity, such as in imaging and metrology. Among this type of detector, Golay cell has been used in THz detection for many years. This device provides reasonable performance characteristics but their large size makes them unsuitable for use in a 2D array. The

limitation in detected power range (typically 10 μW maximum), the fragility and relative high price are among other disadvantages.

Microbolometers are without question the most sensitive THz detectors. But there are some issues for this type of detector. First of all, they must be used at liquid helium temperature for THz detection which requires an expensive cryostat. Secondly, they are physically large and can be very expensive. For some specific applications which require very high sensitive detectors, microbolometer would be the THz detector of choice. But for basic measurements and applications, they are just not practical.

Pyroelectric detectors however, have some inherent advantages which make them suitable for industrial applications. They are room-temperature operation, small package, low price, and also readily available in many commercial sources. Their small size makes them suitable for 2D array extension in near future. This type of detector was used in the Chapter 4 and 5 coupled with THz-multiplier source to demonstrate feasibility in readiness for future 2D detectors. Also, a Golay cell was used in Chapter 3 as a convenient intermediate step.

2.4. THz APPLICATIONS

2.4.1. Spectroscopy

There are many materials and chemical compounds having absorption and transmission foot print (energy levels) in the THz region. Thus THz radiation offers a powerful method to determine and analyse properties of materials of interest. THz spectroscopy uses both coherent detection as in the THz-TDS system, and incoherent detection using frequency tuneable lasers coupled with a direct detector.

Most of the THz spectroscopy work has been done with the THz-TDS system, as it provides a broadband spectra range, which covers almost all the THz region. Many chemical compounds have been studied/identified successfully with this technique such as explosives [6-7, 90], drugs [91] and biological structures [92-93]. Using the THz-TDS system has become so popular that commercial packages for spectroscopy applications are available, such as TeraView (Appendix A.7). In THz spectroscopic applications, frequency tuneable lasers coupled with direct detectors were used as an alternative method to THz-TDS. These systems have been successfully applied to a wide range of materials [20-23, 94]. Though the THz gives a unique tool for spectroscopic determination of many materials and chemical compounds and THz-TDS

is very convenient for spectroscopy thanks to their ability to capture whole waveform of the THz pulses, THz lasers offer more intensity. A toolkit for THz spectroscopy using a frequency tuneable laser and direct detection is available from Toptica (Appendix A.7), which gives more choice for individual needs.

2.4.2. Imaging and metrology with broadband sources

THz imaging plays an important role in non-destructive testing for industrial and security applications. As with THz spectroscopy, most THz imaging works have been done with the THz-TDS system. Hu and Nuss [9] reported the first THz transmission imaging of a packaged semiconductor integrated circuit and of a leaf using THz-TDS. In this system, the acquisition time per pixel was reduced from minutes to less than 5 ms (compared to previous THz-TDS detecting and acquiring system); the scanning delay line was added to the system to down-convert THz to kHz; and a digital signal processor (DSP) was used for real-time spectral display. Approximated diffraction limited lateral resolution was of 250 μm. This work inspired a decade of the THz imaging applications. The same group further reduced the acquisition time [10] to 25 ms per measurement point by using a continuous sweep rather than slow steps for the optical delay line).

The first near-field imaging appeared by using a near-field tip (basically a small aperture) placed in front of the object under investigation at the focal point of the THz-TDS system [95]. The system is equivalent to near-field scanning optical microscopy (NSOM/SNOM). The amplitude of the signals was reduced by ~ 1/130 times (frequency dependent). Spatial resolution was measured by the scanning knife-edge to reach the sub-wavelength scale of $\lambda/4$. Other improvements and new applications of the system were reported in innumerable papers, always with the THz-TDS system [96-101].

Other imaging techniques like the time-of-flight imaging [10] for tomography applications has been reported. The reflection geometry was presented in which reflection pulses from multiple internal layers of an object with varying magnitude, polarity and distortion were studied to reconstruct its 3D structure. Depth resolution of 1 μm was obtained. The system is actually the THz-TDS system without the Fast Fourier Transform (FFT). The depth images were reconstructed by analysing the delay time of the reflected THz pulses. The broad bandwidth of the radiation and the coherent aspect of the detection are the advantages, since it enables to obtain the phase information to

reconstruct the depth [102]. The paper is followed by other claims in resolution and technique improvements [103-107], with a review paper about the technique [108].

Passive imaging images natural THz energy of an object based on its natural emitting spectrum in THz range (black body emission). This imaging technique is similar to the IR/thermal imaging, but in THz range. The technique requires very sensitive detectors in order to detect very weak THz radiation from black bodies (e.g. human). The first THz passive image of a human hand was from a joint project between European Space Agency and UK Rutherford Appleton Laboratory [109]. The image was taken by a 16 pixel detector array and at 0.25 THz. ThruVision is the only available commercial system for THz passive imaging (Appendix A.8). The company is a spin-out from the discussed project. One of the most promising applications of THz passive imaging may be in airport security checking. An advantage which makes THz passive imaging popular for security applications is that the technique does not require radiation to be emitted on to the human body so there is no health risk, and at the same time it enables to see through clothes or cover barriers.

With the popularity of THz-TDS, the system has been dominant in every THz application, including metrology. Krishnamurthy et al. [14] reported the use of THz-TDS emitting and detection in a Michelson interferometer setup to measure the index or thickness of thin polymer film (2 μm thick Mylar film). The difference in the Fourier spectra, with and without the sample were measured and analysed to determine the phase and amplitude shift of the THz pulse interacting with the sample. The refractive index was calculated from the known thickness by using the measured pulse delay in the time-domain. Depths that are greater than THz wavelength could not be measured unambiguously. Zhang *et al.* [110] introduced phase imaging, without the 2π ambiguity, of individual wavelength using THz-TDS. The THz-TDS system used InAs crystal for the generation of THz radiation with a wavelength range from 0.2-3.0 THz and with a spectrum resolution < 10 GHz. A polyethylene wedge object was scanned at 1.0 and 1.1 THz frequencies and then the synthetic wavelength was calculated for thickness measurement of the wedge. Noise was reduced for the composite wavelength as thermal and 1/f noise at individual wavelengths were recorded simultaneously and were therefore correlated. Other thickness and refractive index measurements using THz-TDS can be found published in [8, 111-112].

It is known that speckles, on one hand, deteriorate the image quality. But on the other hand, they can be used for metrological purposes, in particular, in speckle

photography and speckle interferometry. Groves et al. reported the use of THz-TDS in shearography for non-destructive testing of wooden panel painting [113]. A greater wavelength of THz radiation allows the measurement of displacements and deformations that are two orders of magnitudes larger than those measured in visible range. Although THz-TDS has been demonstrated the ability to apply in metrology, however it is not straightforward to upgrade the system to 2D array detector and it is very time consuming make it impractical for industry.

2.4.3. Metrology with narrowband sources

Studies on speckle reduction in millimetre wave imaging had been discussed in order to improve THz images [114-115]. However, because the THz wavelength is large, objects with roughness as big as a hundred micrometres are still smooth when they are illuminated by THz laser radiation. On the other hand, research on real-time speckle photography was reported [33, 116]. The study used a powerful FELs laser and a microbolometer array working at room temperature. The FEL's power was sufficiently large that it could be detected by a microbolometer array without the need of cooling. The study on the properties of speckle patterns at THz range shows that they are also accurately described by speckle theory in visible light: The size of objective speckle is inversely proportional to the THz beam diameter while the intensity distribution of a speckle grain is dependence of the aperture. These studies are fundamental and maybe interesting, but they haven't been shown any specific application. Speckle properties were investigated but research on speckle interferometry in which the speckled image of an object is made to interfere with a reference field has still not been reported.

Metrology measurement using interferometric methods with narrowband sources have been developed. Chen and Kaushik claimed the first use of THz radiation for macroscopic vibration measurement [117]. THz radiation at 0.615 THz generated from a BWO was detected by a single point Golay cell detector in a Michelson interferometer configuration. Vibration from a hidden/concealed object introduced phase changes which were detected and converted to amplitude variation by a spectrum analyser. The system was limited by the ability of detecting only small vibration amplitudes (<10 μm) and low vibration frequency (< 300 Hz). In addition, the phase was not extracted and the measurement was restricted for one point measurement only. Buersgens et al. [118-119] demonstrated some developments to measure and calculate the vibration wrapped

phase for 1D measurement (one line across interference fringes), but the limitation on the ability to detect only slow vibration at low amplitude was not improved.

Thickness measurement using an all-optical OPTL operated at 2.52 THz has been reported by Wang et al. [120]. The interference intensity from a Michelson interferometer was recorded with a Golay cell and the optical thickness measured at discrete points for a polyethylene wedge. The depth was determined from the known refractive index, but the absolute depth of step heights that exceeded the THz wavelength could not be calculated.

Multi-wavelength technique has been introduced to overcome 2π ambiguity in THz interferometry. The theory behind this technique is based on the formation of a synthetic wavelength from two or more applied wavelengths [121]. Wang et al. [122] claims first THz application of multi-wavelengths method using CW THz phase recovery for depth measurement. Dual wavelengths were generated from two different CW Gunn diode and BWO sources. Twice-scanning of 1D phase measurements were applied by scanning a single point pyroelectric detector to capture the phase change between the object beam and reference beam due to the known replacements of the object. A FFT was then applied to the superimposed signal to extract the individual frequency signal.

In conclusion, although THz radiation has been used widely for metrology application, most of the works had been done with THz-TDS and/or point scanning of single point detector. Research on exploring new THz instruments and technologies to improve and to find more practical method for industrial application are moving in fast pace. Particularly the moving to 2D measurements is a certain step in the future.

2.5. THz DIGITAL HOLOGRAPHY

Digital holography in THz region was reported for the first time in 2004 by Mahon et al. [123-124]. The system used a 0.1 THz Gunn diode oscillator source and a scanning detector to record the holograms in an off-axis configuration [125-126]. The lateral resolution achieved was about 9 mm without any discussion about the depth resolution. In 2005, Cherkassky et al. published their work on THz holography with a free-electron laser coupled with a thermal plate and a CCD camera in an off-axis system [127], though no reconstruction was demonstrated. In 2008, Tamminen et al. presented a holographic imaging technique that used a horn antenna emitting 310 GHz with a Gaussian profile and a single raster scanned receiver [128]. The object was placed at an

off-axis angle of 42^o from the reference beam. With each recorded hologram, an image of reference beam's amplitude was recorded separately for the use of the reconstruction. The holograms were reconstructed by Fourier transforming the interference pattern (to get the frequency spectrum), then spatially separating the object term in the spectrum image and finally de-convolve the object field based on the known reference phase. The system has a spatial resolution of 2 mm.

THz dual wavelength holography was introduced by Heimbeck at al. in 2011 [30] using a frequency tuneable THz multiplier source. The holograms were recorded at an off-axis angle between object and reference beams by a scanning Schottky diode detector. The phase reconstructions were made separately for two wavelengths, which process based on the separating in angular spectrum of the object term with others in space (similar as the method introduced by Tamminen et al. [128]). Combining the dual-wavelength measurements produces a synthetic wavelength measurement which overcomes the 2π ambiguity in depth measurement of individual wavelength [121].

Recently, Sun et al. reported phase shifting interferometry with three phase steps using a Gun diode emitted radiation at 0.39 THz and a Schottky diode as a receiver [129]. The interferograms were recorded at three equivalent interval steps but no hologram reconstruction was demonstrated. To the best of the author's knowledge, studies on THz phase-shifting digital holography with full reconstruction haven't been reported.

In this context, Chapter 5 of the thesis was devoted for the study on THz phase-shifting digital holography in which the phase was retrieved by phase-stepping technique at quadrature positions and the reconstruction algorithm was introduced. The technique was then applied for thickness measurement and non-destructive testing of internal defects. The background on DH and DHI is necessary theory to understand the work in Chapter 5 which would be presented below.

2.5.1. Background

In the most basic description, a hologram is a recorded interference pattern between two waves: a reference wave and an object wave after being diffracted (scattered) from a volume object. The latter is also called the object's speckle pattern, as it is composed of the object's speckles. ***Figure 2.5***(a) depicts a configuration for the recording of holograms, copied from [125].

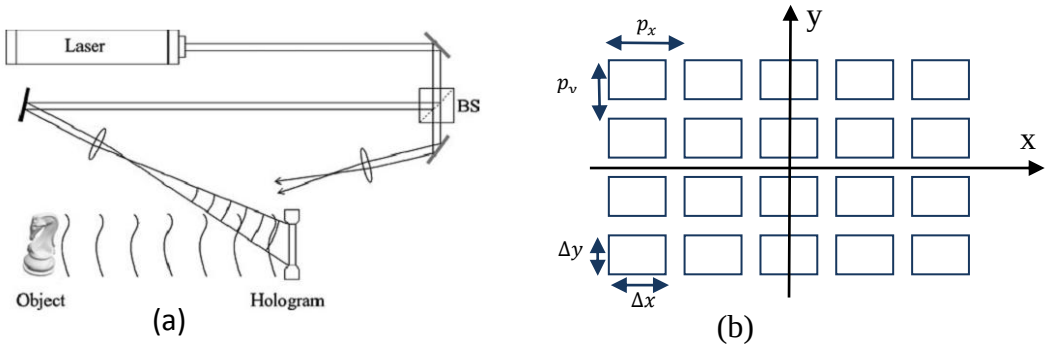

Figure 2.5. (a) Configuration for hologram recording [125]; (b) Detecting area of hologram with pixel size and pixel pitch description.

In conventional holography [130-132], a hologram is recorded by a photographic plate of very high resolution. In digital holography, holograms are recorded digitally by multi-pixels detectors, such as CCD or CMOS, with pixel size $\Delta x \times \Delta y$ and pixel pitch $p_x \times p_y$ for $M \times N$ pixels respectively in x and y directions (***Figure 2.5***(b)). The pixel size must be small enough to be able to resolve the micro-fringes in the hologram. If the object wave makes an angle θ with the reference wave and they interfere together at the hologram plane. The inter-fringe distance in the hologram can be calculated as:

$$i = \frac{\lambda}{2\sin\left(\frac{\theta}{2}\right)} \tag{2.7}$$

Mathematically the object and reference complex amplitudes are described as below:

$$O(x,y) = o(x,y)e^{i\varphi_O(x,y)} \tag{2.8}$$

$$R(x,y) = r(x,y)e^{i\varphi_R(x,y)} \tag{2.9}$$

Where o and r are real amplitudes; φ_O and φ_R are the phases of the object and the reference wave respectively. The two waves interfere together at the hologram plane. The interference intensity is calculated as:

$$I(x,y) = |O(x,y) + R(x,y)|^2$$
$$= O(x,y)O^*(x,y) + R(x,y)R^*(x,y) + O(x,y)R^*(x,y) + O^*(x,y)R(x,y) \tag{2.10}$$

Where O* and R* are conjugate complex. Let *H(x, y)* be the function describing the recorded intensity of the hologram (the hologram's intensity, is linearly proportional to

I(x, y)). In conventional holography, the reconstruction is made by illuminating the hologram with the reference wave. In that case, we have:

$$R(x,y)H(x,y) = (o^2 + r^2)R(x,y) + r^2O(x,y) + O^*(x,y)R^2(x,y) \quad (2.11)$$

$$A = (o^2 + r^2)R(x,y)$$

$$B = r^2O(x,y)$$

$$C = O^*(x,y)R^2(x,y)$$

In the above equation, A, B, C are three orders of the reconstructed image. A is the zero order which is an un-diffracted wave passing through the hologram. B is +1 order which is the reconstructed object wave (multiplied by a constant). It is called virtual image as it can be observed directly. C is the real image of the object (-1 order). For off-axis holography, the three orders are separated spatially.

In digital holography, this reconstruction process can be modelled numerically by multiplying the recorded hologram with *R(x, y)*, which is a constant if the reference wave is planar and perpendicular to the hologram plane. Then the reconstruction is made by applying Fresnel-Kirchhoff diffraction theory. In this case, the hologram with coding fringes in it acts as an aperture which diffracts the incoming light wave (the reference wave), as described in ***Figure 2.6***. This diffraction is described by the Fresnel-Kirchhoff integral [126, 133]:

$$D(x', y', d) = \frac{i}{\lambda}\int_{-\infty}^{+\infty}\int_{-\infty}^{+\infty} H(x,y)R(x,y)\frac{\exp\left(-i\frac{2\pi}{\lambda}\rho\right)}{\rho} \times \left(\frac{1}{2} + \frac{1}{2}cos\theta\right)dxdy \quad (2.12)$$

In which *d* is object-hologram distance, *H(x, y)* is recorded hologram and *R(x, y)* is reference wave. ρ is point-to-point distance between the hologram plane and the reconstruction plane as the integral runs from $-\infty$ to $+\infty$. This is related to the Huyghen-Fresnel principle in diffraction theory which states that each point of the wavefront (diffracted reference wave at the hologram in this case) acts as a point source for its wavelet to travel toward the observation (reconstruction) plane; the resulting wave is the sum of these wavelets (hence the integral). ρ is then calculated as:

$$\rho = \sqrt{(x - x')^2 + (y - y')^2 + d^2} \quad (2.13)$$

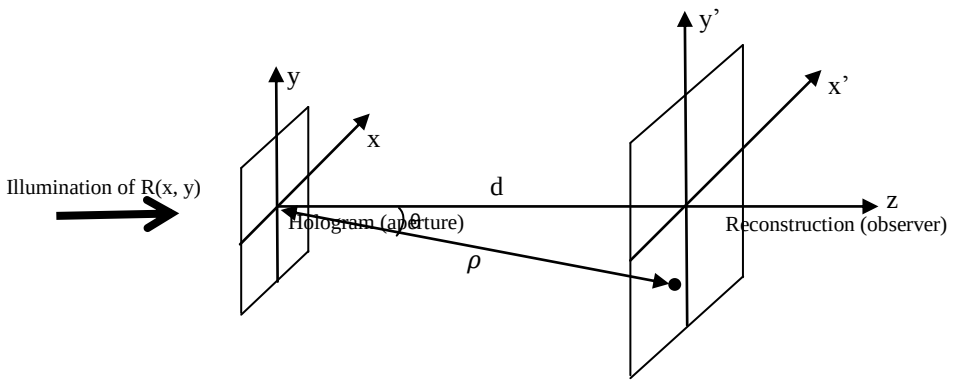

Figure 2.6. Coordinates for diffraction of the Fresnel-Kirchhoff diffraction integral through the hologram.

For the reconstruction, there are two most common approaches that will be considered here within the framework of this thesis. They are called the reconstruction by Fresnel transformation (or Fresnel approximation), and the other is called the reconstruction by convolution approach. In both cases, the reconstructed wavefield is a complex function from which both intensity and phase can be extracted.

2.5.2. Reconstruction by Fresnel Approximation

The Fresnel approximation approximates the calculation of distance ρ when x, y and x', y' are small compared to d. In that case, $cos\theta \approx 1$ and ρ is approximated as:

$$\rho \approx d + \frac{(x'-x)^2}{2d} + \frac{(y'-y)^2}{2d} \tag{2.14}$$

Replacing this new approximation to the ρ in exponential factor in equation (2.12), we get:

$$D(x', y', d) = \frac{i}{\lambda d}\exp\left(-i\frac{2\pi}{\lambda}d\right)\exp\left[-i\frac{2\pi}{\lambda d}(x'^2 + y'^2)\right]\int_{-\infty}^{+\infty}\int_{-\infty}^{+\infty} H(x,y)R(x,y)$$

$$\times exp\left[-i\frac{\pi}{\lambda d}(x^2 + y^2)\right] exp\left[-i\frac{2\pi}{\lambda d}(xx' + yy')\right] dxdy \tag{2.15}$$

However, the digitally recorded hologram is not infinitely long and is also discrete, due to the limitation of the detector's resolution; the above integral described in equation (2.15) can be re-written according to a finite hologram's size as:

$$D(m,n,d) = \frac{i}{\lambda d}\exp\left[-i\pi\lambda d\left(\frac{m^2}{N^2\Delta x^2} + \frac{n^2}{N^2\Delta y^2}\right)\right]\sum_{k=0}^{N-1}\sum_{l=0}^{M-1} H(k,l)R(k.l)$$

$$\times exp\left[-i\frac{\pi}{\lambda d}(k^2\Delta x^2 + l^2\Delta y^2)\right] exp\left[i2\pi\left(\frac{km}{M} + \frac{ln}{N}\right)\right] \quad (2.16)$$

where m = 0, 1, …, M - 1 and n = 0, 1, …, N - 1 are pixel position in reconstruction image;

k = 0, 1, …, M – 1 and l = 0, 1, …, N – 1 are pixel positions in the recorded hologram.

Equation (2.16) is the discrete Fresnel transform. In this equation, the sums correspond to a discrete Fourier transform relationship. Thus, the matrix *D(m, n)* can be calculated by applying an inverse discrete Fourier transform to the multiplied product between *H(k, l), R(k, l)* and $exp\left[-i\frac{\pi}{\lambda d}(k^2\Delta x^2 + l^2\Delta y^2)\right]$. The factor in front of the sum can be neglected for most applications [125].

For reconstruction by the Fresnel transformation, the pixel size in the reconstructed image depends on the reconstruction distance and is calculated as:

$$\Delta x' = \frac{\lambda d}{M\Delta p_x}; \qquad \Delta y' = \frac{\lambda d}{N\Delta p_y} \quad (2.17)$$

This size corresponds to the diffraction limited resolution (Airy disk size) of the optical system at distance d from the hologram in which the hologram is the aperture. It defines the spatial resolutions in the reconstruction image. Examples of a typical hologram and its reconstruction by this approach will be presented in Chapter 5.

Also, according to Huygens-Fresnel principle, every single point in the hologram may receive a diffraction patterns diffracted from every individual point of the object (or it equals to a sum of the wavelets). This means that every recorded point of the hologram has the information of the entire object. Thus a hologram can be reconstructed at any size smaller (than M x N pixels) and we will still get the same view, but the resolution will be smaller according to the equation (2.17).

2.5.3. Reconstruction Based on Convolution Theorem

This approach is based on the convolution theorem which states that the Fourier transform of a convolution between two functions is the pointwise product of individual Fourier transform. To start with, we reconsider the Fresnel-Kirchhoff integral (equation 2.12) and rewrite the equation as:

$$D(x', y', d) = \int_{-\infty}^{+\infty}\int_{-\infty}^{+\infty} H(x,y)R(x,y)\, g(x'-x, y'-y)\, dxdy \quad (2.18)$$

Where $g(x', y', x, y)$ is given by:

$$g(x'-x, y'-y) = \frac{i}{\lambda}\frac{\exp\left[-i\frac{2\pi}{\lambda}\sqrt{d^2+(x'-x)^2+(y'-y)^2}\right]}{\sqrt{d^2+(x'-x)^2+(y'-y)^2}} \quad (2.19)$$

in which the approximation $cos\theta \approx 1$ was used.

Equation (2.18) reveals that the double integral is a convolution between product function $(H \times R)$ and the impulse response g. If we take the Fourier transform of this convolution, the result should be equal to the product of the individual Fourier transforms according to the convolution theorem. This relationship is written in the following equation:

$$F[(H.R) * g] = F(H \times R) \times F(g) \quad (2.20)$$

Equation (2.20) leads to an idea that we can calculate the reconstruction pattern $D(x', y', d)$ by taking Fourier transform of $(H \times R)$ and of g, then multiplying them together; finally taking an inverse Fourier transform of this product.

$$D(x', y', d) = F^{-1}\{F(H.R) \times F(g)\} \quad (2.21)$$

Images reconstructed by the convolution approach have the same pixel size as of the hologram:

$$\Delta x' = \Delta x \qquad \Delta y' = \Delta y \quad (2.23)$$

The reconstruction by convolution is advantageously applied to in-line holograms to localise the objects within the reconstructed volume [125].

2.5.4. Phase-shifting Digital Holography

Holographic method which record only one single hologram to reconstruct both amplitude and phase of the object wavefield suffers from the constraint on physical configuration and digital recording. The reconstructed wavefield contains the real and virtual images as well as the DC signal. Care needs to be taken of the recording setup that the object and reference waves are tilted to a minimum angle from each other, so that the three order images are separated spatially. But at the same time this tilted angle needs to be smaller than a maximum angle, so that the detector can resolve the interference pattern between the object and reference beams.

Skarman *et al.* [134] presented a very different approach to solve the problem. They first applied the phase-shifting method to calculate the initial phase of the real

image. That way they can extract exactly the desired real image based on the known phase. Later this phase-shifting DH was improved and applied to many other applications by Yamaguchi *et al.* [135-138].

The configuration setup for the recording of holograms in phase-shifting digital holographic interferometry (DHI) is similar to that of phase-shifting interferometry in which the reference beam is guided by a moveable mirror to make the phase shifts. The principle of the phase-shifting method is to make the measurement of different interferograms of successive phase steps to be able to calculate the phase by an appropriate algorithm [133]. Here we adapt the four phase steps of $\pi/2$ phase difference from each other and use Carré algorithm [139] for this case to calculate the initial phase for hologram reconstruction. Higher phase-steps require more images to be acquired and the lower ones would be noisier. The choice of using four phase steps is made to balance these facts.

If we call the four recorded holograms as I_1, I_2, I_3, and I_4; each is of $\pi/2$ difference in phase from each other, then the hologram with known phase is written as:

$$H = (I_1 - I_3) + i(I_4 - I_2) \tag{2.24}$$

Apply this to the reconstruction algorithm described above and we can get the exact object's real image and phase at the object's plane without being distracted by other image orders. The information can then be used for applications such as deformation measurement or detecting internal defects of transparent objects, etc.

2.5.5. Digital holographic interferometry

The principle of digital holographic interferometry is based on the reconstruction of the phases at different states of an object. These states could be the changing in thickness or the displacement of a surface, etc. If the deformation between two states is small, then the reconstructed amplitudes are almost the same, but the phase is changed by a small amount of $\Delta\varphi$, i.e. the phase difference between the object beam and reference beam of an interferometer before and after the deformation. The deformation can then be calculated relates to the phase change by:

$$\Delta D = \frac{\lambda \Delta\varphi}{2\pi \Delta n} \tag{2.25}$$

In which ΔD is measured deformation, Δn is difference in refractive index and λ is THz wavelength.

2.6. CONCLUSION

The state of the art of THz technology has been reviewed. The purpose of this review was to provide a broad view on the field together with the needed tools for better understanding the methods used in the thesis. The emphasis of the review was on the potential THz sources and detectors for metrology applications. It is clear from the research reviewed that there are more and more available THz systems where the techniques are mostly borrowed from either optical and/or electrical regions. THz-TDS is dominant in most research work and applications in THz domain. In the next chapters, two types of THz sources will be studied in which one is an all-optical source and the other is an all-electronic source. Potential applications will be explored which take advantage of the THz radiation over the other frequency ranges.

Chapter 3

THz INTRA-CAVITY OPO FOR NON DESTRUCTIVE TESTING AND THICKNESS MEASUREMENT

3.1. INTRODUCTION

In this chapter, some initial work with an intra-cavity OPO THz laser is presented. The choice of this laser comes from a careful consideration of the literature review on THz sources (Chapter 2). The presented laser became commercially available relatively recently, and has potential interest capabilities for metrology including single wavelength and narrowband (so relatively long coherence length), tunable in a wide range of THz regime and relatively high peak power. The objective of this work was to assess its suitability for full-field metrology. The emphasis is on interferometric metrology measurements, but spectroscopic measurement to investigate the THz properties of some materials of future interest were also considered. In section 3.2, the inspection of transmission properties of some materials of future interest are presented. Experiments include the non-destructive testing (NDT) of internal defects in subsection 3.3.2., and thickness measurement is discussed in subsection 3.3.3 which is the first reported use of an all-optical THz source for thickness measurement. Conclusion for the whole chapter will be considered in section 3.4.

3.2. THz TRANSMISSION PROPERTIES OF SOME MATERIALS OF FUTURE INTEREST

In order to view the transmission of some materials of future interest, including some type of ceramics for medical and turbine industry applications, as well as to gain experience with an intra-cavity OPO THz laser, experiments were initially undertaken at

the University of St Andrews. The laser used was initially developed from the University of St Andrews and is still based there. The transmission properties are important for the applications in imaging and sub-surface non-destructive testing (NDT) evaluation. A description of the measuring system is presented in sub-section 3.2.1. The results and the data analysis of the transmission spectra are covered in sub-section 3.2.2.

3.2.1. System

Transmission measurement system is shown schematically in ***Figure 3.7***. The THz OPO laser emitted a THz beam into free-space which was collimated by a cylindrical lens (not shown in the figure). The beam was focused by a parabolic mirror P1, and was spatially filtered by a pinhole before passing through sample to be measured at the focusing point. A system of two parabolic mirrors P2 and P3 focussed the transmitted light to a cooled single point bolometer detector. To make a transmission measurement, a reference measurement of the incident radiation intensity without the specimen is needed. Hence for each sample, two sets of data of transmitted and reference intensity were recorded.

The THz OPO laser is frequency tuneable from 1.2 to 2.5 THz for the system tested. Continuous frequency tuning is made by changing the angle between the pump laser beam and the nonlinear crystal which is mounted on a rotation stage. Under computer control of the rotation stage, THz output beam is rotated a maximum angle of 0.5^{o} while the output frequency is tuned between 1.2 - 2.5 THz. The THz wavelengths are not measured directly but are inferred as the difference between the known pump wavelength (1064 nm) and the measured idler using a wavemeter [59]. A lock-in amplifier (LIA) was used to reduce noise and to amplify the measured signal from the bolometer detector. The LIA's sensitivity was set depending on the amount of light transmitted through the samples.

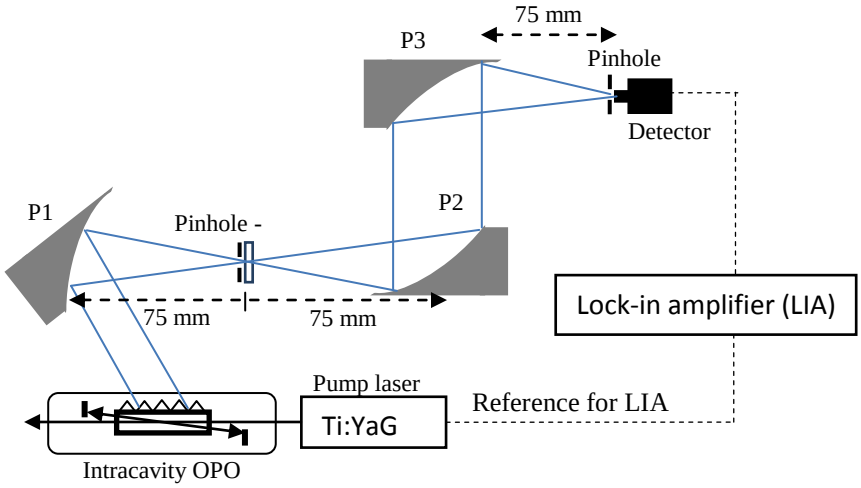

Figure 3.7. Transmission measuring system with an intra-cavity THz OPO laser. P1, P2, P3 are gold coated parabolic mirrors.

According to the Beer-Lambert law, the intensity of the transmission of light through a substance decreases exponentially with the depth in the material. If $I_0(\lambda)$ is the incident (reference) intensity coming to a sample and $I(\lambda)$ is the transmitted light, then:

$$\boldsymbol{I(\lambda) = I_0(\lambda)\, e^{-\mu(\lambda)\, x}} \qquad (\mathbf{3.1})$$

where λ is the wavelength; x (in cm) is the thickness of the sample and μ(λ) (in cm^{-1}) is the linear attenuation coefficient which is a material property of the intensity lost per unit length (e.g. in one centimetre). However, the results presented here only show the transmission of the samples at the measured thickness. The transmission spectra are therefore:

$$\boldsymbol{T(\lambda) = \frac{I(\lambda)}{I_0(\lambda)}} \qquad (\mathbf{3.2})$$

where $T(\lambda)$ is the transmission at monochromatic wavelength λ; $I(\lambda)$ and $I_0(\lambda)$ are, as described above, transmitted and reference intensity respectively.

3.2.2. Results

Figure 3.8 shows a typical reference spectrum without any specimen (original data). The THz frequency and the intensity were recorded at each angle of the nonlinear crystal. There was an obvious error in some measured data which arises from frequency counting. This error is due to the wrong reading of the idler wavelength as the THz wavelengths are calculated from the known 1064 nm pump wavelength and the

measured idler [59]. Also, because the recorded frequencies of the sample and those of the reference were not synchronised, it is confused in choosing frequency range for plotting the transmission spectra (calculated from equation (3.2)). Therefore the intensity data was plotted in measured order rather than at the measured frequency (frequency re-ordered).

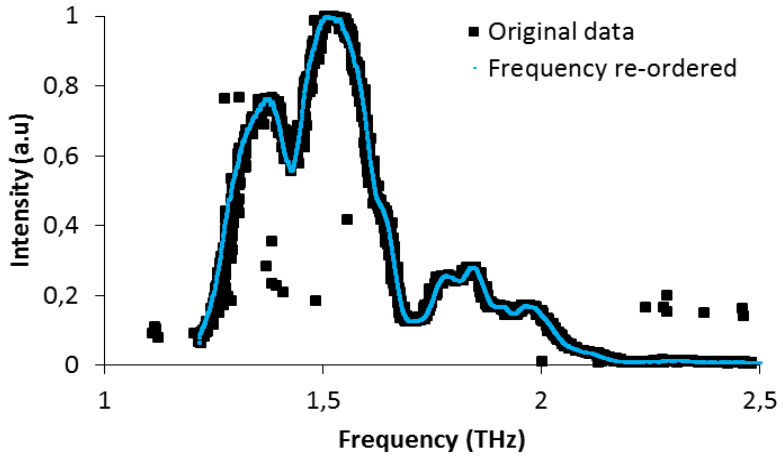

Figure 3.8. A typical reference intensity measurement showing frequency errors (original data) and intensity measured versus re-ordered frequencies (Frequency re-ordered).

The frequencies were recalculated by dividing the calibrated frequency range (1.2 – 2.5 THz) to the known number of frequency/intensity points. Then the frequency range was separated into individual frequency points, each point is separated at a distance of the above number from its neighbours. Thus, the measured intensities are plotted versus those re-calculated frequencies. This approach yields accurate results, as shown in the figure (*Figure 3.8*). By recalculating the frequencies for both reference and sample, the frequency and intensity of the measured data are now synchronised for calculating and plotting of transmission spectra.

The transmission results are shown in ***Figure 3.9***. The measured materials are some type of ceramics including YSZ, YTZP, Alumina and MgPSZ. MgPSZ has full name as Magnesia Partially Stabilized Zirconia which the chemical composition is MgO stabilized with 9% ZrO_2. YTZP is Yttria Tetragonal Zirconia Polycrystal and is composed of Y_2O_3 stabilized with 3% mol ZrO_2. Alumina ceramic is well-known with its chemical composition Al_2O_3. YSZ is Yttria Stabilized Zirconia and is used in thermal barrier coating for turbine blades.

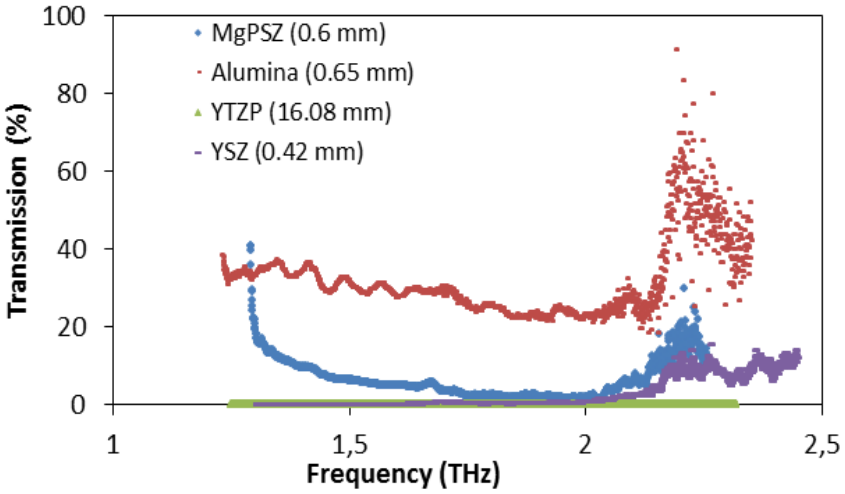

Figure 3.9. THz transmission properties of some materials of interest. Thicknesses of the specimens are: MgPSZ 0.60 mm; Alumina 0.65 mm; YTZP 16.08 mm; YSZ 0.42 mm.

Adding fractional Zirconia to YTZP, YSZ or Mg-PSZ can enhance their physical and chemical characteristics of the materials. The enhanced characteristics include excellent erosion, durability, and corrosion, abrasion resistance, together with temperature resistance, fracture toughness and strength. That is why they become the materials of choice for various extreme service applications which can take advantage of their properties, like in the chemical and petrochemical industry, as well as in the healthcare and dental services sectors. Those applications demand specific and tough requirements. Hence the structure of the ceramics materials must be well-controlled. Recent work has had some success in characterising zirconia ceramics in the early fabricating state, in order to control the manufacturing process [140]. That work used infrared (IR) light for 3D imaging of objects' sub-surface structure, in order to detect internal defects of the samples. However the method failed while applying on some other ceramics or with thicker specimens due to non-transmission problem. This section studied THz transmission properties of those samples in order to verify whether THz can replace IR as a probe radiation.

The transmission results in ***Figure 3.9*** show that the investigated ceramics do not have any noticeable absorption/transmission peak in the studied frequency range. It is also noticed that at the end and/or at the beginning of some spectra, there are noisy transmission points which are due to the low intensity level of both the reference and transmitted light. The YSZ which is used in thermal barrier coating of gas turbine

blades isn't transmitted in this range. There are some existing works in literature which applied THz wave to study YSZ [141-143]. However, they were all using the TDS system, with the THz spectra from 0.1 – 4 THz. In those papers, the range from 1.2 to 4 THz doesn't show any transmission of YSZ, which agreed with what was observing in this result. Transmission spectra of MgPSZ show some small level of 5 - 10% transmission from 1.2 - 1.65 THz for 0.60 mm thickness. At 0.65 mm thickness, Alumina specimen has 30 - 40% transmission. However, the THz wavelengths are quite long (1.2 – 1.65 THz, equivalent to 0.25 mm down to 0.18 mm wavelength), which will limit the spatial resolution. Meanwhile, measurements on YTZP sample and its variances (not shown in the graph) including Pre-sintered 3Y-TZP ($(Y_2O_3)_3(ZrO_2)_{97}$), Porcelain blocks (YTZP with added Fe_2O_3 for colouring) do not show any transmission at this frequency range. Literature review on YTZP doesn't found any work done at THz frequencies.

3.3. NON-DESTRUCTIVE TESTING AND THICKNESS MEASUREMENT

In order to determine the suitability of the intra-cavity OPO source for metrology, the research on the THz intra-cavity OPO system continued with a commercial THz intra-cavity OPO borrowed from M-squared Laser. The laser operating system was already described in Chapter 2 but it is very compact as a commercial product. In this section, imaging and interferometric thickness measurement experiments were performed using the laser. The measuring system for the reading and recording of the data was setup once for all the imaging and interferometric experiments. The optical configurations for each measurement are described in the appropriate sub-section which corresponds to the related measurement.

The measuring system includes the laser source which is the THz OPO laser, a Golay cell detector and a lock-in amplifier. The laser operated at 52 Hz pulse repetition rate (which corresponds to the frequency of the Q-switch pump laser), 20 ns pulse duration and 10 nJ pulse energy (peak power 1W and 05 μW mean power). The spectral bandwidth was approximately 100 GHz, corresponding to a coherence length of approximately 3 mm. For detecting of the THz signal, a Tydex Golay cell GC-1P was used. The detector has an entrance window diameter of 6 mm, 20 - 30 ms response rate, 10 - 20 Hz optimum modulation frequency, and responsivity of 10^6 V/W at optimum

modulation frequency but goes down to ~ 10^3 V/W when detecting signal of 50 Hz modulation frequency (Appendix A.3).

The low laser output power and small detector responsivity produced a low SNR of approximately 2 and hence a lock-in amplifier (LIA, Stanford Research Systems SR530) was used to reduce noise and to amplify the signal. Due to the requirement for the input of the LIA, a TGP 110 10 MHz pulse generator was used to produce a symmetric reference signal which is triggered and synchronised by the 52 Hz frequency pulse of the pump laser Q-switch. The Q-switch signal was amplified to 5 volts and buffered before input to the pulse generator. The output from LIA was read and recorded manually. In order to reduce external noise sources the entrance of the detector was covered with a piece of black paper. The THz was transmitted through the paper, whilst the effects from visible light and environmental fluctuation to the detection were eliminated.

3.3.1. Imaging Internal Defects

The experimental setup is schematically depicted in ***Figure 3.10***. M was a flat mirror used to re-direct the THz beams radiated from the OPO laser. The parabolic mirror P, coupled with lens L1, had an effective focal length of ~ 50 mm which is shorter than the focal length of individual element. This coupling system focussed the THz beam to a focal point of 3 cm from lens L1, where the objects under investigation were placed and scanned around. The lens L2 collected the transmitted THz beam onto the Golay cell detector entrance. The distance L1-L2 was chosen so that the Gaussian beam filled the aperture of L2 in order to maximize transmission through the system. The THz frequency was chosen at the peak intensity of the laser's spectra range, and at the transmission window of water absorption in the air, which is of 0.952 THz (λ = 0.315 mm).

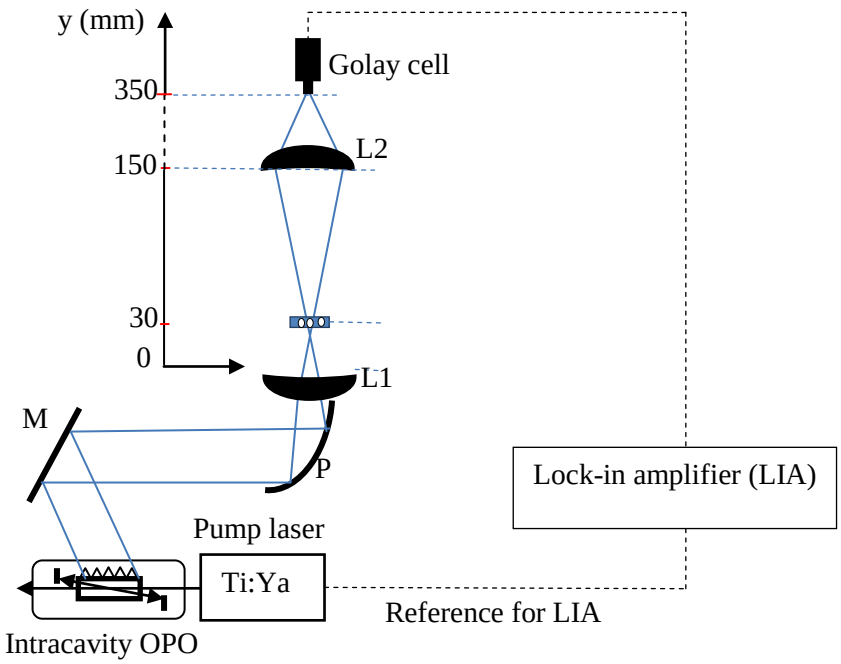

Figure 3.10. Experimental setup for non-destructive testing of internal defects.M is gold coated, flat mirror; L1 and L2 are Teflon plano-convex lenses of 50 mm diameter and 100 mm focal length; P is parabolic mirror.

In this setup, the lens L2 played a role as an objective whereas the condenser was composed of the parabolic mirror P and lens L1. The detector was placed at the image plane of the objective L2 (at 20 cm from L2), the magnification at the intermediate plane (detector plane) is 20/12. Numerical aperture (NA) of a lens is expressed as a multiple between the refractive index *n* of the measured environment (*n* = 1 in the air) and the sine value of one half angular aperture θ ($\sin\theta = D_a/\sqrt{f^2 + D_a^2}$ with D_a is obstacle aperture radius and f is focal length). As the optics (P, L1, L2) had the same size of 50 mm diameter, NA of the condenser and objective are 0.640 and 0.208 respectively.

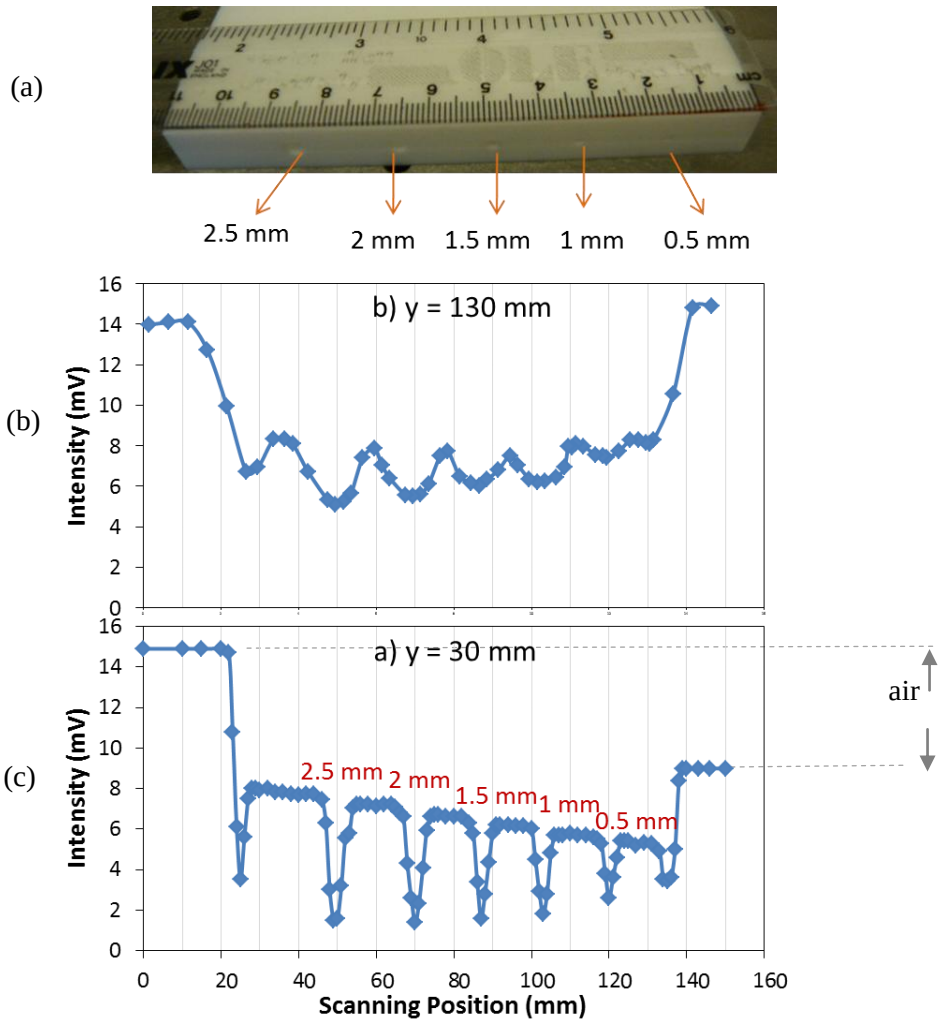

Figure 3.11. A teflon sample with artificial holes in sub-surface was used to calibrate the measurement (a). Scanning results at out-of-focus point y = 130 mm (b) and at focus point y = 30 mm (c).

A Teflon block with sub-surface artificial defects was used as a test object to calibrate the measurement and is imaged in ***Figure 3.11*** (a). The machined cylindrical defects had diameters between 0.5 to 2.5 mm and are 15 mm spatially separated from each other. ***Figure 3.11*** (b) and (c) show the results of scanning the object at different positions in y axis. The horizontal axis is scanning position in cm, which can compare with the holes' positions, as shown in the picture of the object with a ruler. The vertical axis is the value of relative intensity, measured at each position. The object sample was placed at focus point y = 30 mm and then at out-of-focus point y = 130 mm to compare. Obviously at the focus point the intensities drop deeper than at the out-of-focus point. This means that it is sharper when viewed at the focus plane. The spatial resolution of

this setup can be calculated as the resolution for bright-field (trans-illumination) imaging system which is written [144]:

$$D_s = 1.22 \frac{\lambda}{NA_{cond} + NA_{obj}} \tag{3.3}$$

where λ is the wavelength, NA_{cond} is NA of the condenser and NA_{obj} is NA of the objective. Theoretical calculation gives a spatial resolution of 0.43 mm. There is a matchup between theory and experiment as we can see in *Figure 3.11* (c) when the object is in focus, the 0.5 mm hole can be separated clearly from the area around it. It is also noticed that the laser output power was dropping during the measurement by comparing the intensity in the air at the beginning and at the end of the measurement. The two wells of intensities at two sides of the object correspond to the light scattering at the edges of the object.

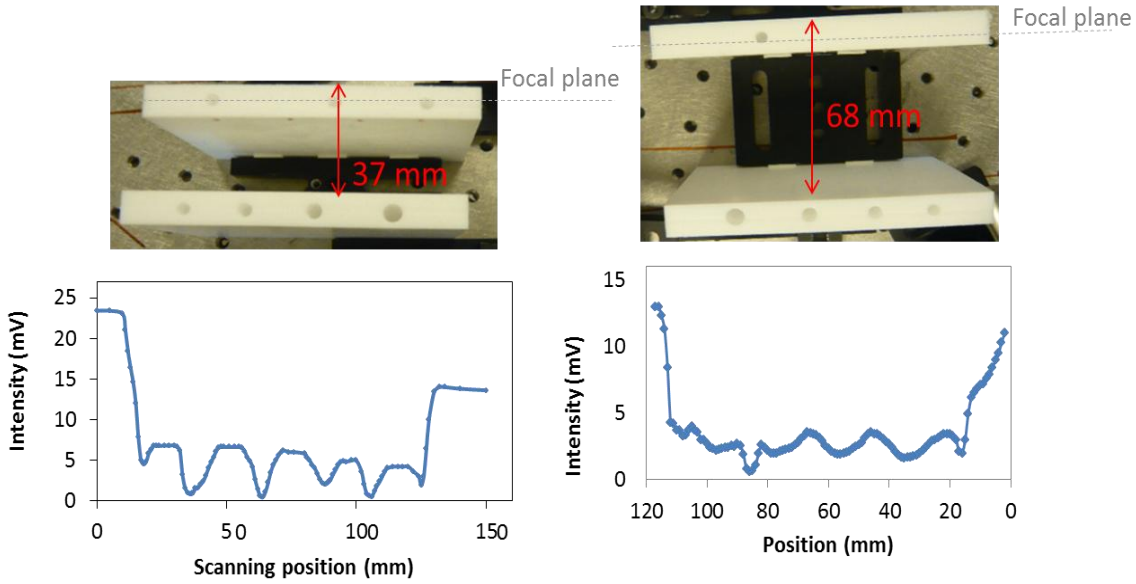

Figure 3.12. Images and scanning results of the test objects designed with two Teflon blocks which have artificial defects in them and are fixed at 37 mm (left) and 68 mm (right) distance from each other.

In *Figure 3.12*, two objects were designed by adding a second Teflon block separated at different distances from the previous target which was placed at the focal plane. The block placed at focal plane of the first object has 3 holes of 4 mm diameter; an additional block with 4 holes sized from 3 to 6 mm was placed at 37 mm distance from the first one (called 37 mm object, upper – left image). The second object was composed of one Teflon block placed at focal plane which has 1 hole of 4 mm diameter and another block placed at 68 mm distance which has 4 holes sized from 3 to 6 mm

(called 68 mm object, upper – right image). The scanning results of the two objects are presented below the images.

The depth of field, which is "the depth in specimen space that appears to be in focus within the image, without readjustment of microscope focus", can be calculated using the expression [144]:

$$\boldsymbol{D_d = \frac{\lambda n}{NA^2} + \frac{n}{M \times NA_{obj}} e} \tag{3.4}$$

where n is the refractive index of the measured environment (n = 1), e is detector pixel size (6 mm), NA_{obj} was calculated above (= 0.208), and M is magnification(=20/12), giving a calculated depth of field of 25.87 mm. The scanning result of the second object (68 mm) shows that the 4 mm defect at focal plane was imaged sharply among those which are blurred at the out-of-focus plane of 68 mm distance from the focal plane. This result is matched with the calculated depth of field described above. However with the first object (37 mm), it is hard to recognise the defects which are separated at the planes of 3.7 mm distance in depth. There are reasons which may explain for the disagreement between this observation and the calculated depth of field. First of all, the refractive index of the measured environment should be bigger than 1 as the light passes through the first Teflon block to go to the second block, so the theoretical depth of field could be bigger than the calculated number with n = 1 as above. Secondly, the laser intensity was decreased with time (***Figure 3.13***) and was dropped very much by the end of the measurement, which fact makes it hard to extract the dropped intensities caused by the laser intensity fluctuation with those caused by the defects.

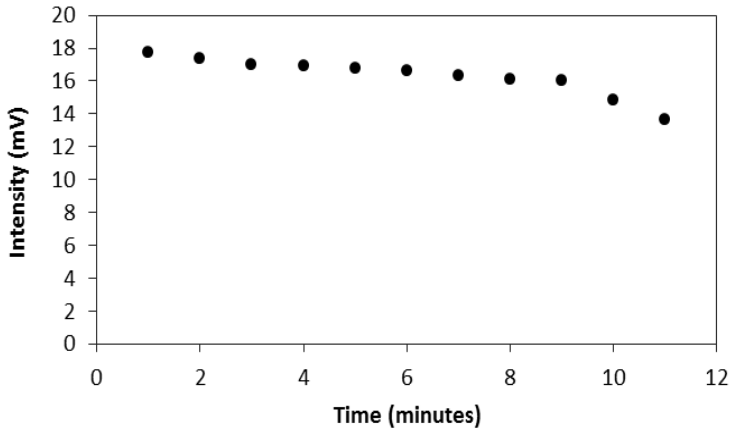

Figure 3.13. Laser output intensity vs time.

Based on the results, it can be concluded that even without an aperture, ignoring the effect of the Gaussian and expanding beams, the coarse measurement of spatial

resolution matched the theoretical prediction within maximum 14% of full scale and could be smaller.

3.3.3. Thickness Measurement Using Multi-wavelength Interferometry

A Mach-Zehnder interferometer was constructed using the THz laser, ***Figure 3.14***. The interferometer was aligned initially with a HeNe laser (not shown), after which the THz beam was introduced. The interferometer comprised two 23μm thick Mylar sheet beam splitters (BS1 and BS2) and gold-coated mirrors (M1 and M2). The THz beam diameter in the interferometer was approximately 10 mm, which was reduced to 2 mm on the Golay cell detector. The detector output voltage was filtered and amplified by a lock-in amplifier, as described above. The reference beam mirror M2 was mounted on a linear translation stage (positional accuracy ~1 μm) to change the optical path length of the reference beam. Moving M2 by distance d produced a path length change $2dcos\theta$, where θ is the angle of incidence of the laser beam on mirror M2. The object tested was a 66×108 mm2 poly-Tetrafluoroethylene (PTFE or Teflon) block of nominal thickness 5mm. Material was milled from one half of the block to produce a step height of 235 μm (measured with a micrometer gauge).

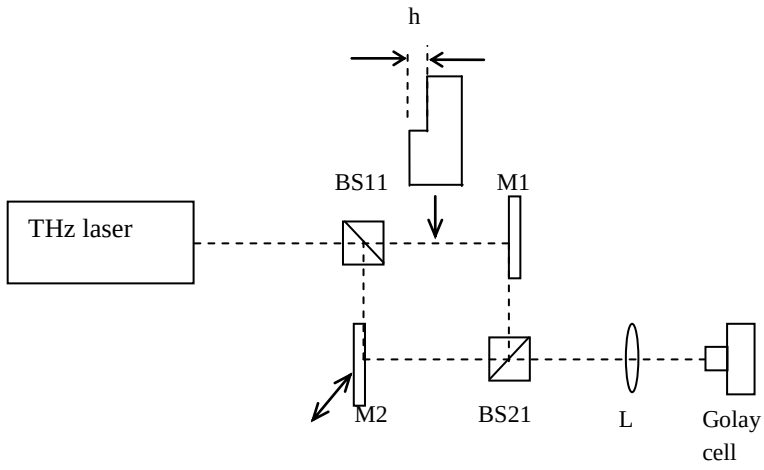

Figure 3.14. Schematic of the interferometer used for thickness measurement and object with a step height of h.

For a π/2 phase step at a laser wavelength of 315.13 μm, the lateral displacement of the beam was 66 μm compared to its diameter of 10 mm. No change in intensity of the reference beam was measurable for mirror M3 positions corresponding to four steps

of 0, π/2, π and 3π/2. The lateral motion will also shear the object and reference wavefronts in the interferometer, but again no effect was measureable for the nominally plane wavefronts used in the experiments reported here.

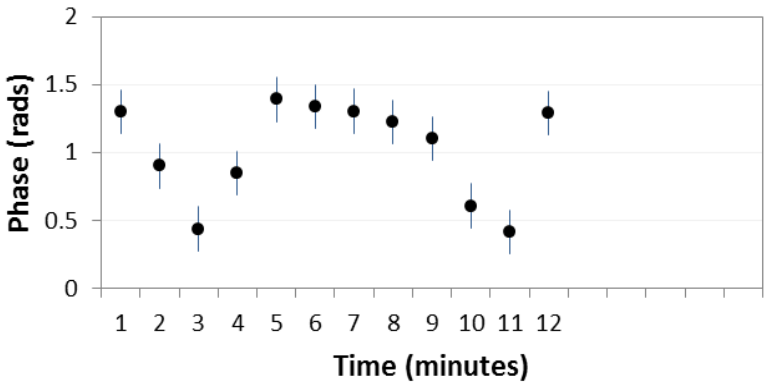

Figure 3.15. Phase noise measurement.

The recording of the phase-steps requires a minimum stability of the laser intensity during the recording time. However, with the trial technology of that time ($MgO:LiNbO_3$ with incorrect coating was used as nonlinear medium for THz generation), the laser intensity was dropped apparently as already seen in the previous measurement (***Figure 3.11***) and was not sufficiently stable for this task. ***Figure 3.15*** shows a phase noise measurement in which the phases were extracted from the recorded phase-steps and surely the phase was very noisy during just 12 minutes. The M-Squared have now fixed the problem in their subsequent systems. For this reason, in this experiment the phase was measured by tracking a whole 2π period to reduce noise in phase measurement.

Figure 3.16 shows the linear regression between measured phase at 0.9520 THz and its modulated fitting cosine function of the 'thin' part of the object, i.e. the milled half of the object. The phase was tracked in a whole 2π period. Linear fitting line is plotted in red colour. R^2 is the correlation coefficient of the fitting to the measured data. The same analyses to the measurements on the 'thick' part of the object and at 1.1063 THz were done, and the resulting R^2 coefficients are in between 0.971 to 0.984. These values of R^2 demonstrate a strong uphill linear relationship between the measured data and the modulated fitting cosine function. Therefore in this case, tracking the whole 2π

episode of the phase provides a more precision in phase measurement than the 4-phase-stepping technique.

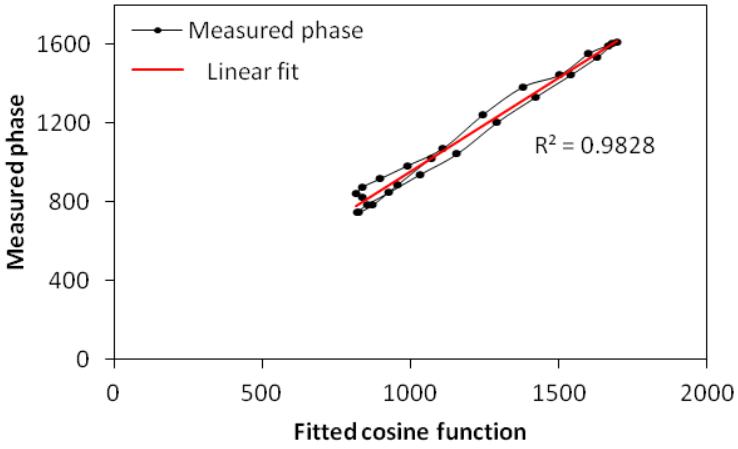

Figure 3.16. Measured phase of the 'thin' part of the object versus the fitting cosine function at 0.9520 THz. Fitting of the linear regression between the measured and the modulated values is presented by the red line. R^2 is correlation coefficient.

Figure 3.17(a) shows the phase-stepped intensities recorded at 0.9520 THz (wavelength 315.1 μm) for the "thin" section of the object. The phase was stepped through approximately π radians by moving mirror M2 in 10 μm steps. ***Figure 3.17(b)*** shows the numerical differences between intensity measurements recorded at adjacent mirror positions, around the maximum and minimum fringe peaks of ***Figure 3.17(a)***.

The purpose of calculating the intensity differences was to determine the positions of the maximum and minimum intensity, where the local intensity gradient is zero. Phase measurements in ***Figure 3.15*** were based on four recorded phase-steps to calculate the phase from an appropriate algorithm. In this measurement, the sampling rate was increased by recording many points of the whole 2π period of the phase. The accuracy and precision of the measurement was improved by increasing the sampling rate of the measurement in which the errors in the phase determination were reduced. As shown in ***Figure 3.17(b)*** for the thin section of the object, linear fits were applied to the intensity differences and the fringe maximum and minimum positions were identified from the zero crossing positions.

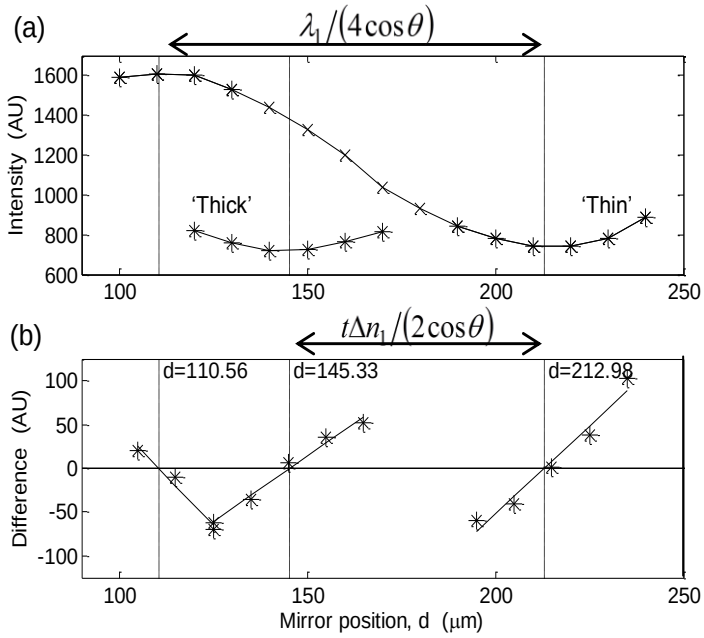

Figure 3.17. (a) Phase-stepped intensity plotted against mirror position at 0.9520 THz (wavelength 315.13 μm). (b) Intensity difference between adjacent measurements (i.e. numerical intensity gradient) and linear least squares fit to determine the intensity maximum and minima.

The movement of mirror M2 between the fringe maximum and minimum for the thin section was Δd = 213.0 – 110.6 μm = 102.4 μm corresponding to a measured wavelength of λ_1=313.8 μm for θ = 40°, i.e. an error of 0.4% of the laser wavelength. For an ideal cosine, this linear fit method to the intensity differences for ±π/4 radians around a maximum (or minimum) is accurate to <0.1% for the position of the maximum (or minimum).

The object was then moved to illuminate the "thick" section of the block, i.e. the non-machined half of the object. ***Figure 3.17(a)*** shows the phase-stepped intensities recorded in the region of the fringe minimum only. ***Figure 3.17(b)*** shows the intensity differences and the position of the minimum identified from the linear fit. As shown in the figure, the measured change in the mirror position at the fringe minima between the thick and thin sections of the object was Δd_1 = 213.0-145.3 μm = 67.7 μm, corresponding to an optical thickness $t\Delta n_1$ of 103.6 μm. Teflon is non-dispersive and has a refractive index of $n = n_g = 1.445$ that varies by less than 6% over the 0.2 to 3 THz range. Therefore using $\Delta n_1 = \Delta\Delta_n = 0.445$ for the object in air, the measured geometrical thickness of the step height was 232.9 μm, i.e. difference of 0.7% of the

laser wavelength compared to the micrometre measurement. Clearly the measurement is ambiguous to multiples of the THz wavelength.

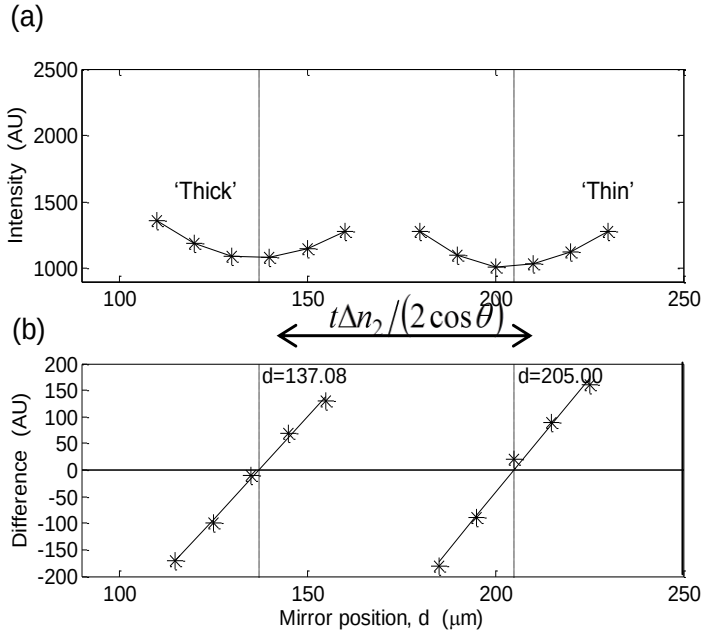

Figure 3.18. (a) Phase-stepped intensity plotted against mirror position at 1.1063 THz (271.17 μm). (b) Intensity difference between adjacent measurements (i.e. numerical intensity gradient) and linear least squares fit to determine intensity minima.

The measurement was repeated with the laser tuned to 1.1063 THz ($\lambda_2 = 271.14$ μm). ***Figure 3.18****(a)* shows the phase-stepped intensities recorded in the region of the fringe minima for the thick and thin sections of the object. ***Figure 3.18****(b)* shows the positions of the fringe minima determined from the intensity difference. As shown in the figure, the measured change in the mirror position at the fringe minimum between the thick and thin sections of the object was $\Delta d_2 = 67.9$ μm, corresponding to an optical thickness $t\Delta n_2$ of 104.1 μm. Therefore the measured geometrical thickness of the step height was 233.8 μm, i.e. a difference of 0.4% of the THz wavelength compared to the micrometre measurement. This difference can be considered as the uncertainty of the measurement. Again, this measurement is ambiguous to multiples of the THz wavelength.

The phase differences $\Delta\phi_1$ and $\Delta\phi_2$ due to the step height can be calculated from the optical thicknesses $t\Delta n_1$ and $t\Delta n_2$ at each illumination wavelength respectively, following the theory already described in Chapter 2, the equations from which are repeated here:

$$\Delta\phi_1(x) = k_1 t \Delta n_1 \tag{3.5}$$

$$\Delta\phi_2(x) = k_2 t \Delta n_2 \tag{3.6}$$

The step height can be calculated as:

$$t = \frac{\lambda_s(\Delta\phi_2 - \Delta\phi_1)}{2\pi\Delta n} \tag{3.7}$$

In this equation, the synthetic wavelength $\lambda_s = \frac{\lambda_1 - \lambda_2}{\lambda_1 \lambda_2} = 1942.4$ μm. The measured step height is 239.8 μm. The synthetic wavelength measurement is "coarse" because it magnifies the noise in the phase measured at each wavelength by the same factor as the magnification of the wavelengths. It is more accurate to divide the synthetic wavelength step height into integer multiples of one of the wavelengths, for example λ_1, and add that number of integer wavelengths to the λ_1 measurement. For the current example, the synthetic wavelength demonstrates unambiguously that no correction is required to the measured optical thickness at either of the individual wavelengths. The unambiguous measurement range of the optical thickness has been extended to the synthetic wavelength.

In summary, the optical thickness variation of a test target was measured successfully in a Mach-Zehnder interferometer. The output frequency of the laser was tuned to 0.9520 and 1.1063 THz in order to generate a synthetic wavelength and the unambiguous measurement range was extended to seven wavelengths. An accuracy of approximately 0.5% of the THz wavelength was achieved over the extended measurement range for the step height. These were the first unambiguous thickness measurements with an all-optical THz source, to the best of our knowledge. The optical parametric THz laser enabled direct detection to reduce the measurement time, compared to opto-electronic sources and does not require the specimen to be placed in a chamber with a dry atmosphere. It operates at a shorter wavelength than electronic sources, thus increasing the resolution. Tuning the optical parametric THz laser was a straightforward task, enabling the absorption lines of atmospheric water vapour to be avoided. Interferometric measurements with direct detection were demonstrated.

3.4. Conclusions

In conclusion, the THz intra-cavity OPO laser source has been studied for some metrology measurements. Through the course of the experiments, the laser was unstable due to the limited technology (unsuitable nonlinear medium) at the time of the tests. For

this reason, the tests were applied to a limited number of points for each measurement (one scanning line in defect detection and one point in thickness measurement). Due to the instability of the laser intensity, the phase was instable too. Therefore, a whole 2π period of the phase was recorded in order to increase the sampling rate of the phase measurement, which can reduce the error in the calculation. Although the intra-cavity OPO technique has many advantages over many other sources (relatively high peak power, narrowband, widely tuneable in a continuous range) and the laser has been demonstrated to be suitable for interferometric measurements with direct detection, the limited technology at the time of the tests was not suitable for full-field metrology application. Therefore an electronic source was chosen for performing the experiments in the next Chapters.

Chapter 4

THz MULTIPLIERS

4.1. INTRODUCTION

The search for a suitable THz source for full-field metrology application leads to the choice of using THz OPO laser for its relatively short wavelength and therefore higher spatial resolution (Chapter 3). Though the original intention was to use an optical THz source, the THz intra-cavity OPO laser presented to be unstable due to the limited technology of the nonlinear medium at the time of testing. Therefore an electronic source which has been known to be reliable in order to prove metrology principles was used for the next measurements.

Among the electronic techniques, THz frequency-multiplied sources have certain advantages, compared to the solid state THz sources or BWOs, despite their relatively low output power at high frequency (> 1 THz). Firstly, they are compact and low cost, compared to heavy BWOs. Secondly, they work at room temperature and at lower frequencies that the QCLs cannot reach. Thirdly, they are inherently phase-lockable and frequency tuneable [26].

This chapter focuses on the characterisation and some initial application examples of a THz multiplier source in our lab. The chapter starts with some general descriptions of the THz- multiplier source. Then next section goes through the characterisation of a pyroelectric detector, which was used for detecting of the THz signal. The noise of the source - detector combination was studied as well. At the end, some initial applications will be presented and discussed: spectroscopy (in transmission measurements), interferometry (thickness measurement), and imaging applications.

4.2. THE SOURCE AND THE DETECTOR

The THz source from Virginia Diodes Inc (VDI) comprised a microwave synthesiser of 9.16-13.88 GHz tuneable frequency and an amplifier/ multiplier chain (AMC) of three triplers producing cw, highly coherent radiation at 0.259 – 0.375 THz. It generates THz

radiation at relatively high output power from 0.4- 1.2 mW, ***Figure 4.19***. A diagonal horn directs the generated THz wave into free space.

The operating frequency of the synthesiser is digitally controlled. The controlling programme from VDI was modified, in order to automatically scan the output frequency, with the desired frequency step and scanning range. Separate code was written to apply a User Controlled Attenuation (UCA) voltage, where 0 V corresponded to no attenuation and 5 V to full attenuation. These programmes were written in LabVIEW. In addition, the source has a TTL port which enables the output radiation to be modulated by applying a voltage pulse chain to the port. In most of the experiments in this chapter, and in Chapter 5, the source was operated at the highest frequency of 0.375 THz (wavelength 0.8 mm) in order to reduce the diffraction limit of the measurements. In the transmission experiment, where the specimen samples were checked for their transmission properties, the frequencies were scanned through the frequency range of the source.

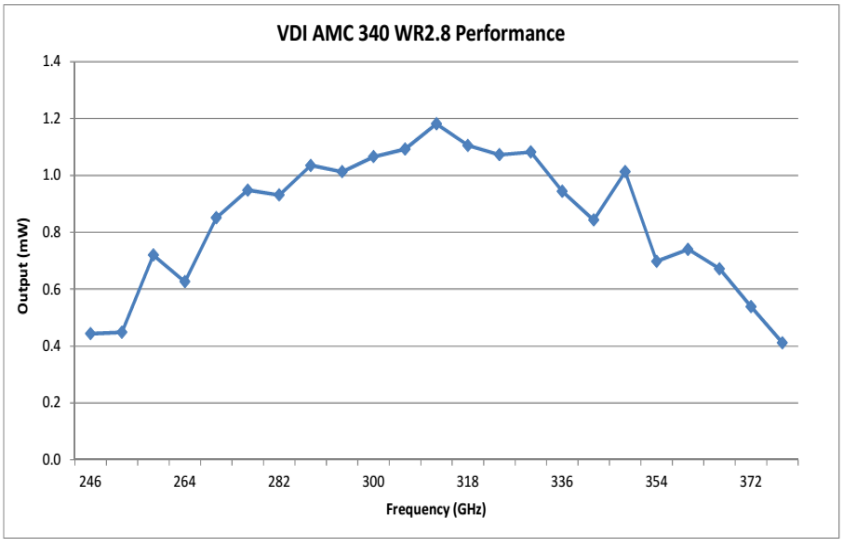

Figure 4.19. VDI calibrated output of the source, power versus frequency.

For detecting of the THz radiation, a Gentec THZ2I-BL-BNC pyroelectric detector was used. The detector has a rise time equal or smaller than 200 ms and an effective aperture of 2x2 mm^2. The pyroelectric detector detects a change in temperature rather than the absolute temperature, so the detected radiation needs to be pulsed or modulated. Therefore the THz output beam was modulated by applying a voltage pulse train, which the minimum voltage is 0V and the maximum is 5 V, to the TTL port of the source.

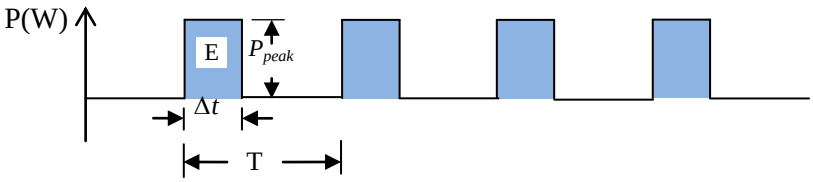

Figure 4.20. Laser power and laser energy: P is laser power, E is laser energy, Δt is pulse and T is full pulse period.

Figure 4.20 describes the relation between the source power, energy and the pulse duration. The power of a source is the optical output power in Watts and is normally understood to be the continuous power output in the case of a cw laser and as the average power output in the case of a pulsed or modulated laser (Appendix A.4). The laser energy is equal to the area underneath one laser pulse.

The core of a pyroelectric detector is pyroelectric material which absorbs the measured radiation power and creates electrical charges at its surfaces based on a polarization change. A voltage can be measured between the surfaces of the material, which the level increases with the absorbed radiation. A typical response of a pyroelectric detector to a laser pulse is schematically depicted in ***Figure 4.21*** (Appendix A.9). The result within the response time of the detector is a rising voltage, which, at the maximum level (V_{max}), is proportional to the laser pulse energy and/or peak power. It is then followed by an exponentially decaying period. After that, it needs a longer recovery time in order to return to the initial state.

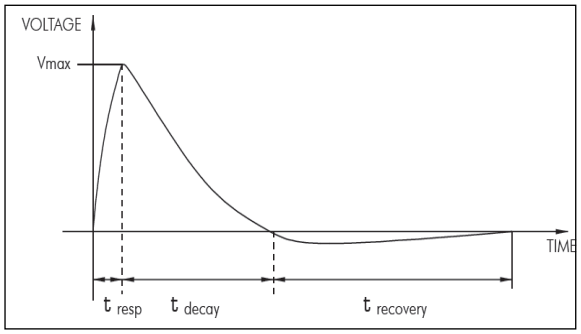

Figure 4.21. Typical response of a pyroelectric detector to a laser pulse.

To detect the signal accurately, it is important that the source and the detector must have their timing controlled accurately: the integration time must coincide with the

THz pulses. In other words, the sampling (the reading and recording) of the detector response must be taken at the right time following the modulated THz signal as described in ***Figure 4.22***. This job was done by applying a single generated digital pulse train to do multiple tasks: to modulate the THz source and to synchronise the detector response sampling.

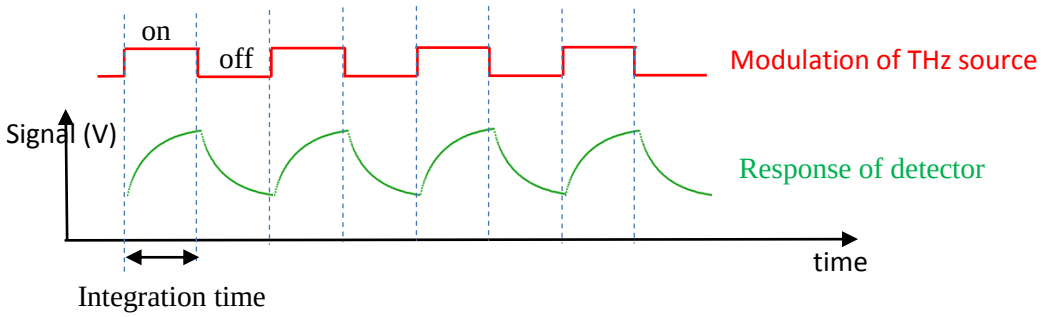

Figure 4.22. Modulated response of the pyroelectric detector (green line) to a pulse train of modulated THz radiation (red line) with the synchronisation for the reading/acquiring data (Integration time).

The voltage responses of the detector were acquired by a NI PCI 6221 instrument which was also used to create a digital pulse train. This instrument board was connected to a PC and was controlled via a programme coupled with the main program written in LabVIEW. The digital pulse train triggered the modulation (via TTL port) and at the same time drove the sampling measurement of the response signal from the detector. The pulse train is like a time scale for pulsing and reading/ acquiring data from the detector response.

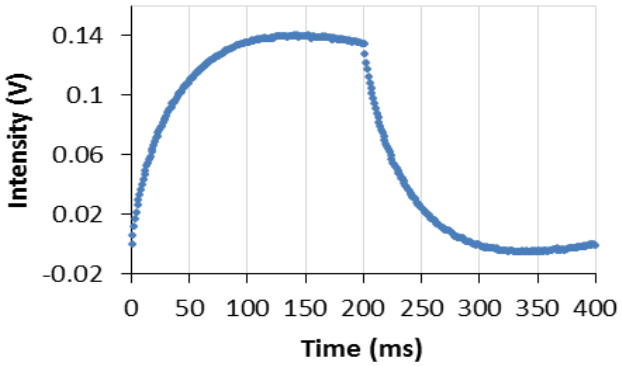

Figure 4.23. Response of the pyroelectric detector to THz pulse with duration 200 ms.

In order to investigate the response time of the detector, THz pulses of 200 ms were recorded and the average of the pulses is presented in ***Figure 4.23***. In these measurements, no voltage was applied to UCA port and the detector was put at a position on the optical axis in front of the source. From this measurement, the pulse reaches maximum voltage response at 125 ms whereas at 200 ms the response of the detector starts to decay. This result is agreed with the calibrated rise time from the company which suggests that the detector's rise time should be equal to or smaller than 200 ms.

4.3. DETECTOR PERFORMANCE

Measurement noise from the detector can be separated into internal and external sources. The internal noise sources include Johnson noise, shot noise and 1/f noise [145] (Appendix A.10). The system was isolated so that noise from external sources such as air flow, temperature fluctuation, external light, etc. were reduced to below the internal noise level.

Figure 4.24 shows a random noise measurement with the pyroelectric detector with the THz source blocked. The room temperature was controlled at approximately 19^{o}C with the lab air conditioning. The measurements were taken once every 1 millisecond, during 4 seconds (although the graph only shows 2s worth data). It is unavoidable that the room temperature changed by a small amount during this time and contributes a small part in the noise measurement. However, this drift is invisible as the measurement was made during very short time (4 s). The noise level is 0.0026 (V) which was calculated as the standard deviation (SD) of the measured samples.

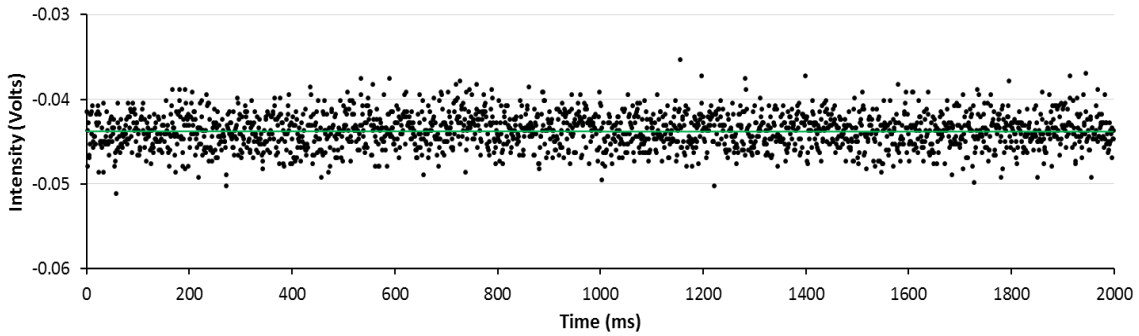

Figure 4.24. Random noise measured with the pyroelectric detector without THz illumination. The green line is mean value of all of the measurements.

After that, the THz source was opened and the detector was placed in front of it to measure the THz radiation. The THz signal was modulated at 5 Hz frequency and 50% duty cycle. The acquisition sampling rate was kept the same (1000 samples/second). So the response of the detector to one THz pulse is 200 ms duration with 200 samples captured at each ms (***Figure 4.25***(a)). The pulses are recorded continuously and the responses of 120 pulses were recorded. Average of 120 responses is calculated in ***Figure 4.25***(b) and noises of individual samples in the THz pulse were extracted from the 120 recorded results (***Figure 4.25***(c)). In comparison, each calculated point in ***Figure 4.25***(c) is the noise level (SD) of 120 measured samples which are 200 ms delayed from the other; the position of the calculated noise in horizontal axis (time, ms) corresponds to the position of the samples in one THz pulse.

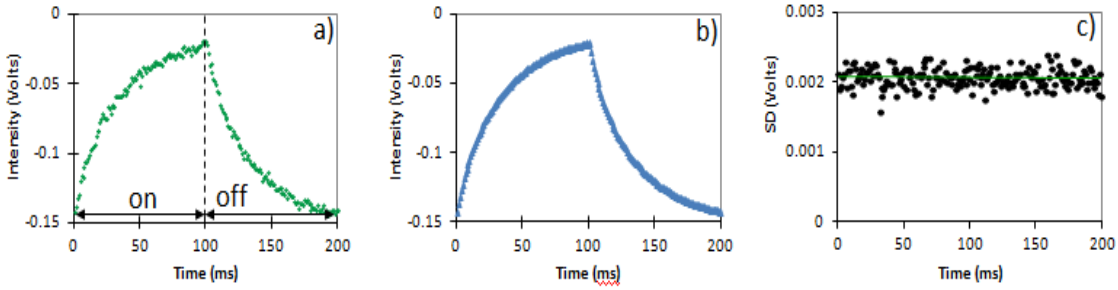

Figure 4.25. a) A typical response of a pyro-electric detector to one THz pulse: "on" region is response when the THz pulse was on, "off" is response when the pulse was off; b) Average of 120 responses; c) noise (SD) at each sample in time was calculated for 120 samples; the green line is averaging level of them all, and equal to 0.00207 (V).

Figure 4.25(c) shows that at every response sample, the noise level keeps unchanged at around the level of the random noise (≈ 0.002 V). The stable noise level means that the noise is not affected when the THz radiation is on or off. From these results, it can be concluded that the pulse to pulse of the source-detector combination is repeatable and is super-imposed by the random noise of the detector.

Voltage response of a pyroelectric detector reaches a maximum intensity level after a given time within rise time. This maximum intensity is normally used to calibrate the pulse energy of a source. The integration of the voltage response (the area underneath of the response curve) has a linear relationship with the maximum voltage as well as with radiation intensity and can also be used to calibration the radiation intensity (see Section 4.5: Linearity, ***Figure 4.33***). In fact, as the noise at every response sample is random and does not depend on the THz radiation intensity (***Figure 4.25***), the integration

(the summation) of the response samples should have a smaller noise than that of individual sample. Taken into account the random noise at each voltage response sample is ~ 0.002 V, if the samples are summed together during 125 samples, the pulse to pulse noise is of ~ 0.25 V (125 × 0.002). But the sum is actually smaller than 0.25 V so when it is divided by the number of samples (125 samples), the noise level becomes smaller than that of individual sample's noise. In that case, the noise is reduced according to the averaging method. To prove this theory, the above 120 recorded pulses are integrated during the "on" period (***Figure 4.25***(a)) and the pulse to pulse noise is then compared to peak voltage noise.

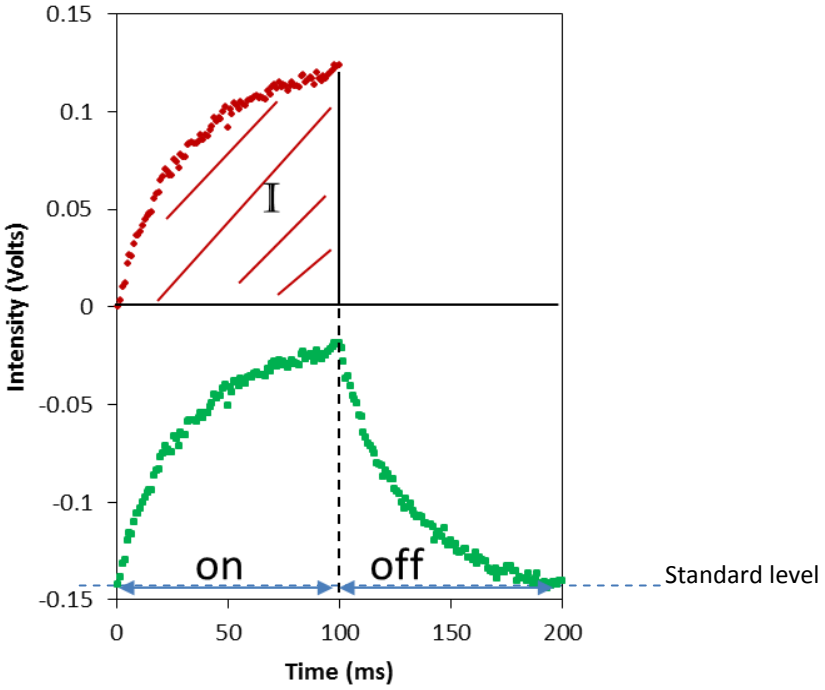

Figure 4.26. Integration process: The original data is shown in green for the response of the detector to the THz pulse of 5Hz 0.5 duty cycles. The red trace shows the moving of the "on" period of the original data to above zero level and the integration I *of the period is described as the red area underneath the red trace.*

Figure 4.26 presents the integration process in which the original data is shown in green. The voltage response of the detector can be separated into two periods: when the source was "on" and when the source was "off". To calculate the integration of the "on" period, the response samples are moved to above zero level (by subtracting them to the standard level) and are summed together. The standard level was determined as the noise level (when the source was blocked to the detector). The standard level is stable if the measurement environment is isolated from temperature change. As the peak

voltage is measured by only one sample, to be able to directly compare the noises of the peak voltage and the integration measurements, the summed (integration) values are divided by the number of integrating samples, which is 100 samples in this case as the source was on during 100 ms (***Figure 4.26***) and the sampling rate was 1000 samples/s.

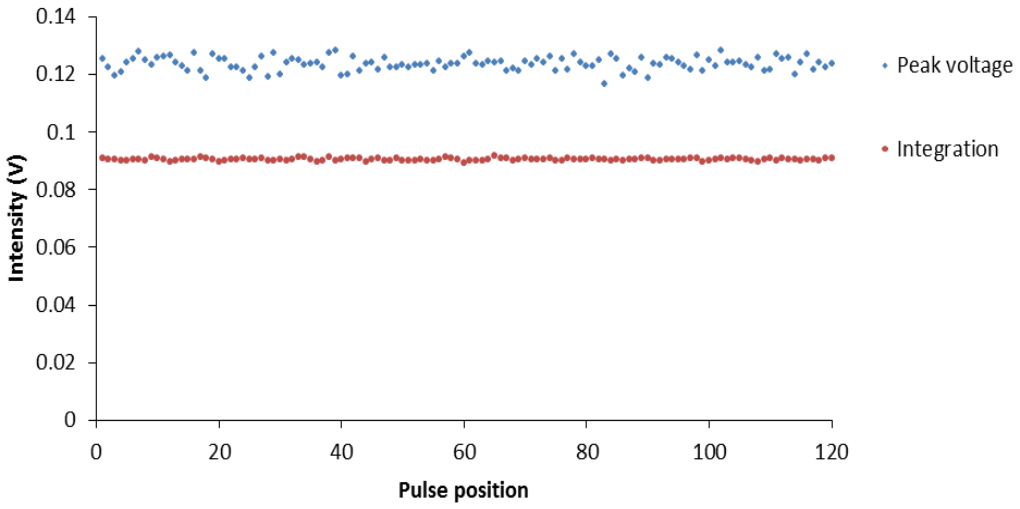

Figure 4.27. Pulse to Pulse noise of peak voltage measurement and integration measurement from 120 measured pulses.

Figure 4.27 shows the comparison of the noises of the peak voltage and integration measurements. Noise (SD) of peak voltage measurement is at level of 3 10^{-3} (V) and noise of integration measurement is 3 10^{-4} (V). The signal level of the integrations is reduced to be lower than the peak voltage when they are divided by 100 samples, but the noise is reduced at a much higher ratio than the signal. Therefore, the final signal-to-noise ratio (SNR) of the integration measurement ($SNR_{Integration}$ = 218.736) is improved compare to peak voltage measurement ($SNR_{PeakVoltage}$ = 52.831). In fact in this case, not only that the SNR of the one-hundredth of integration measurement is higher than SNR of peak voltage measurement as already investigated, but also it doesn't change if it is divided by 100 (the number of samples) or not, because when it is divided then the signal and the noise are divided by the same factor (of 100 samples).

4.4. SIGNAL TO NOISE RATIO

In this section, the SNR is investigated in 4 cases at chopping frequencies: 5 Hz, 4 Hz, 2.5 Hz and 0.5 Hz, all at 50% duty cycle, as shown in ***Figure 4.28***. In this figure, the voltage responses of the pyroelectric detector to the THz pulses at different chopping

frequencies were plotted against the sampling time in ms (with the same recording sampling rate of 1000 samples/s). The reason for choosing these frequencies is to compare the SNR when the pulse duration is at the rising time of the pyroelectric detector (4-5 Hz is equivalent to 100-125 ms) and those at shorter and longer time durations. The ultimate objective is to run at the frequency which gives a better SNR.

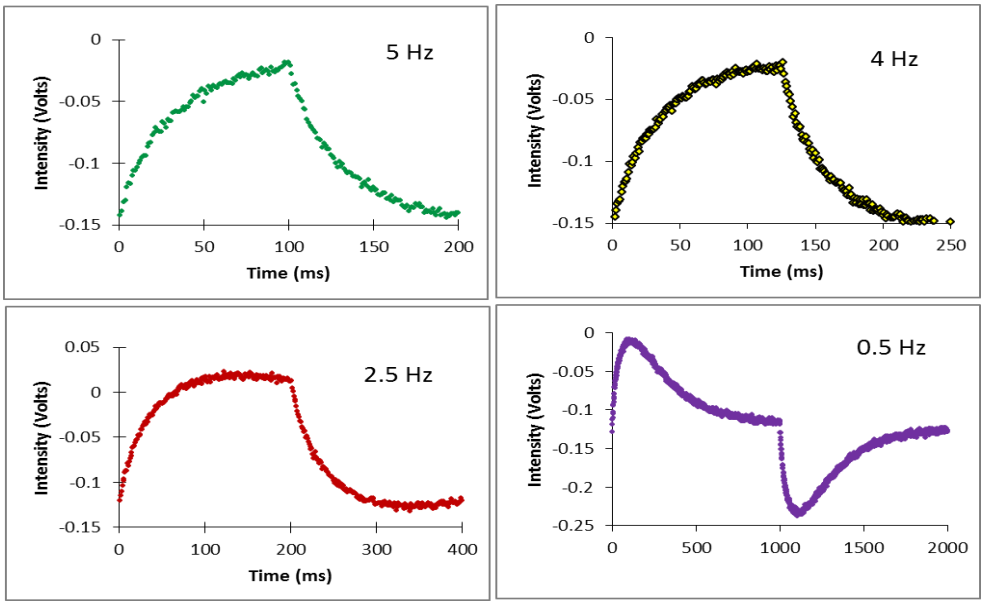

Figure 4.28. SNR will be measured in 4 cases of different pulse durations and chopping frequencies: 100 ms at 5 Hz, 125 ms at 4 Hz, 200 ms at 2.5 Hz and 1000 ms at 0.5 Hz.

Each frequency was investigated with the same amount of repeated pulses (60 pulses). The signals were measured as the integration of recorded samples during the "on" period of each pulse and then divided by the number of samples for each frequency case (e.g. 100 samples for 5 Hz frequency, 125 samples for 4 Hz, 200 samples for 2.5 Hz and 1000 samples for 0.5 Hz). The noises were then calculated as SD of 60 measured signals for each frequency case. Table 4.1 displays the calculated noises, signals and SNRs (in ratio and in decibel) of each frequency. Because the signals and the noises were measured in Volts, so the decibel values of SNRs are calculated as 20 times of the log of SNRs in ratio. The SNRs calculated are in the range of 20 to 50 dB. The highest SNRs are in the cases of 100 – 125 ms pulse durations (4 Hz and 5 Hz chopping frequencies). These SNRs are comparable to those in the literature as 40 dB in

[146], and 30 dB in [147]. Longer pulse durations give more noise and/or smaller signal (after dividing to the number of samples per pulse), so the final SNRs are smaller.

In ***Table 4.1***, it can be seen that the SNR of 4 Hz are highest among the other investigated frequencies. At this frequency, the pulse duration reaches the response time of the detector (Section 4.2). In addition, when taken into account the fact that the scanning time for one image acquisition in the 4-5 Hz case is a lot quicker than that of the slower frequency (e.g. for 50mm x 50mm area of 125x125 points, it takes 1.54 hours at 5 Hz; 1.93 hours at 4 Hz; 3.09 hours at 2.5 Hz and 15.43 hours at 0.5 Hz to finish one image), it is obvious that 4 Hz frequency is optimum for (integration) intensity measurement with this detector.

	Noise level (V)	Signal (V)	SNR	SNR (dB)
5 Hz 0.5 duty cycle	4.52E-4	9.06E-2	200.75	46.05
4 Hz 0.5 duty cycle	2.55E-4	9.82E-2	385.43	51.72
2.5 Hz 0.5 duty cycle	34.59E-4	12.62E-2	36.48	31.24
0.5 Hz 0.5 duty cycle	23.63E-4	5.59E-2	23.66	27.48

Table 4.1. SNRs of different chopping frequencies: 5 Hz, 4 Hz, 2.5 Hz and 0.5 Hz, all are of 50% duty cycle. Signals and noises were measured for 60 repeated pulses.

There are ways to improve the SNR such as: (i) increase the signal intensity (making measurements at higher THz intensity) or (ii) reduce noise level (using the averaging method). Increasing the signal intensity to increase the SNR (of pulse to pulse) is straight forward. Collimate well the THz beam so that it is not diverged after the source; setup the measuring systems nearer to the source to avoid intensity losing due to the air absorption are things we can do immediately. ***Figure 4.29*** shows that the SNR was improved by ~ 10 times, when the signal intensity is increased to ~ 10 times. While the signal was increased, it is noticed that the pulse to pulse noise level doesn't changed much; of about 3 10^{-4} V.

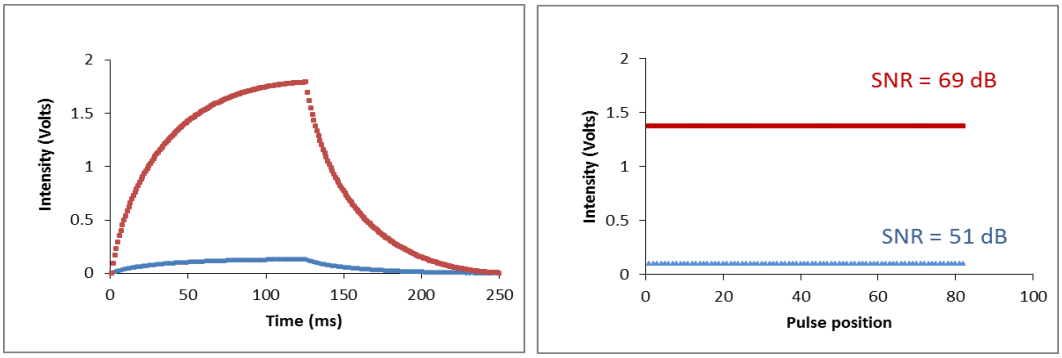

Figure 4.29. Right: Intensity responses (averaged of 82 responses) of the detector to the THz pulses of a diverse beam (blue) and a focused beam (red); Left: Integrations per 125 samples of 82 pulses at those individual cases. The numbers present the SNR of pulse to pulse measurements in each case.

In addition to the increasing of the signal intensity, reducing noise is another solution to improve the SNR. The most common way is by the averaging method. For example in here, the samples were averaged over several pulses (9 pulses) and the noise was reduced clearly as compared and shown in the left and right graphs in ***Figure 4.30***. The SNR was then improved from 51 dB to 58 dB (equivalent to more than 2 times bigger in S/N ratio).

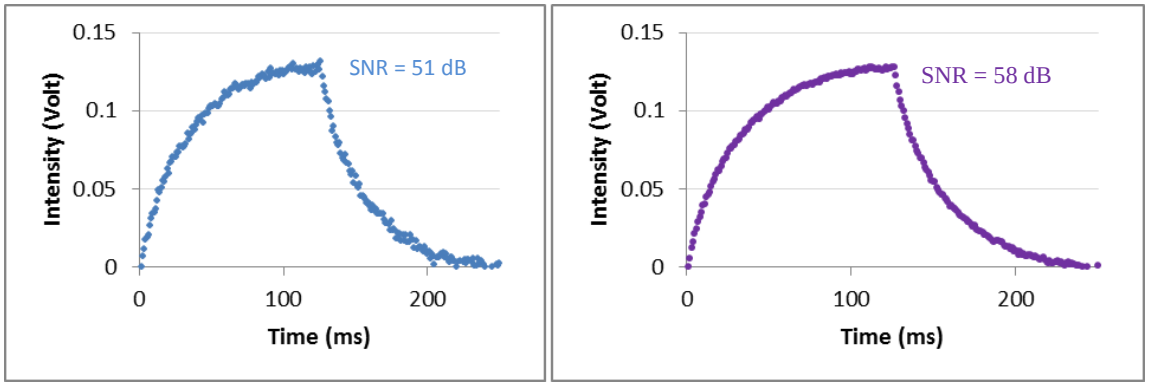

Figure 4.30. Improving the SNR by averaging method. Left: Single response (SNR = 51 dB); Right: Averaged of 9 response (SNR = 58 dB).

However, even when one point (one pixel in a 2D scanning image) is measured by one THz pulse, it takes quite a long time to finish one scanning image (several hours) while running at 4 Hz chopping frequency. So averaging several pulses for one point measurement is not very practical. Also, in our later measurements, the integrated signal

did not be subtracted to the number of samples (125 samples) but the original integrated data were used instead. In that case, the signal is bigger, the noise is bigger, but the SNR does not change if the signal is subtracted to the number of samples or not.

4.5. LINEARITY

This section studies the linearity in the response of the pyroelectric detector to the changing in the output power of the THz source, which is controlled by applying voltages to the UCA. This is linearity comparison of the combination of the source and detector – as with the noise that has been studied above. The experiment is illustrated in ***Figure 4.31***. The pyroelectric detector was put on the optical axis and in the output of the source (in front of the diagonal horn), at the positions P1 and P2. At each of these detector positions, the measurements were made while a range of voltages were applied to the UCA port of the THz source to change the THz output power. Voltages applied to the UCA are in the range of 0 to 5 volts. 0 volts corresponds to no attenuation and 5 volts corresponds to maximum attenuation. Voltages out of this range may damage the attenuator.

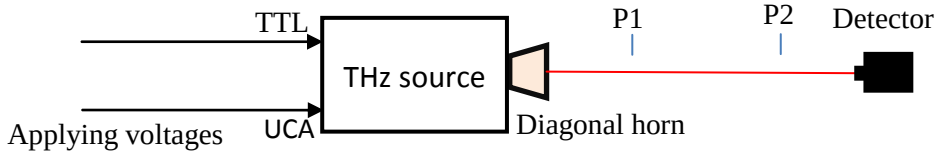

Figure 4.31. Schema of the experiment for studying of the linearity. P1 and P2 are two positions of the pyroelectric detector. Applied voltages to UCA were from 0 to 5 volts; TTL signal controlled the THz source to be running at 0.25 Hz 50% duty cycle.

The source was running at 0.25 Hz 50% duty cycle so that the whole voltage pulse responses of the detector are captured, but the samples were integrated within the rise time of the detector only, which is during the first 125 ms of the pulse. The integration data were kept originally and were not divided by the number of samples (125 samples), so the integration unit would be in Volt multiples by millisecond (V.ms). ***Figure 4.32*** shows the voltage responses of the detector versus sampling time when the detector was at positions P1. The presented responses are averaged over several pulses for a smooth

presentation. The peak voltage can be seen decreased with the increasing voltage applied to the UCA port of the source.

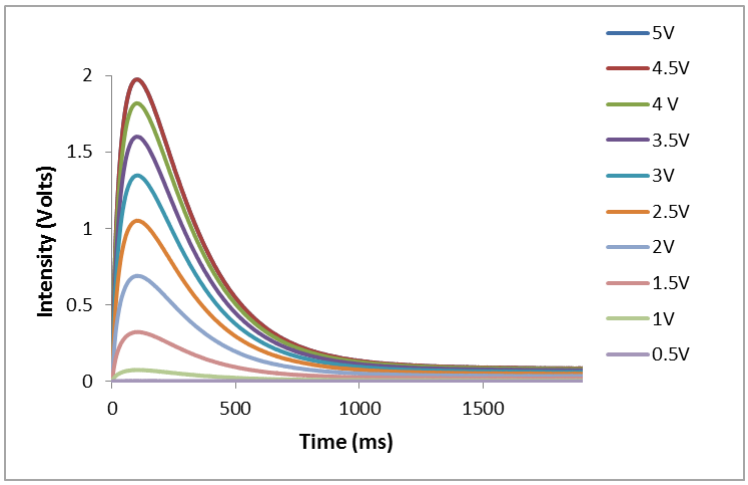

Figure 4.32. Responses of the pyroelectric detector to output THz pulses when different voltages were applied to UCA port of the source

In order to verify the validation of the integration process in the intensity measurement, the calculated integration data were plotted against the peak voltage data and the graph is presented in ***Figure 4.33***. It is logical that the THz intensity is weaker when the detector is moved further from the source (from position P1 to position P2) due to the divergence of the beam and the lost power by the environmental (water) absorption.

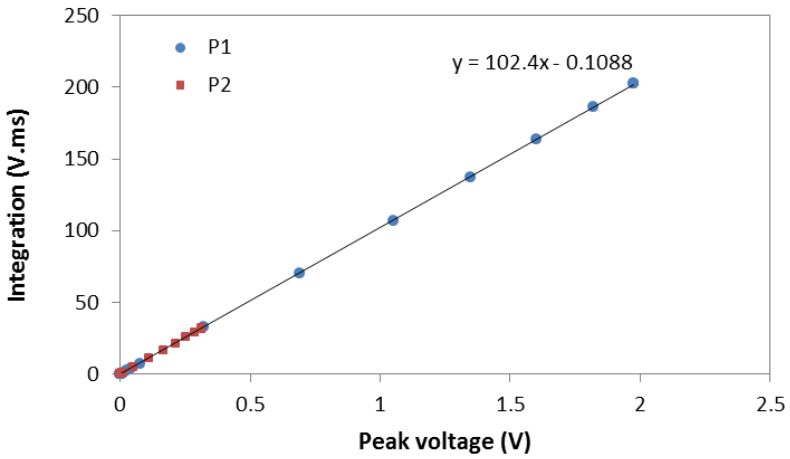

Figure 4.33.Calculated integration intensity versus peak voltage for two intensity ranges of THz radiation when the detector was at position P1 (blue circle) and P2 (red square).

The graph shows that there is a linear relationship between the integration and the peak voltage of this pyroelectric detector's response and the integration equal to ~ 102 times the equivalent peak voltage in both cases. This fact enables us to use either integration data or peak voltage for intensity measurement; yet using integration intensity has an advantage of having a higher SNR (which was investigated in Section 4.3).

Figure 4.34 graphs the dependence of the integration intensity to the UCA applied voltage. Graph (a) is experimental result and graph (b) is the calibrated data of the source company (the VDI). The consistent shape of the detector response even at high or low THz power ranges (at P1 or P2) in ***Figure 4.34***(a) gives another proof for the linearity in measurement of the source – detector combination. Though there are differences in the form of the experimental and the calibrated curves, there is a coherent tune in the dependence of the THz intensity to the UCA applied voltage. The variation between the two graphs is expected because the presented data in the VDI's graph was measured under different test conditions and it is noticed in the manual of the source that the exact shape of the curves may vary depending on many different conditions. And yet our measurements were made at 375 GHz and not at the frequencies the VDI used.

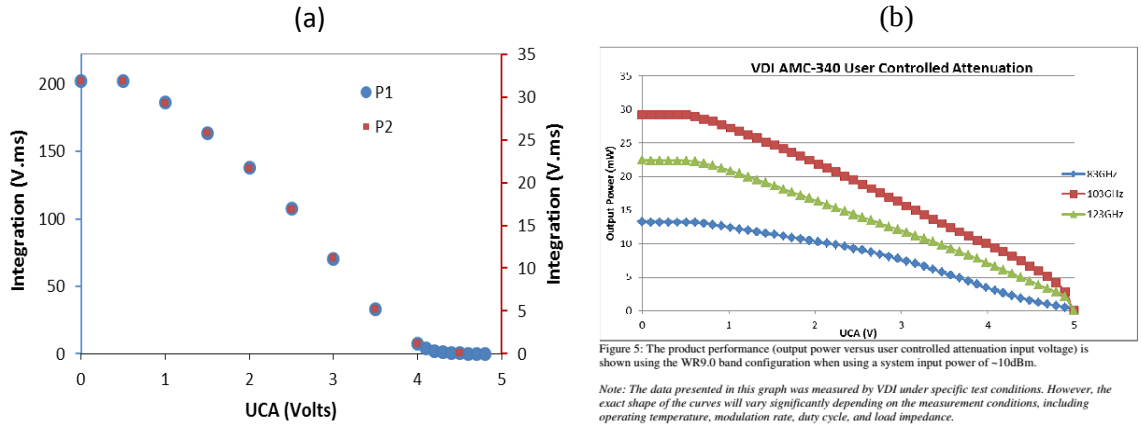

Figure 4.34. The dependence of the detector intensity response to the UCA applied voltage for two investigated detector position P1 and P2.Graph (a) is experimental result and graph (b) is VDI's calibrated data.

In conclusion, the integration data can be used alternatively to the peak voltage as they have a linear relationship, with a ratio of ~ 102 times bigger than the peak

voltage value. The response of the detector to the THz output radiation from the source is linearity with consistent dependent shape of the detector response to the UCA applied voltage even when the THz radiation is at low or high level.

4.6. USING DETECTOR TO CHARACTERISE THE OUTPUT OF THE THz SOURCE

4.6.1. The Scanning System

A system was built, which enables 2D and/or 3D scanning measurements to be taken with the 1D pyroelectric detector. The core of the system are three-1D translation stages, combined together to form a multi-axis system which is controlled from a single PC-based software programme. The translation stages are of 100 mm travel range with a minimum repeatable incremental movement of 2 μm. They are in the range of high speed step motor translation stages from Thorlabs (Appendix A.11) which the maximum velocity is 30 mm/s and maximum acceleration is 30 mm/s^2. Two of the three translation stages were combined by a right-angle bracket to make a xy configuration, for 2D scanning measurements (***Figure 4.35***). The pyroelectric detector was posted on the y stage. The third stage was used for applications which need to make phase-stepping.

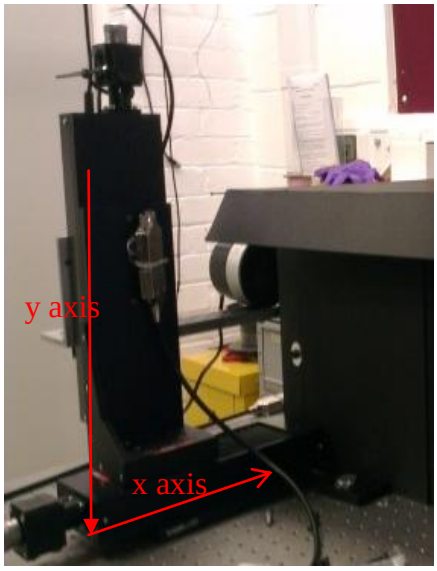

Figure 4.35. xy configuration of two-1D translation stage.

The PC-based software programme was written using LabVIEW as a Graphical User Interface (GUI) environment, to control and to interact directly with the controller box of the stages, via the USB communication protocol. The data acquiring and analysing process was also coupled in this programme to record the data in the form of a readable file (text, word, excel, or notepad). Again, a digital pulse train was used to trigger the THz source, as well as the data acquisition. In addition to that, the same digital pulse train used to trigger the THz source is used to trigger the stages' movement to start at the right moment in the time scale. In our measurements, the data was integrated only for a half voltage response pulse of the detector, at the period when the source is triggered "on". Time scale for one point measurement is depicted as in ***Figure 4.36***. The integration process takes 125 ms of the first "on" period of the source. The moving of the stages takes 200 ms for 0.3 to 0.4 mm step size. After that there is a waiting time for the stages to get stable, before a new data acquisition and recording process is started, at the rising of the third "on" period of the source. In conclusion, when it is a 2D scanning application, it takes 500 ms to finish the measurement at each point. A friendly user interface was designed for the interaction between the users and the main controlling program.

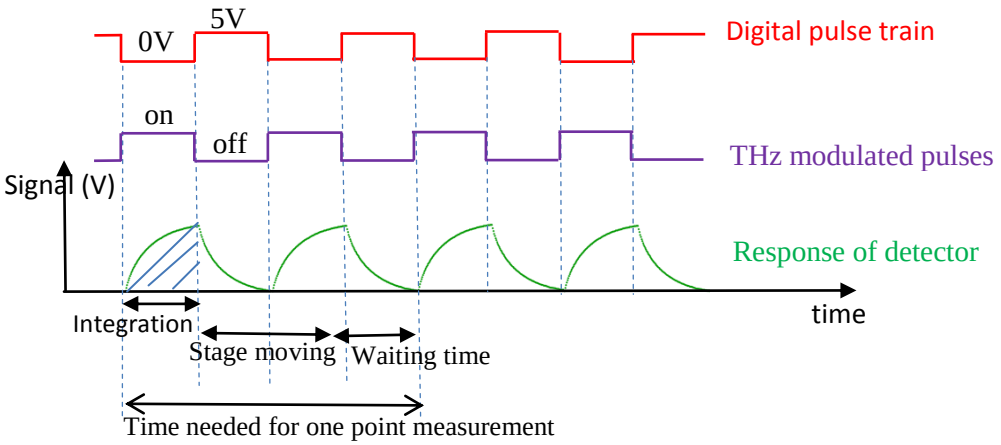

Figure 4.36. Time scale for one point scanning measurement.

To run the three stages smoothly, a strategy for how and when each of them will move is needed. A matrix of stages' positions was created and inserted into the main control programme to help the moving commands. In the case of 2D scanning, the stage in y direction (see ***Figure 4.35***) was programmed to run point to point until it finishes one line. Then the x stage is moved to the nearest of current position before the y stage starts a new scanning line, as described in ***Figure 4.37*** 2D case. In that case, the y stage

runs more frequently than the x stage. This is better than the inverse situation, which the x stage runs more frequently, because the x stage has to carry all the weight of the y stage and the detector.

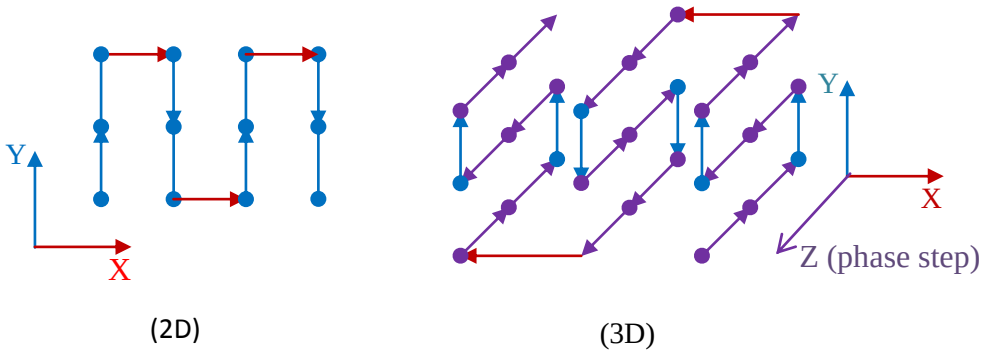

(2D) (3D)

Figure 4.37. Matrices of stage positions for 2D and 3D scanning measurements.

For interferometry applications, with phase-stepping movement, 3D scanning is needed. In that case, the z stage (phase-step stage) was chosen for running more frequently than the others because the step size of the phase is normally small. Besides, it does not carry heavy weights, compared to the other two stages. ***Figure 4.37*** (3D) describes the position matrix of 3D scanning of the stages.

4.6.2. Beam Profile Characterisation

Measurement and analysis of output beam characteristics is essential for our applications, particularly when the source is setup for the first time in our lab. Beam characterising involves measurement of the beam-profile which is the spatial energy (or power) distribution of the beam. According to the product description document of Virginia Diodes, the THz output beam has a profile "84% Gaussicity". We have used the scanning system and the pyroelectric detector described above to capture the 2D profile of the output beam at different distances from the source to verify.

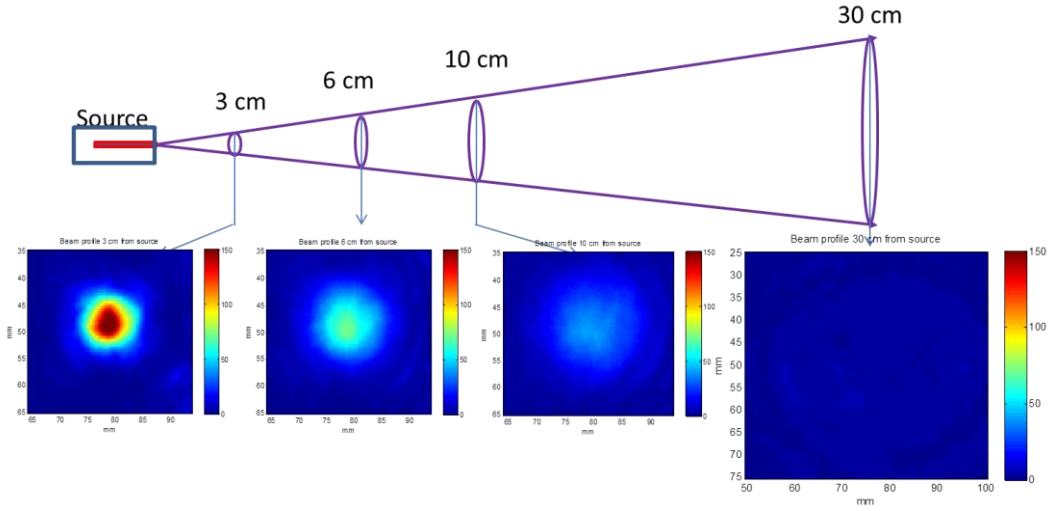

Figure 4.38. 2D beam profile of the THz multipliers at different distances from the source.

Figure 4.38 presents the output beam profile of the THz multiplier source at different positions along the optical axis (Z axis). The distance from the central beam to the optical table was 15 cm in height. At positions 3, 6 and 10 cm the image size is 60x60 pixels and pixel size is 0.5 mm. At position 30 cm, the image size is 50x50 pixels and pixel size is 1 mm. For these measurements, a 0.5 mm diameter pinhole was mounted at the entrance of the pyroelectric detector to reduce the amount of spatial noise to be integrated. At smaller pinhole size (3mm / 1mm / 0.5mm) the signal was reduced so drastically that it becomes a disadvantage, as the contrast of the images was reduced as well.

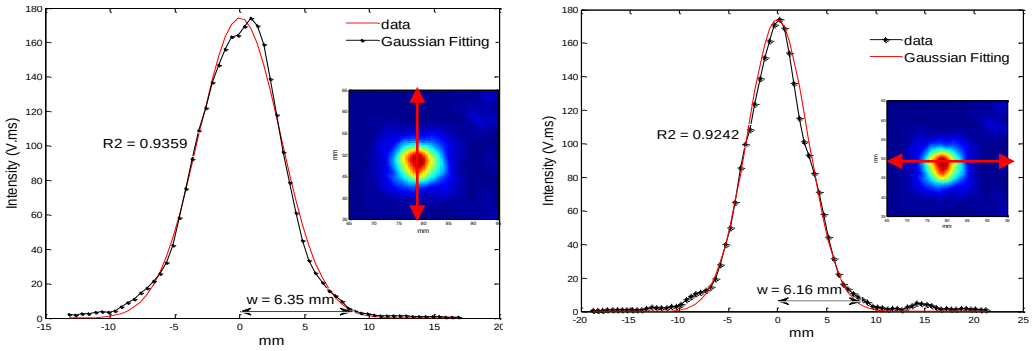

Figure 4.39. Gaussian fitting of the measured beam profile, 3 cm distance from source.

In order to verify the matching up of the output beam with the Gaussian profile, we carried out several calculations and analyses on these measured beam profiles. First

of all, a modulation of the Gaussian beam was calculated to fit the horizontal and vertical lines of the beam profile, based on the real beam parameters at 3 cm distance. The Gaussian beam is modulated based on the relationship between the beam radius and the beam intensity of a Gaussian shaped beam. The equation that describes this relationship is as follows:

$$\boldsymbol{I(x,y) = I_0 \exp\left(\frac{-2x^2}{w_x^2}\right) \exp\left(\frac{-2y^2}{w_y^2}\right)} \quad (4.1)$$

- w_x, w_y : $1/e^2$ beam radius in x and y direction respectively
- I_0 : Peak intensity of two directions x and y.

Thus the total output power of the beam is obtained by integrating the intensity I(x,y):

$$\boldsymbol{P_{TOT} = I_0 \int_{-\infty}^{+\infty} \exp\left(\frac{-2x^2}{w_x^2}\right) dx \int_{-\infty}^{+\infty} \exp\left(\frac{-2y^2}{w_y^2}\right) dy = \frac{\pi}{2} I_0 w_x w_y} \quad (4.2)$$

- P_{TOT} : total power of the beam

The peak intensity I_0 of the two directions was extracted from the above measured beam profile and it equalled to 348.6 V.ms with a detector size of 2x2 mm^2. Dividing this intensity by the detector's sensitivity ($1.28\ 10^5$ V/W) will convert this peak intensity to energy in Joules. The power intensity is then calculated by multiplying the energy with the source's modulated frequency (4 Hz). Knowing the peak intensities of each direction enables us to calculate a Gaussian profile to fit with the experimental measurement as presented in ***Figure 4.39*** applied for horizontal and vertical (x and y) profiles of the 3 cm distance beam. These Gaussian fittings have:

w_x = 6.16 mm (horizontal radius)

w_y = 6.35 mm (vertical radius)

Applying these parameters to the equation (4.2), gives a result of P_{TOT} equals to 0.17 mW. However, this is actually an average output power of the pulsed laser beam, whereas the calibration in the user guide of VDI, the power was measured for continuous (cw) output, which gives a number of ~0.4 mW for 375 GHz, as shown in ***Figure 4.19***. To compare these numbers together, we take the fact that our pulses are 50% duty cycle, what we measured is about ½ of the cw output power. So by multiplying the result of P_{TOT} we have got by 2 gives us 0.34 mW, which is within ~15% difference from the output power that the laser company calibrated for our source (~ 0.4 mW from the calibrated data in ***Figure 4.19***).

Another parameter of the beam that we can get from analysing these measured beam profiles is the beam waist which is the smallest beam radius of a Gaussian beam along the propagation direction. This parameter defines the resolutions of the measuring system.

A Gaussian beam has the wave fronts of a same value of phase are spherical which cause the beam to diverge. The phase is plane at the position of smallest beam diameter $2w_0$. From this position, the beam radius w (1/2 of beam diameter) increases as it travels along the Z axis (

Figure 4.40). The beam diameter changes as a function of its position on this axis, which is described by the equation:

$$w_z = w_0\sqrt{1+\left(\frac{\lambda z}{\pi w_0^2}\right)^2} \tag{4.3}$$

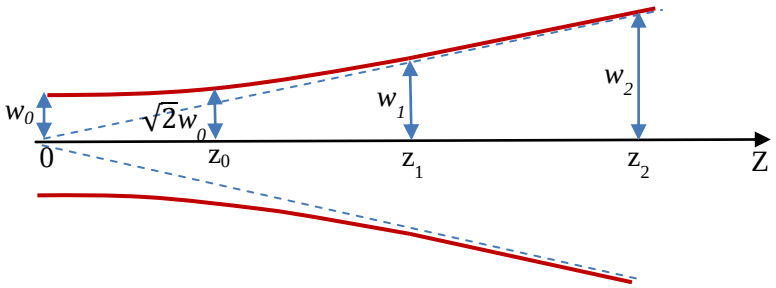

Figure 4.40. Propagation of a Gaussian beam.

By using equation (4.3), the smallest spot size w_0 can be calculated from two measured beam radius w_1 and w_2 at location z_1 and z_2 as:

$$w_0 = \frac{\lambda}{\pi}\sqrt{\frac{z_2^2 - z_1^2}{w_2^2 - w_1^2}} \tag{4.4}$$

Care should be taken that z is measured from the beam waist. In the case of a laser, the beam waist position is approximately in the centre of the laser's cavity. In our case, we assume that the beam waist position is at the last point of the wave guide before it is radiated into space via the diagonal horn. So the z position of each beam profile needs to include the length of the diagonal horn. The beam positions that have been indicated above (30 mm, 60 mm and 100 mm) were calculated from that point.

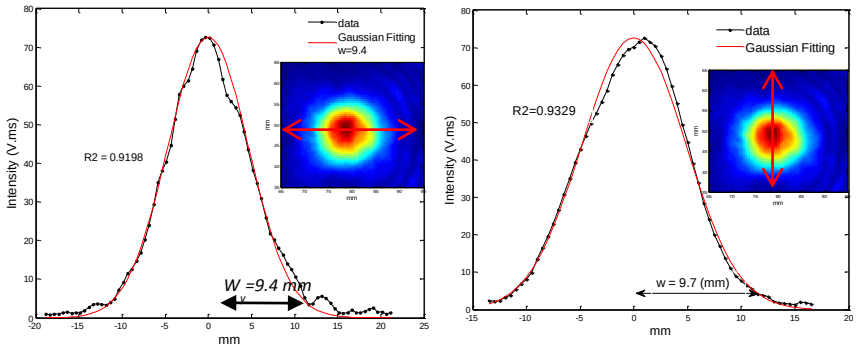

Figure 4.41. Gaussian fitting for x and y axis of the measured beam profile at 60 mm.

At 30 mm position, the Gaussian fitting of the beam profile gives the beam's horizontal radius w_{x1} 6.16 mm and vertical radius w_{y1} 6.35 mm. A similar calculation for the measured beam at 60 mm position was taken as in ***Figure 4.41*** which gives w_{x2} 9.4 mm and w_{y2} 9.7 mm respectively. Applying these numbers to the equation (4.4) for the THz wavelength of 0.8 mm, the beam waist diameter is calculated as equal to 1.9 mm and 1.8 mm in horizontal and vertical directions respectively. These numbers match up with the calibrated number from the source's company (beam waist of 1.9 mm for multiplier/diagonal horn model WR-2.8).

Knowing the beam waist, we can also estimate the Rayleigh range r_0 at which the beam radius is as big as $\sqrt{2}w_0$ and is given by (in book such as [148]):

$$z_0 = \frac{\pi w_0^2}{\lambda} \tag{4.5}$$

Calculating by this equation gives an estimated depth of focus of 12.7 mm and 14.2 mm in x and y directions respectively. As the beam waist is the radius of minimum spot size, according to the Rayleigh criterion, it is the lateral resolution and the depth of focus for the axial resolution measuring system, using this source.

4.7. TRANSMISSION PROPERTIES OF SOME MATERIALS OF INTEREST

Figure 4.42 shows the intensity against frequency measurement. A test of frequency scanning in air was repeated after every 15 minutes, over duration of 120 minutes. The frequency was scanned in a range of 240- 380 GHz with step size 1.35 GHz output of multipliers, which is 0.05 GHz step size in the synthesiser (27x 0.05 = 1.35). The minimum tuneable step size of the VDI synthesiser is 20 Hz. Noise in every frequency

point is shown as an error bar at that point. The noises are small and of 0.1-0.4 V.ms, so the frequency measurement is stable.

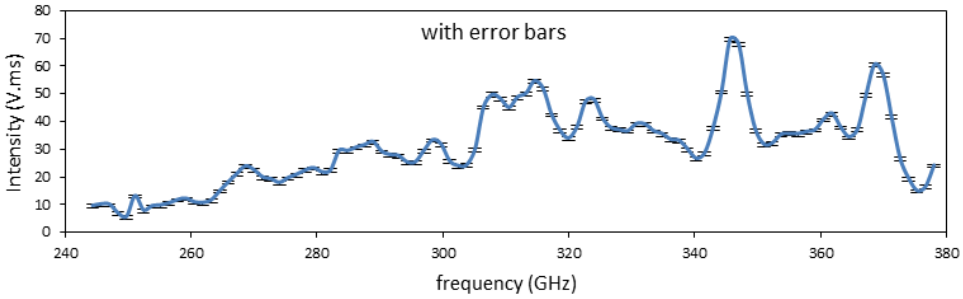

Figure 4.42. Noise in frequency scanning: measured frequencies with error bars.

A simple experiment was built to measure the transmission of some materials of interest. The measured samples are basically the same samples which were investigated in Chapter 3 with the intra-cavity OPO laser and in a different THz frequency range. The experimental setup is schematically depicted in ***Figure 4.43***. The divergent THz beam was collimated by a plano-convex lens of 10 cm focal length. The entrance of the detector was aligned right after a small pinhole. For each transmission measurement, a reference of frequency measurement in air was recorded before the object is put in the setup and is placed right in front of the pinhole.

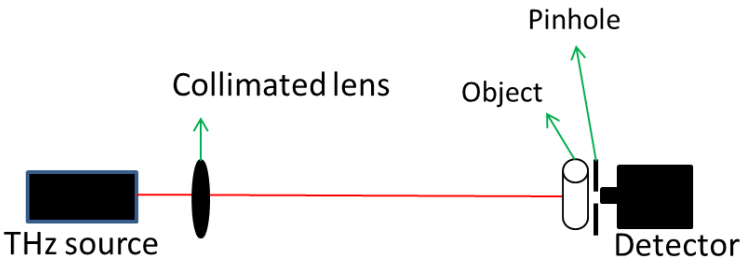

Figure 4.43. Schema of the experimental setup for transmission measurement of specimens of interest.

Results are shown in ***Figure 4.44***. Compared to the transmission spectra of the same samples, which were shown in chapter 3, the YTZP and YSZ are not transmitted in a higher THz range (~1.2- 2.5 THz), but they are transmitted in the lower frequency range of this THz source (0.24 – 0.38 THz). This information gives us some ideas of the THz regions, where we can use, to study these materials. For future work, reflectometry

and interferometry may be used in phase/thickness measurement of the thermal barrier coating in the tuneable range of this THz source.

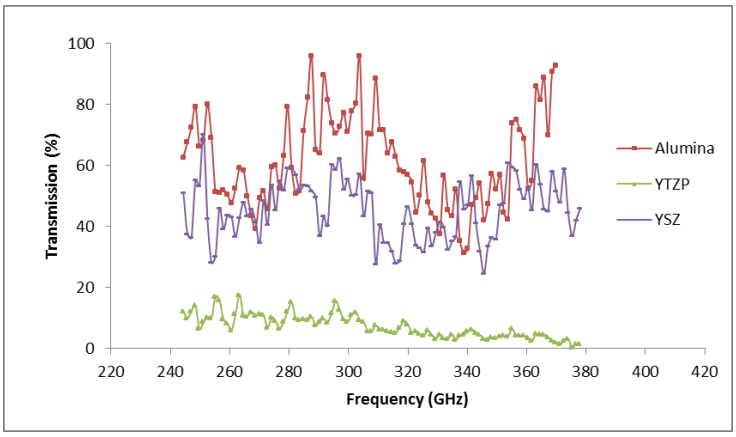

Figure 4.44. Transmission properties of some samples of interest in tuneable range of the THz source. Thicknesses of the specimens are: Alumina 0.65 mm; YTZP 16.08 mm; YSZ 0.42 mm.

4.8. IMAGING SYSTEM

An imaging system was built which was based on the confocal design for imaging applications. The system is schematically depicted in ***Figure 4.45***. The THz output beam from the source was collimated by a parabolic mirror, M0, before it is collimated and focused into the object plane P2, by the first lens L1. The lenses L2 and L3 are identical and enable the light pattern in P2 to be imaged one-to-one at detector plane P3. A pinhole was placed in front of the detector to remove the image's diffraction pattern, which helps to improve the resolution of the measurements. The system takes images in a single point of the sample at a time. The measured objects were posted on 2D translation stages to be scanned automatically, while the pyroelectric detector was fixed at plane P3 after the pinhole A.

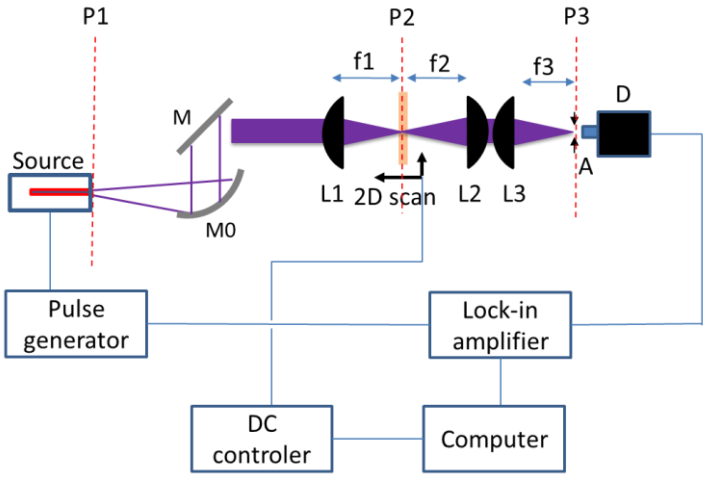

Figure 4.45. Schematic for experimental setup of imaging system: f1 = f2 = f3 = 75 mm.

The size of the pinhole A was chosen to be three times of the beam waist which was estimated in the last section, so the size is 6 mm. The diffraction limit of the system is calculated to predict the beam spot size at the object plane P2 and the resolutions for the system. This limit is the size of Airy disk which is calculated by well-known equation:

$$A = 2.44\frac{\lambda f}{D} \tag{4.6}$$

Where λ is THz wavelength (0.8 mm), f is focal length of the objective lens (75 mm), and D is beam diameter when it reached the objective lens (~ 40 mm). This gives a predicted spot size of 3.66 mm.

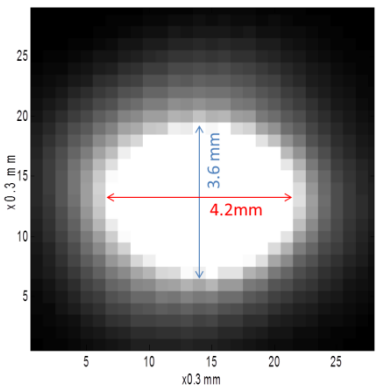

Figure 4.46. Image of beam profile at object plane P2.

In order to verify the validity of this calculation and to check the quality of the alignment, the beam spot size at object plane P2 was imaged. The image result is shown in ***Figure 4.46***. We have got the spot size slightly bigger than the estimated beam waist and the calculated diffraction limit of the system. This may be due to the M2 factor that impacts on axial and lateral resolutions of a real Gaussian beam (which makes lateral resolutions bigger and axial resolution shorter). So, according to Rayleigh criteria, the resolutions of the imaging system are expected to be 2.1 mm and 1.9 mm for horizontal and vertical directions respectively. According to Shannon criteria, the sampling step size that we need to setup for the scanning system is smaller than 1 mm. In our system, step sizes of 0.4 mm were chosen.

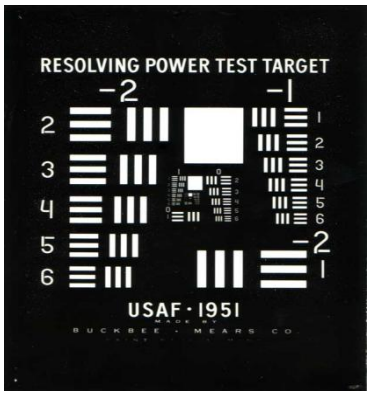

Figure 4.47. 1951 USAF resolution target (image source: Wikipedia).

Figure 4.47 is a 1951 USAF resolution target which was used to test the spatial frequency response (or modulation transfer function) compared to the real spatial frequency. The target includes of 6 groups displayed in three layers on the surface of the target. Each group consists of 6 elements numbered from 1 to 6 which decreasing in size as the element number increases. The resolving powers of the test elements are expressed in number of line pairs per millimetre (lp/mm).

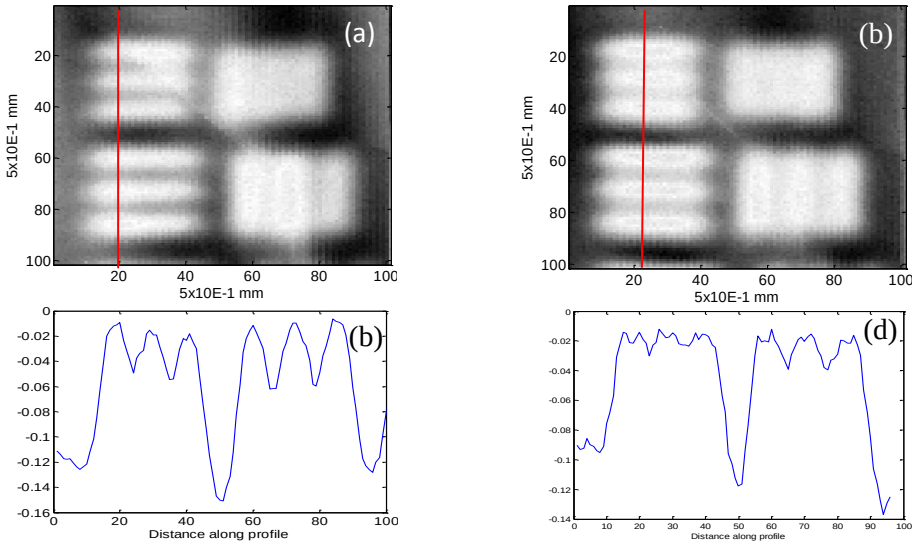

Figure 4.48. THz scanning image and a vertical profile (the red lines) of the group -2, element 5 and 6 of a 1951 USAF resolution target with (a, c) and without (b, d) detector pinhole.

Figure 4.48 is a comparison between the THz images of a part of the resolution target (Group -2, element 5 and 6) when they were scanned with and without the detector pinhole. Obviously the image scanned with the detector pinhole shows a better quality and contrast.

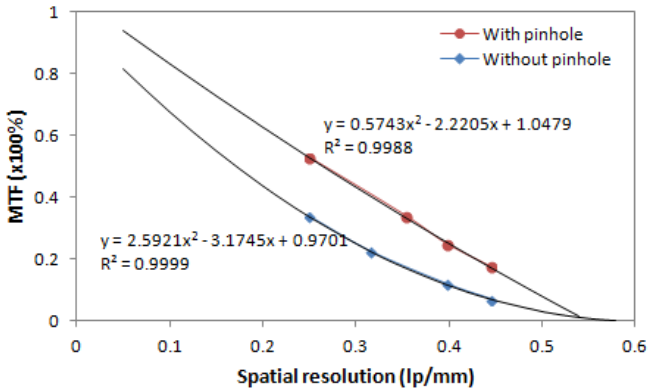

Figure 4.49. Modulation transfer function (%) versus spatial resolution (lp/mm) measured with and without pinhole (red and blue lines respectively). Second order polynomial fitting to the measured data are presented by black lines with corresponding equations and correlation coefficients.

The modulation transfer function (MTF) was introduced to calibrate the quality of the response images compared to the real spatial frequency of the measured test target element. The equation for MTF is derived from the contrast C_f at a specific spatial frequency f, which is calculated as:

$$C_f = \frac{V_{max} - V_{min}}{V_{max} + V_{min}} \quad (4.7)$$

Where V_{max} and V_{min} are the maximum and minimum of the normalised intensities. The MTF is then calculated as:

$$MTF = 100\% \frac{C_f}{C_0} \quad (4.8)$$

With C_0 is the maximum contrast measured at low frequencies (e.g. $V_{max} \approx 1$; $V_{min} \approx 0$).

Figure 4.49 graphs the measured MTF versus the spatial frequency with (red line) and without (blue line) the detector pinhole. When the images are scanned without the pinhole, the MTF decreased to low level (< 10% contrast) at the spatial frequency of ~ 0.45 lp/mm (~ 2 mm line width), it is hard to resolve the lines. Whereas when there was detector pinhole, the MTF is improved to ~ 20% contrast at the same spatial frequency. This spatial frequency is near the resolution limit calculated above (and as seen in the image of the spot size ***Figure 4.46***). So the resolving power of the system calibrated by the resolution test target corresponds well with the calculated number.

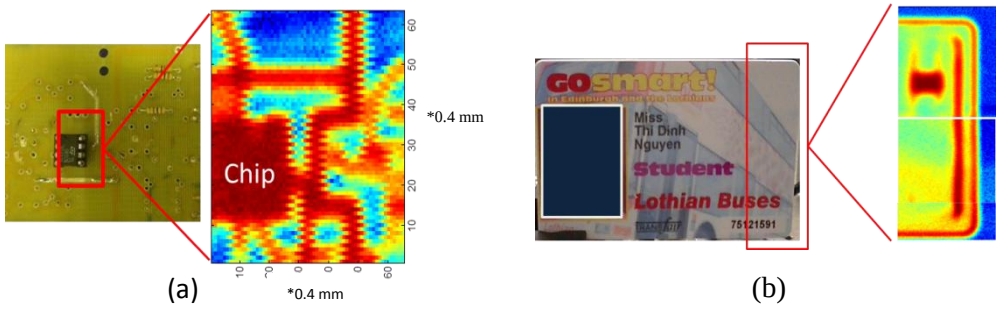

Figure 4.50. Images of a circuit board (a) and Edinburgh bus card (b).

Some imaging results are presented in ***Figure 4.50*** for a circuit board and an Edinburgh bus card. From both the images, we can see that the THz radiation is able to be transmitted through the covering plastic layers; thus, we can see the structure inside of the objects. The metal wire and the intelligent chip of the bus card are now visible.

4.9. INTERFEROMETR

Current research on interferometry is focused on the characterisation of the system and some initial results on thickness measurement. Subsection 4.9.1 describes the alignment and experimental setup. The intensity noise and phase noise will be studied in

subsection 4.9.2 with 2D phase noise map is presented and discussed in subsection 4.9.3. Subsection 4.9.4 examples an application of the interferometer on thickness measurement.

4.9.1. Experimental System

The experiments are based on Mach-Zehnder interferometer which is illustrated in ***Figure 4.51***(a). The tunable THz source was operating at a chosen frequency of 375 GHz as mentioned at the beginning of the chapter. The diverging output beam was collimated by a 50 mm diameter, 75 mm focal length plano-convex Teflon lens. The light beam is split into reference beam and object beam by a High Resistivity Float zone Silicon (HRFZ Si) beam splitter. A second beam splitter combines the reference beam and the object beam, which now carries information of the measured object, together at the entrance of the detector. Reference mirror (RM) and object mirror (OM) were aligned to be at $\theta = 45^{o}$, compared to the incident beams. Moving reference mirror by a distance d produced a path length change of $(2d \cos\theta)$. Measurements were made by scanning the single point pyroelectric detector, across the output interference beam, by two motorised translation stages in an X-Y or X-Y-Z configurations as described above. The reference mirror was posted on top of the Z translation stage, which can move in a direction perpendicular to the mirror plane. The changing of reference mirror position corresponds to the change in the phase of the reference beam, which in turn changed the interference pattern due to the change of phase difference between reference beam and object beam ***Figure 4.51***(b) shows vertical profile of interferogram intensity changing versus reference mirror positions.

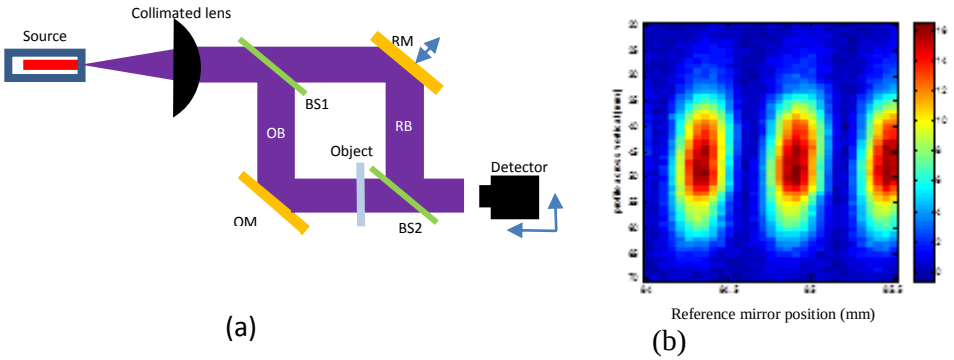

Figure 4.51. (a) Schemas of the experimental setup based on Mach-Zehnder interferometer. BS1 and BS2 are beam splitters. RM and OM are flat, gold coated mirrors. RM is reference mirror, OM is object mirror. (b) Interference intensity variation of vertical profile of interferogram versus position of reference mirror (phase change).

Figure 4.52(b) is the interference intensity variation of a point near the centre of the interferogram versus reference mirror positions, and the intensities at the same point of object and reference beams. To record these data, the detector was fixed at the centre of the interference beam while the reference mirror was scanned by the Z translation stage and the recording system recorded datum value at every reference mirror position. The object beam was blocked while recording the intensity for the reference beam and vice versa. Definitely the object beam is stable because the moving of reference mirror doesn't effect on it, but from the graph we can also see that the reference intensity is considered to be stable in the range of several fringes to the non-normal movement of reference mirror.

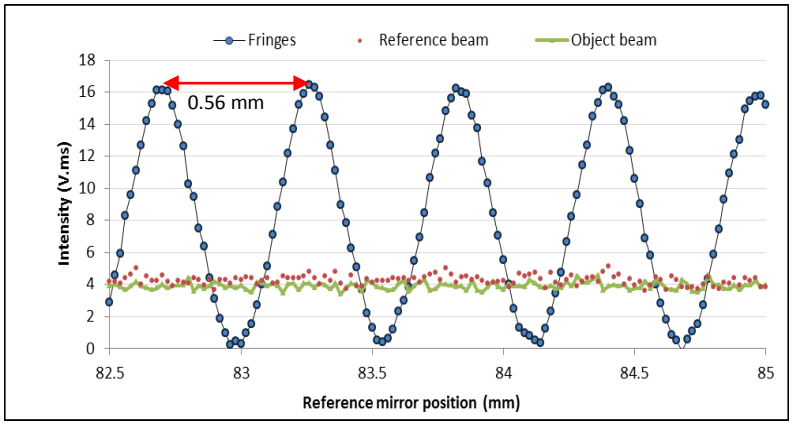

Figure 4.52. Interference intensity variation, object intensity and interference intensity of a point near the centre of the interferogram versus position of reference mirror (phase change).

The movement of reference mirror between two successive peaks of the fringes was $\Delta d = 0.56$ mm in the air, which corresponds to the change of one wavelength in optical path length. This observed length matches perfectly with the calculated value for $\theta = 45°$ and $\lambda = 0.8$ mm.

4.9.2. Intensity noise and phase noise

In this sub-section, 1D (one horizontal line) characteristic of the phase noise associated with the intensity noise and modulation amplitude of the interference pattern were investigated in order to understand the effects of noise in the later results. We start with the intensity noise of the separated object and reference beams.

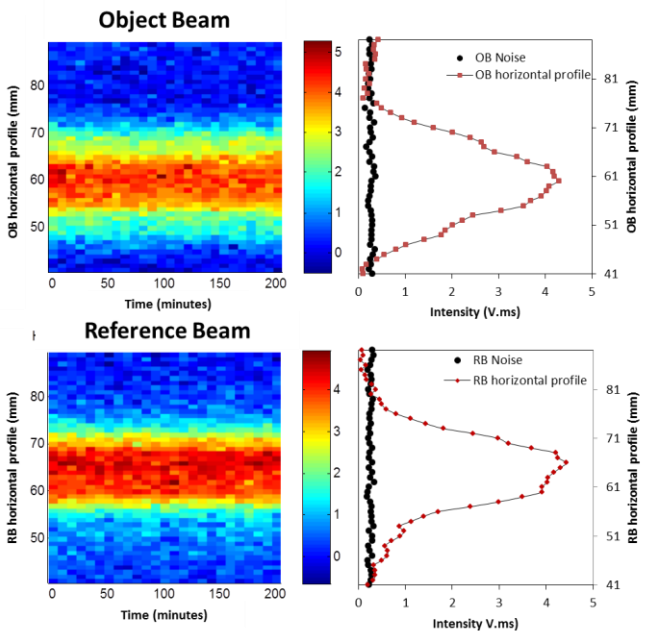

Figure 4.53. Horizontal profile of object beam versus time (left), and noise calculated at each pixel across the profile (black dots in the right).

In ***Figure 4.53***, intensity variation of horizontal profiles of object beam (OB) and reference beam (RB) versus time is imaged (left), and the noise at each pixel on the profile is calculated and displayed in the graphs on the right. The graphs show that the reference beam noise δ_{RB} and object beam noise δ_{OB} keep at the same level across the measured profiles no matter the fact that the intensity was changing and was reaching much higher level in the middle of the beam. This level is of 0.26 V.ms, which is within 5% of the maximum intensity, for both object beam and reference beam. It means that the noise level doesn't change with the intensity level. This is consistent with previous measurements and is different from CCD and CMOS detectors where the noise increases with intensity.

Meanwhile the object beam and reference beam noise levels don't change with the changing of the THz beam intensity, the phase noise does. A proof for this relation is shown in ***Figure 4.54***(b) where the phase noise at each pixel across the horizontal profile of the interferogram is plotted versus measured position in the profile. This phase noise is extracted from the repeating phases which are imaged in ***Figure 4.54***(a). This phase in turn is calculated from repeat measurement of intensities at successive phase lags of 0, $\frac{\pi}{2}$, π, $\frac{3\pi}{2}$ (rads).

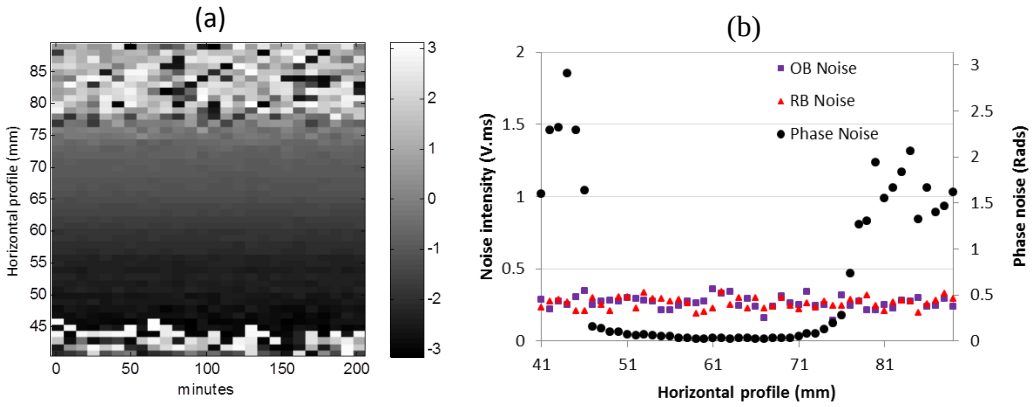

Figure 4.54. Horizontal profile of the phase map versus time (a), and noise calculated at each pixel across the profile (black dots in (b)).

The four frames of intensity data of the four phase-steps are recorded as:

$$I_1 = I_{OB} + I_{RB} + 2\sqrt{I_{OB}I_{RB}}\cos(\Phi) \tag{4.8}$$

$$I_2 = I_{OB} + I_{RB} + 2\sqrt{I_{OB}I_{RB}}\cos\left(\Phi + \frac{\pi}{2}\right) \tag{4.9}$$

$$I_3 = I_{OB} + I_{RB} + 2\sqrt{I_{OB}I_{RB}}\cos(\Phi + \pi) \tag{4.10}$$

$$I_4 = I_{OB} + I_{RB} + 2\sqrt{I_{OB}I_{RB}}\cos\left(\Phi + \frac{3\pi}{2}\right) \tag{4.11}$$

Where I_{OB} and I_{RB} are intensities at the measured point of object beam and reference beam. The phase Φ is then calculated as [149-150]:

$$\phi = tan^{-1}\left(\frac{I_4 - I_2}{I_1 - I_3}\right) \tag{4.12}$$

In the graph in ***Figure 4.54***(b), the phase noise is proportional to the inverse of the THz signal intensity while relating them together. In fact, it was predicted in the already developed algorithm that the phase noise is linearly proportional to the intensity noise and the inversed modulation amplitude following [149, 151]:

$$\delta_\phi = \sqrt{\frac{2}{R}} \times \frac{\delta_I}{I_m} \tag{4.13}$$

In this equation, R is number of steps used in the phase-stepping measurement and algorithm (which is 4 in this case), δ_I is intensity noise of the system and I_m is the modulation amplitude (or the modulation depth) of the intensity in the interference pattern. Note that the intensity noise of both object beam and reference beam is stable at

the level of 0.264 V.ms and doesn't change with the intensity fluctuation. The modulation amplitude is expressed as in equation (4.14) or can also be calculated from the measured intensities of four phase-steps as in equation (4.15):

$$Imod = 2\sqrt{I_{OB}I_{RB}} \tag{4.14}$$

Or

$$Imod = \sqrt{(I_4 - I_2)^2 + (I_1 - I_3)^2} \tag{4.15}$$

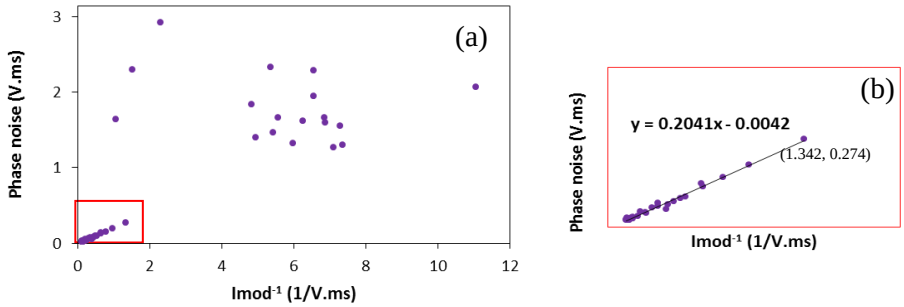

Figure 4.55. Phase noise versus Imod^{-1} (a), and the zoom-in of the indicated red zone in graph (a) with linear fitting line and equation (b).

In ***Figure 4.55***, the phase noise is plotted versus inversed *Imod* (*Imod*$^{-1}$). The result shows that at high modulation amplitude (low *Imod*$^{-1}$), this relationship is linear and the fitting equation is displayed in the graph (b) which is a zoom-in of the red zone indicated in the graph (a). In the linear fitting equation, the second parameter is too small that can be neglected (0.0042). The first parameter shows an agreement within 8.3% between the expected value (0.187) of the constant in equation (4.13) when the intensity noise is included. This result shows that high-fidelity data are obtained from the measuring system.

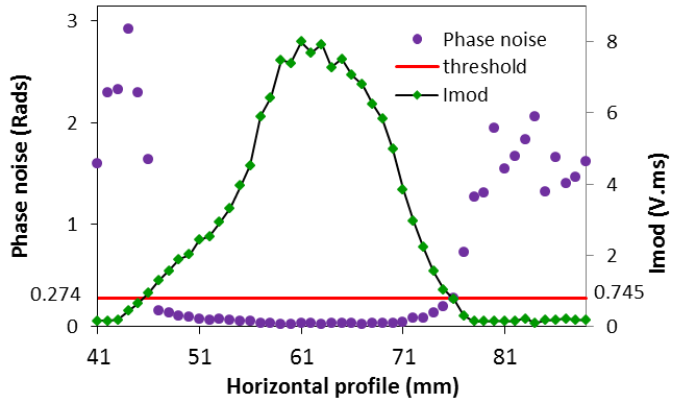

Figure 4.56. Threshold for phase noise with the corresponding modulation amplitude level.

Although in the graph (b) of ***Figure 4.55***, the last point which is considered to have a "high modulation amplitude" to be included in the linear fitting has a phase noise as high as 0.274 rads and a modulation amplitude of 1/1.342 V.ms. This modulation amplitude equals to 10% of the maximum modulation amplitude (~8 V.ms, see ***Figure 4.52***), which removed ~30% of the data pixels in this measurement. The phase noise threshold is equivalent to $2\pi/23$ fraction of an interference fringe. However at the centre of the beam where the intensities reaches maximum, the phase noises are as low as 0.025 rads, which corresponds to $2\pi/251$. This phase noise is relatively low level and is compared to typical phase noise of $2\pi/250$ of a system using CCD or CMOS camera working at visible wavelengths [152]. Thus ***Figure 4.56*** shows in graph a threshold level for phase noise in primary vertical axis with the corresponding modulation amplitude in the secondary vertical axis. Therefore in all the later phase measurements, the smallest 10% of modulation amplitude will not be processed. This can be done by defining a threshold of 10% of *Imod* as "Not a Number" (NaN) while analysing data using Matlab.

4.9.3. 2D Phase Noise

An entire set of two-dimensional (2D) phase measurements over a long period has been collected and analysed. The aim of the work is to build up a 2D phase noise map for the whole interference pattern during 12 hours, which duration is needed to finish a digital holography measurement. Based on the approach presented in the previous section, the phase was calculated by equation (4.12), from the measured intensities of the four phase lags. The phase-stepping was made mechanically by moving the Z stage which carries the RM.

Data on the changing of the phase in 2D across the interference pattern over time were collected every 40 minutes; image size is of 50x35 pixels with pixel size 1 mm. Every image is included with 10% of modulation amplitude threshold not to be processed as discussed above. ***Table 4.2*** summarizes time 'time budget' for individual processes. Time consuming for one pixel measurement is 0.5 second. For one 4-phase-step measurement, the number of pixels to be measured is 7000 points and the total time to finish one measurement is 3500 seconds (~ 1 hour).

1 pixel (s)		2D phase	
DAQ	0.125	**Image size**	50 x 35
Stage Moving	0.183	**Phase-step**	4
Waiting time	0.192	**Number of pixels**	7000
Total time	0.5	**Total time (s)**	3500

Table 4.2. Time budget of individual process in the sampling period of one pixel and one 2D phase measurement.

The 2D phase noise map was built by calculating the phase noise as a STD of the measured phase over time for each pixel in the image. This phase noise map is presented in ***Figure 4.57*** with a scaled colour bar in the right, unit in radians. From the map we can see that excluding 10% of modulation amplitude give a maximum phase noise (threshold) level is still kept at ~0.25 rads. In the middle of the beam where the modulation amplitude is high, the phase is more stable which the noise level can be as low as 0.01- 0.02 rads ($2\pi/628$ - $2\pi/314$), which is the same level as calculated in the 1D phase noise investigation (Section 4.9.2.), but over extended time need for recording DHIs.

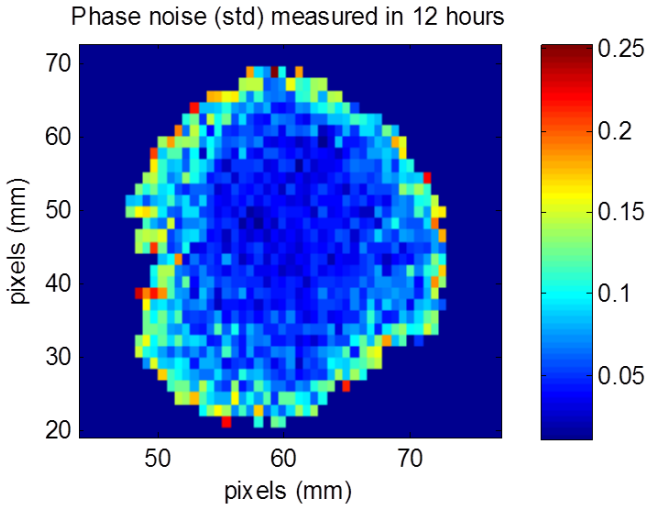

Figure 4.57. 2D phase noise map. Unit in rads.

The map gives a calibration for phase noise across the interference pattern during a long period of time. This long term phase stability during this study is needed for later measurements in the application of the THz phase-shifting holography.

4.9.4. Thickness Measurement

In this experiment, changes in the thickness of a wedge object are measured with the Mach-Zehnder interferometer, described above. Test object is a Tetra-polyethylene (Teflon) block in the shape of a wedge as shown in ***Figure 4.58***. The object is opaque in visible wavelength but is transmitted in THz range. This is a typical sample material, which is transmitted through in THz region.

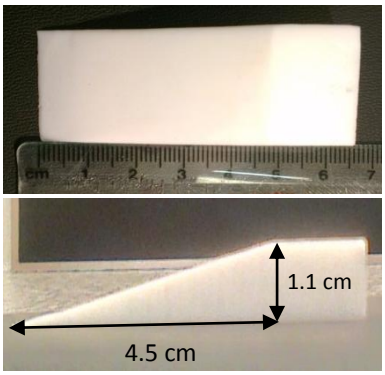

Figure 4.58. Shape and size of Teflon wedge object used for phase resolution and thickness measurement.

To measure the thickness, the principle is well-known and simple: The phases of the object and of the measuring environment (the air) are measured as above (equations 4.8 – 4.12), and the unknown thickness is calculated from the phase difference between them equation (3.7) with the refractive index of Teflon is 1.46 in THz range which is well-known. So Δn is 0.46 in this case.

The step by step description for the measurement and the calculation of phase difference is shown in figure 4.30. First of all, the phase of the air reference is measured with 4 phase-steps 0, $\pi/2$, π, and $3\pi/2$ (***Figure 4.59***(a)). Second, the wedge object was put in the object arm of the interferometer so that the object beam was transmitted through the area on the object which we want to measure. The measurement of 4 phase-steps was repeated and we get 4 interferograms which hold the object's phase information (***Figure 4.59***(b)). Here, the recorded interferograms are of size 41x36 pixels, with a pixel size of 1 mm. Third, the phases of air reference and of the wedge object are retrieved as per the equation 4.11. Images of these phases are shown in ***Figure 4.59***(c) and (d) respectively. The phase difference is calculated by subtracting these two phases together and is shown in figure 4.30(e). Phase images are with 10% modulation

amplitude threshold, and the black to white colour corresponds to –π to π. ***Figure 4.59***(f) shows cross sections of the phase of air reference and of the wedge together in one graph. The red lines cross the horizontal profile of the figure (c) and (d) is to indicate which cross section was taken to show.

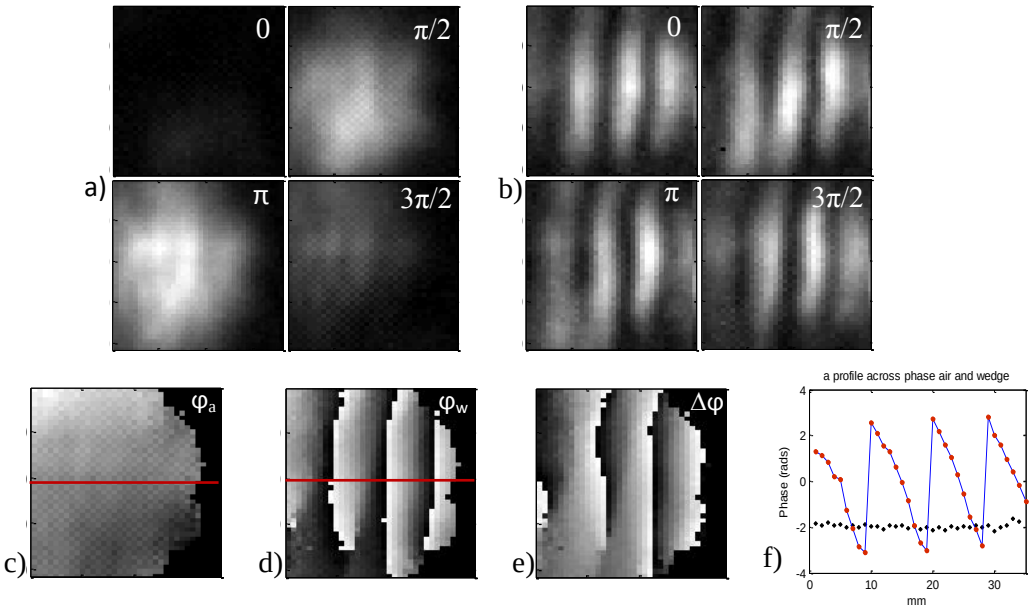

Figure 4.59. Four recorded interferograms of successive reference's phase-steps of air reference (a), and of the wedge (b). Calculated phase from the four recorded interferogram of air (c), and of wedge (d). Phase difference of wedge and air (e), and a cross section of air and wedge.

The interference phase is ambiguous (wrapped) to an additive of 2π period, as can be seen clearly in ***Figure 4.59***(f). This is due to the limitation of using wavelength as a unit of length measurement. The procedure to convert this wrapped phase to continuous phase is called "unwrapping". There are some algorithms in the literature to calculate the unwrapping of the phase. In this thesis work, the Goldstein's branch cut method [153] is used. The algorithm and software development can also be found described in [154].

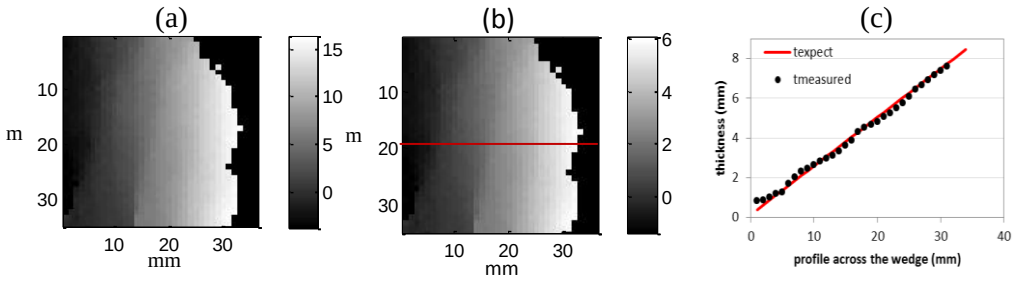

Figure 4.60. Unwrapped phase (a), measured thickness (b), and thickness profile compares with expected values calculated from the real shape of the wedge. (c).

Figure 4.60 shows the unwrapped phase (a) and the calculated thickness (b) in which some lower noisy pixels were removed (compared to the full size images in ***Figure 4.59***). An example of the measured thickness compared to the expected values calculated from the real shape of the wedge is displayed in figure (c). The rms error between the measured and expected values is of 0.11 mm. The phase noise contributes the most to this error. When the threshold of the modulation amplitude is set at 10% of the maximum value of modulation amplitude, we expect the maximum phase noise of ~ 0.27 rads (equivalent to $2\pi/23$), which corresponds to 0.09 mm in the thickness noise measurement of Teflon (equivalent $\lambda/13$). Compare with previous study [120], a lower noise level was achieved because the source used in the study was a FIRL with much higher power and a shorter wavelength (2.52 THz/ 0.119 mm). In addition, the application of 10% modulation amplitude threshold was of the air reference, whereas the 10% I_{mod} when there is an object should be at a higher threshold as the light intensity is smaller after it is transmitted through the object. This may be one of the reasons for the different error number that we get here. Also, we see that the object beam after the wedge has shifted a distance from the perpendicular direction. However when it is shifted, it is shifted for the whole wedge, so the inclined angle doesn't change in the measured values. And we do not see any signal of the perpendicular transmitted beam nor of the reflection beam, so it can be ignored. The ripple noise comes from detector non-linearity.

4.10. CONCLUSION

In conclusion, a THz multiplier source has been characterised together with a pyroelectric detector in our lab. The detector which has a rise time of 125 ms was used to detect the signal of 4 Hz 0.5 duty cycles. The source has a beam waist diameter of

~1.8 and ~1.9 mm in lateral directions. These diameters determine the smallest achievable resolutions of an imaging system which uses the source, including the DHI. Random noise of the source- detector combination is of 0.002 mV and the SNR is of ~ 40 - 50 dB which can compare to the SNR levels in the literature. Some initial applications have been studied with the new source and detector, including spectroscopy (in transmission measurements) and in imaging applications.

The same Mach-Zehnder interferometer setup which will be used in Chapter 5 for THz digital holographic interferometry was studied in this Chapter. Results about interferometry measurements show that the phase noise is proportional to the inversed modulation amplitude of the interference fringes, whereas the intensity noise isn't. The linear parameters of the dependence of the phase noise to the inversed modulation amplitude are matched within 8.3% difference with the calculated theory. From those results, a threshold of 10% of the modulation amplitude was determined where the pixels with intensities lower than that will be removed from the later calculations. At the threshold of 10% of the I_{mod}, the phase noise reaches $2\pi/23$ maximum. However at the centre of the beam where the I_{mod} is high, the phase noise is as low as $2\pi/251$, which is very precise (and also accurate).

Studies on temporal stability of the system in a long period of 12 hours were taken in 2D because the recording of THz DHI takes several hours to finish one measurement. Observations have shown that the phase noise kept stable during the measured period. When the bad pixels with intensities smaller than 10% of I_{mod} removed, the maximum phase noise reaches 0.25 rads (equivalent to $2\pi/25$) and the minimum phase noise can be as low as 0.1 – 0.2 rads (equivalent to $2\pi/628$ - $2\pi/314$) in the middle of the beam. These phase noise levels are the same as in the previous studies in 1D and in a shorter period mentioned above. In conclusion, the studies on the THz multiplier source and the pyroelectric detector used in interferometry have shown that the system is table in long term period, suitable for the recording of holograms in DHI applications with single point detector scanning.

Chapter 5

THz PHASE-SHIFTING DIGITAL HOLOGRAPHIC INTERFEROMETRY

5.1. INTRODUCTION

In recent years, research on optical digital holography has been developed to a great degree thanks to the advances in high resolution cameras and image processing techniques [155-156]. Digital holography (DH) has many advantages over conventional holography, including the ability to record and to reconstruct information digitally in which applying spectral filter, refocusing the area under investigation by numerical methods can be performed without the need of any change in the measuring system. The phase-shifting interferometry technique applied to DH enables a higher image quality reconstruction and a wider viewing angle than from traditional DH off axis configuration [135], thanks to ability to extract exactly the desired (real) image from the known measured phase. Optical digital holography has been wildly used in many applications such as in metrology [157-158], in measuring shape and surface deformation of opaque bodies [159-160], in vibration analysis [161-162], in biological microscopy [163-165].

The THz radiation has many advantages over other radiations in electro-magnetic spectrum. However, very little publications can be found in the literature that addresses the issue of digital holography in THz field (Chapter 2: literature review). In this chapter, we explore the possibility of applying phase-shifting DHI in THz region. The setup used the THz-multiplier source coupled with the pyroelectric detector which is relatively low cost, effective and easy-to-use equipment. The holograms were recorded in four phase-steps and the reconstructions were made using convolution approach in order to track the area under investigation inside the object volume. Reconstruction images are free from disturbing orders makes it easier for alignment as well as time

consumed computing reconstruction. Applications range from non-destructive testing of internal defaults inside transparent objects or in metrology measurements. The rChapter is organized as follows: Section 5.2 presents optical DHI experiments and results which were performed successfully in our lab. From what had been done, the techniques were applied to THz DHI. Section 5.3 presents the characterization of the system and the applications are described and discussed. The conclusion is reported in Section 5.4.

5.2. OPTICAL DIGITAL HOLOGRAPHIC INTERFEROMETRY

Practical work with optical digital holography was undertaken in order to study the achievable resolution and the noise behaviour for the application of THz DHI later on. Optical holography experiments used a 2D CCD camera to record holograms which speeded up the investigation process compared to the THz DHI which scanned a single point detector. This section will describe what has been done successfully about optical DHI.

5.2.1. Experimental setup

Figure 5.61 depicts the experimental setup for the recording of holograms which was a Michelson interferometer configuration. The light source was a HeNe laser which emitted a red light at 633 nm. The output laser beam was filtered by passing through an optical fiber. The beam after the fiber was Gaussian and divergent. L was a 30 cm focal length plano-convex lens which was used to collimate the divergence beam from the fiber. Mirror M redirected the collimated beam to the 50% beam-splitter BS which separated the original beam to two equivalent object and reference beams. The object was recorded in reflection. The wedge was used substitution to a mirror in the reference beam to equalize reference beam intensity with reflected object beam intensity. By having the similar intensity of the two beams, a better contrast (visibility) of the fringes was achieved, and so a better image quality and better phase resolution. The wedge was mounted on a piezoelectric translation stage which was moved by applying a suitable DC voltage for phase stepping application.

The recording camera was a charge coupled device (CCD) of 768 x 1024 pixels, pixel pitch of 4.69 μm in both directions. With this sampling pitch, the corresponding maximum resolvable spatial frequency f_{signal} of the CCD is 106 line-pairs per mm (lp mm^{-1}). This resolution limits the maximum off-axis angle θ between object and reference beams, which resulting maximum inter-fringe frequency in the hologram.

When the object and the reference beams were combined together at the CCD plane, the created interference fringes were separated at a distance which can be calculated similarly as in the case of Young's fringes, following:

$$i = \frac{\lambda}{2\sin\left(\frac{\theta}{2}\right)} \tag{5.1}$$

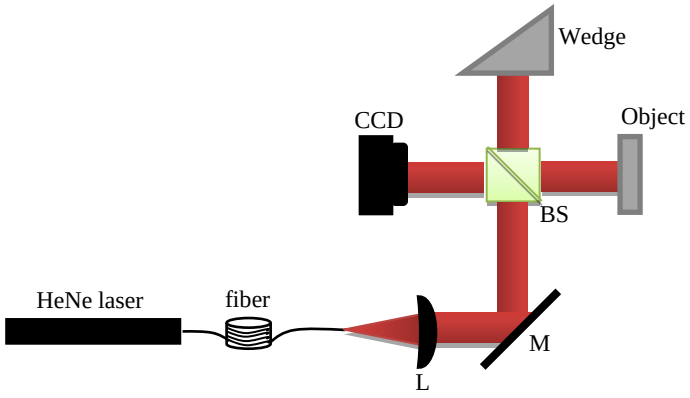

Figure 5.61. Optical system for recording reflection hologram. M1, M2, M3 are flat mirrors, BS is a beam splitter.

The inter-fringe frequency f_{signal} is then calculated as the inverse of fringe-distance, which is $2\frac{\sin\left(\frac{\theta}{2}\right)}{\lambda}$. This inter-fringe frequency is the signal frequency which is being studied/ measured. According to the well-known Shannon theorem [166], the sampling frequency needs to be at least twice bigger than the signal frequency. In case the sine is small, the maximum angle between two beams can be approximated by:

$$\theta_{max} \approx \lambda f_{sample} \tag{5.2}$$

which is 3.85 degrees in this case. The CCD-object distance is 19 cm which was measured manually. With this configuration, it is possible to simply use the Fresnel transformation for the reconstruction (Chapter 2: literature review).

5.2.2. Phase-shifting in DH

Figure 5.62 shows typical recorded holograms at two different recording distances (camera - object distance) of 19 cm and 41 cm. The small images at lower-right corner of each hologram are zooming-in of a small zone in that right corner of each hologram to make visible the speckles and the interference fringes. The speckle size is bigger in the hologram recorded at 41 cm distance than that in the hologram recorded at 19 cm distance. This fact can be recognised directly by naked eyes and it is in agreement with

subjective speckle theory when the speckle size is proportional to the object-CCD distance.

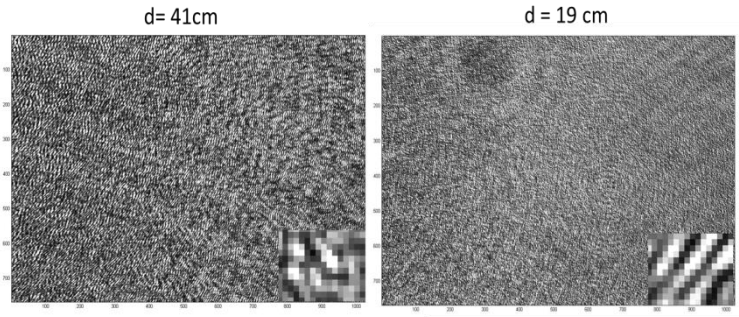

Figure 5.62. Typical recorded holograms at two difference recording distance.

Resolution of the images reconstructed from holograms by Fresnel algorithm depends on the reconstruction distance. At the image plane, the resolution is proportional to the recording distance and inversely proportional to the pixel pitch of the detector (equation (2.17) - Chapter 2). Therefore, expected lateral resolutions in the reconstructed image (at the object plane) by Fresnel algorithm would be 25.0 μm and 33.4 μm in x and y directions for the hologram recorded at 19 cm, or be 54.0 μm and 72.0 μm for the hologram recorded at 41 cm distance. These resolution sizes are actually the diffraction limit (or Airy disk/ speckle diameter) of optical system in which the hologram is an aperture (Chapter 2). This speckle size is ~ 7 - 10 times pixel size of the detector (4.69 μm). Thus it gives an idea for the setting up of the THz system that the recording distance (object-detector distance) need to be reduced as much as possible in order to gain resolution for the reconstructed image.

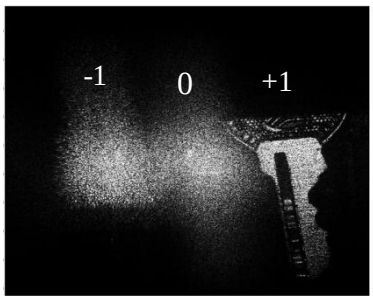

Figure 5.63. Fresnel reconstruction of the hologram recorded at 19 cm in figure 5.2.Zero order is reduced by subtracting the hologram to the mean of it.

Figure 5.63 is reconstructed image of the hologram recorded at 19 cm in figure 5.2. The hologram was recorded at an off axis angle between object and reference

beams in order to separate spatially the different images and the DC term [126]. The reconstruction shows the real image (+1) and its conjugate (-1) as well as the disturbed on-axis DC term (0) which are separated at different positions in the reconstructed image. Although the DC term was then reduced by subtracting the hologram to the mean of it, but it cannot be eliminated and is still visible.

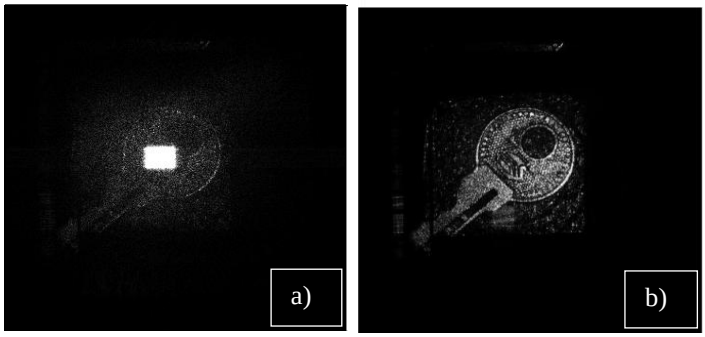

Figure 5.64. Reconstructed images of (a) an off-axis hologram (with reduced/filtered zero order) and (b) from four phase-shifting holograms.

The phase-stepping technique used in this work has advantages over off-axis hologram as already mentioned in Chapter 2. First of all it extracts the desired order (+1) and removes automatically the others (0 and -1 orders), as seen in ***Figure 5.64***(b). In this figure, the hologram recorded at 41 cm in ***Figure 5.62*** is reconstructed, showing a bright on-axis DC term disturbs the real image (a), whereas the reconstruction from 4 consecutive phase-lag holograms shows only +1 order (b). Consequently, it overcomes the limitation of minimum off-axis angle to separate the image orders. Obviously, the viewing angle is wider compared to the off-axis technique. This technique was studied in order to apply at THz wavelength for the first time (described in the next section).

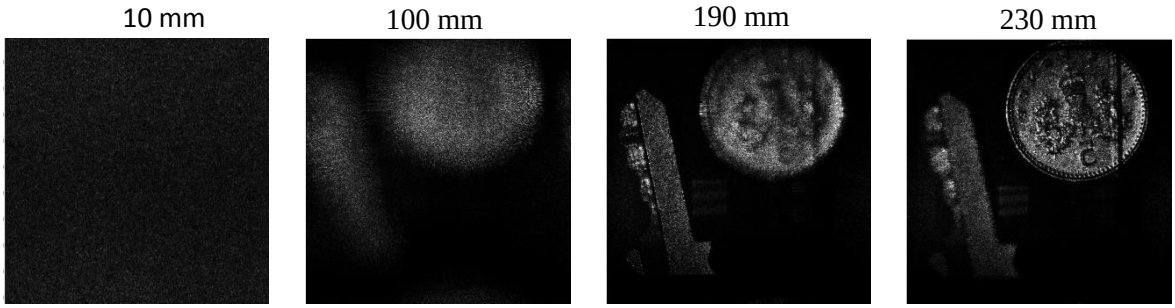

Figure 5.65. Hologram reconstruction at different depth: 10 mm, 100 mm, 190 mm and 230 mm distance.

Figure 5.65 is a test to verify the depth resolution and the ability of digitally focusing of DH. Two objects (a key and a coin) placed at different distance from the CCD were captured together in one hologram. The reconstruction at different distances was manipulated to find correct positions of each object. At 190 ± 5 mm the key is in focus whereas at 230 ± 5 mm it is out of focus but the coin is in focus instead. The distances are matched with what had been measured manually. The line at the right corner of the coin is the image of the edge of the beam splitter.

5.2.3. Deformation measurement

In this subsection, DHI was applied successfully in deformation measurement. The experiment was the same setup as described in section 5.2.1. Holograms were recorded for 4-phase-steps of one object (a British coin) at two different states. The object was tilted a small angle between the two states, called state 1 and state 2. The reconstruction by Fresnel transformation results to complex amplitudes which contains information of the object waves at each state. The intensities and phases are calculated from the reconstructed wavefields, as written in Chapter 2. The object phases are calculated as:

$$\Phi_1 = arctan \frac{Im\ O_1(\xi,\eta)}{Re\ O_1(\xi,\eta)} \tag{5.3}$$

$$\Phi_2 = arctan \frac{Im\ O_2(\xi,\eta)}{Re\ O_2(\xi,\eta)} \tag{5.4}$$

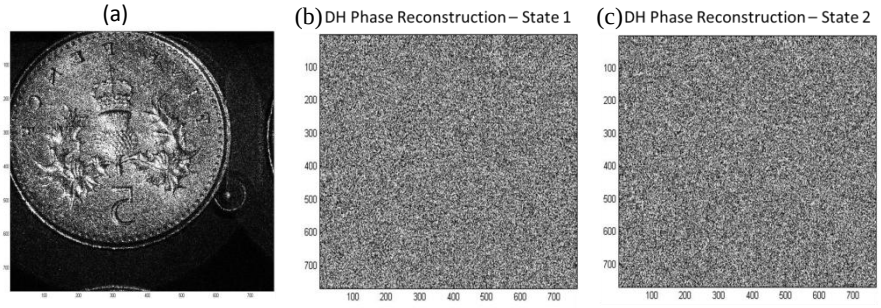

Figure 5.66. Reconstructed intensity of the object (a) and reconstructed phases (of the object) in two different states (b,c).

Figure 5.66 shows the reconstructed intensity and phases of two states of the object when it is reconstructed at the object plane. The object in state 2 was tilted a small angle compare to that in state 1. In this case, the phase is what we are interested in. Phases vary randomly from $-\pi$ to π due to the roughness on the surface of the object. The interference phase is now calculated by subtraction of the two phases:

$$\Delta\Phi = \Phi_1 - \Phi_2 \tag{5.5}$$

The calculated phase difference varies from -2π to 2π as a result of the subtraction. This phase difference can be "re-wrapped" so that it ranges from –π to π, using the equation:

$$\Delta\Phi = \arctan(\sin(\Delta\Phi), \cos(\Delta\Phi)) \tag{5.6}$$

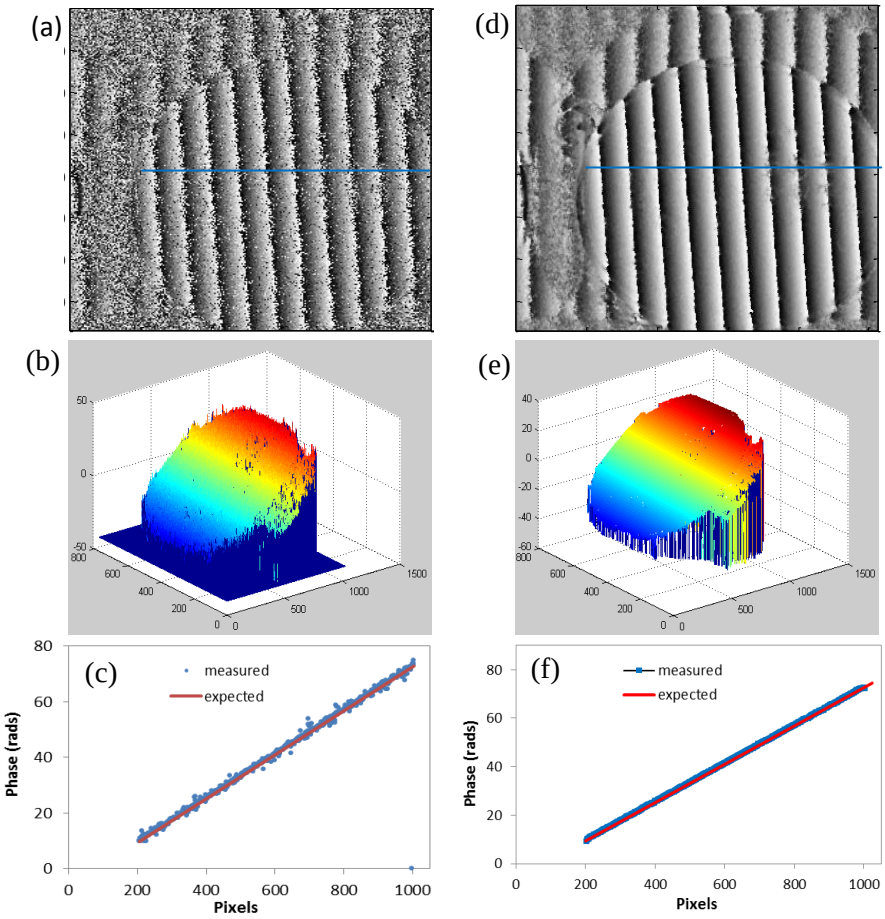

Figure 5.67. Phase difference (a), unwrapped phase in 3D (b), and comparison between measured and expected phase (c); those phases after smoothed by 7x7 median windows (d, e, f).

The resulting phase difference is presented in ***Figure 5.67***(a). This phase was then unwrapped using Goldstein's branch cut method as mentioned in Chapter 4. The unwrapped phase is shown in 3D in ***Figure 5.67***(b). The reconstructed phase is very noisy due to bad pixel points as can be seen, which may be caused mostly by speckle decorrelation. In this setup, the object was placed at 15 cm from the detector, so the speckles in the reconstructed image have an average size of 20 – 26 μm in two directions, which correspond to 5 or 6 times of the pixel size.

In order to determine the precision and accuracy of the measurement, the measured phase is compared to the calculated (expected) phase which corresponds to the real tilted angle between the two states. The pixels taken for comparing are in the blue line in the middle of the horizontal axis (at pixel 334) as indicated in ***Figure 5.67***(a). The differences between the measured and expected phases are taken at every pixel and the rms noise (SD) is extracted from those different values. The result is shown in ***Figure 5.67***(c). The measured rms noise (SD) is 0.733 rads, which corresponds to 1/9 of a wavelength. It shows how variable a measured value can be from the expected value (real tilted angle of the object) and not from the mean value of the measurements. In this case, it presents both the precision and accuracy of the measurement. According to normal distribution theory, any measured number could be 70% possibility fallen in the range of ± 0.733 from the normal value (real tilted object angle in this case). Contribution to the observed phase noise may include speckle decorrelation, noise sensitivity of the phase algorithm, electronic and quantization noise [167]. Errors caused by the phase algorithm and the CCD camera sensitivity contribute to maximum 0.03 rads [167-169], the rest comes from speckle decorrelation which accounting for ~ 95% of the phase noise observed.

To improve the results, a median filter was implemented using a routine written in Matlab. In addition, bad pixels with intensities smaller than 10% of the maximum modulation amplitude are removed. The median filter performs the filtering noise using a median window which is scanned around the image. Each output pixel is the median value in the window of neighbourhood pixels around the corresponding pixel in the original input image. The advantage of using median window in this case is that it filters out bad data points but it does not change the phase value of pixel points [169], whereas the average filter doesn't work that way. ***Figure 5.67(d,e)*** presents the phase difference and the unwrapped phase after being smoothed using 7x7 median window. Quantitatively, ***Figure 5.67(f)*** makes a comparison between the measured phases after filtered to the same expected phases as already mentioned above in the graph in ***Figure 5.67(c)***. The rms phase error calculated in this case is 0.115 rad, which corresponds to $2\pi/55$. In this case, the noise has been reduced by more than 5 times by digital signal processing. The quantity of deformation can then be calculated from the measured phase using equation (2.25) written in Chapter 2.

In conclusion, when phase-shifting technique is applied to deformation measurement using DHI, the speckle noise contributes the most to the phase error due to

the random property of the speckle. The main contributors accounting to this error includes speckle decorrelation and low modulation amplitude of the pixel points. Speckle decorrelation is caused when the collecting angle is changed between two states. When the THz radiation is used, the long wavelengths cause a bigger speckle size but at the same time the pixel size is much bigger. Low modulation intensity is a fundamental problem of phase-shifting technique which can be reduced by applying the 10% intensity threshold. In the case of THz radiation, the intensities are low due to the nature of THz low energy photons and of the source. So similarly as in this study, some signal processing and data analysis may have to apply in THz measurements in order to improve the results when working with THz DHI.

5.3. TERAHERTZ DIGITAL HOLOGRAPHIC INTERFEROMETRY

In this Section, phase-stepped DHI to remove DC term has been implemented for the first time in THz region with full reconstruction will be presented. The Section starts with the description of the experimental setup, and continues with the investigation of the resolutions of the system. Finally to validate the method, deformation (thickness) measurement and NDT of the internal defects are performed.

5.3.1. Experiment for recording and the reconstruction

A Mach-Zehnder interferometer was built to record the holograms in transmission mode. The experimental setup of the system is depicted in ***Figure 5.68***. THz radiation emitted from the multiplier source was collimated by a Teflon plano-convex lens. The operation frequency was chosen at 0.375 THz (0.8 mm wavelength). BS1 is a 50% HRFZ silicon (high resistivity float zone silicon) beam splitter which separated the collimated THz beam into object beam and reference beam. Reference mirror (RM) and object mirror (OM) redirected the corresponding beams and made an angle of 45^{o} with the incident beam. BS2 is a second and identical beam splitter as BS1 that combined the reference and object beams together. The holograms were recorded by scanning the 1-D pyroelectric detector in the 2D translation stage system. Phase-shifts were performed by displacing the reference mirror using the third translation stage. The holograms were recorded for 80x80 pixels with pixel size is 0.5 mm. It covers a region of 40x40 mm^2 in which the whole interference beam is recorded. According to the characterization of the THz source which had been done previously in chapter 4, the minimum resolution an

imaging system can get with the source is around 2 mm (based on the measured beam waist diameters). Shannon criteria said that the detector pixel needs to be smaller than 1 mm so that information isn't lost. The 0.5 mm pixel pitch was chosen to be smaller than this minimum required step size to have a smoother image.

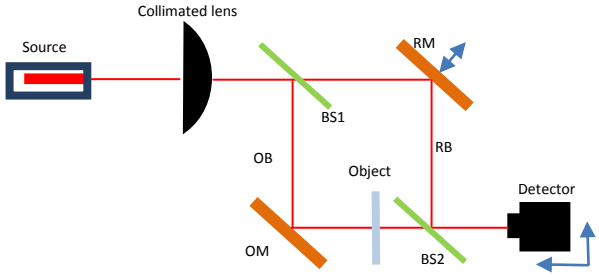

Figure 5.68. Schemas for the experimental setup.

In DHI, the argument for pixel size is also based on the ability to resolve the speckle spots and the inter-fringe in the recorded holograms. In this experimental setup, the object-detector distance was d ≈ 60 mm, subjective speckle would have an average size of 1.2 mm (= λd / MΔx). The pixel pitch of 0.5 mm size equals to 1/2.4 speckle size, which can surely resolve the speckles. With 0.5 mm pixel pitch, the maximum resolvable spatial frequency is 1 lp/mm. From equation (5.2), the maximum angle that can be tilted between OB and RB is:

$$\theta_{max} \leq 2sin^{-1}\left(\frac{\lambda}{4\Delta x}\right) \tag{5.8}$$

Where λ = 0.8 mm; Δx = 0.5 mm; gives calculated maximum angle of ~ $47^{o,}$ which is very big. By introducing phase-stepped for the first time in this experiment at THz frequency, the problem with minimum off-axis angle is overcome. Instead, this angle can be as small as 0 degree.

The reconstruction was made by convolution approach. In this case, the pixel size of the reconstructed image is equal to that of the recorded hologram at every reconstructed distance (Chapter 2), which is different from the Fresnel transformation approach. As the scale of the reconstructed images doesn't change for any reconstructed distance, the advantage of the convolution approach is to localize the internal defects within the object volume. This characteristic is very suitable for in-line transmission holographic applications.

5.3.2. Resolution target

A bespoke resolution target was created in order to study experimentally lateral resolutions of the measuring system described above. The target was fabricated on a thin aluminium plate which includes 4 sets of resolutions; each of them has 4 square holes of the same size and the holes are separated at the same distance equals to the diameters of the holes, as depicted in ***Figure 5.69***. The 4 sets of resolutions are separated at a distance of 5mm from each other. This structure of holes was entirely illuminated by the object beam and was combined with the reference beam by the second beam-splitter.

An estimated resolution based on the diffraction limit and Rayleigh's criterion can be calculated as:

$$R = 1.22\frac{\lambda d}{D} \tag{5.9}$$

In which $\lambda = 0.8$ mm; $D = 40$ mm is hologram size; and $d = 68$ mm is reconstruction distance. Hence the resolution is calculated as 1.66 mm. Remind that the characterization of the THz source in Chapter 4 comes to a conclusion that the resolution of any imaging system which uses the source is ≥ 1.8-1.9 mm (based on the measured beam waist diameters). This resolution is bigger than the diffraction limited of the system. So we may expect that the spatial resolution should be around 1.8 mm.

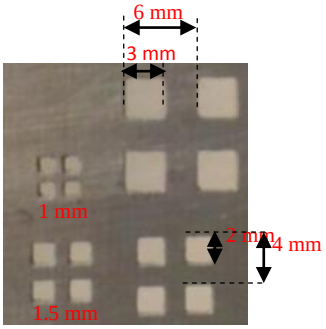

Figure 5.69. Resolution target made with aluminium plate

Holograms are recorded at 4 successive phase-steps of 0, π/2, π, and 3π/2 radians. ***Figure 5.70*** (a-d) illustrates the reconstructions from the recorded holograms of the resolution target (at 0.375 THz). ***Figure 5.70***(a-c) shows the intensity reconstruction at different distance of the object. By varying the reconstructed distance z in the equation (2.21) (Chapter 2), the object plane is determined at z = 68 mm which is matched with the object-detector distance measured manually in the experimental setup. In the

reconstruction image, the 4 sets of holes are well separated from each other because the distance between them (5 mm) is bigger than the limited resolution of ~ 1.8 mm.

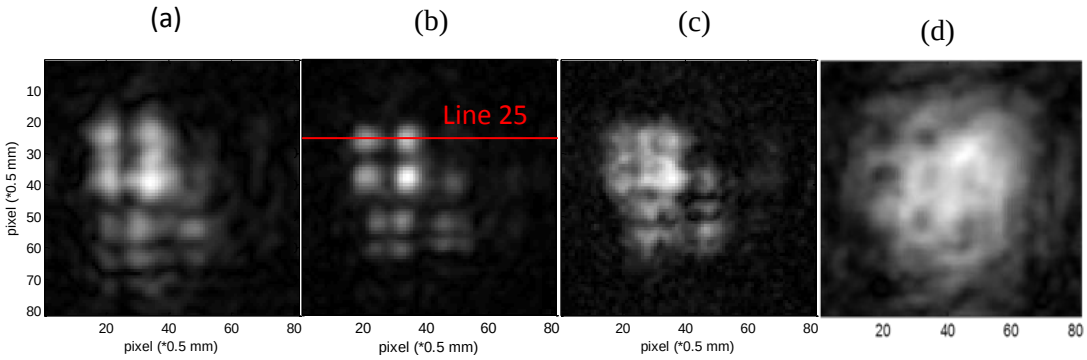

Figure 5.70. Reconstruction images of resolution target at different reconstructed distances: at 85 cm (a), at 68 cm (b) and at 45 cm (c); (d) is reconstructed image at 68 cm distance by one single hologram.

In the resolution target, the sets of 2 mm and of 3 mm holes satisfy the limited resolution calculated above. In the reconstruction image (***Figure 5.70***(b)), they are well resolved. However, the hole in the low-right corner of 3 mm resolution set is brighter than the others. The reason can be understandable: it was at the centre of the Gaussian interference beam so the intensity is stronger. The set of 1.5 mm holes are right below the expected resolution, it is hard to resolve the holes. ***Figure 5.70***(d) is the reconstructed image of from one single hologram at focus plane of 68 cm distance. The twin image is superimposed with the DC item make it impossible to resolve any resolution set of the target.

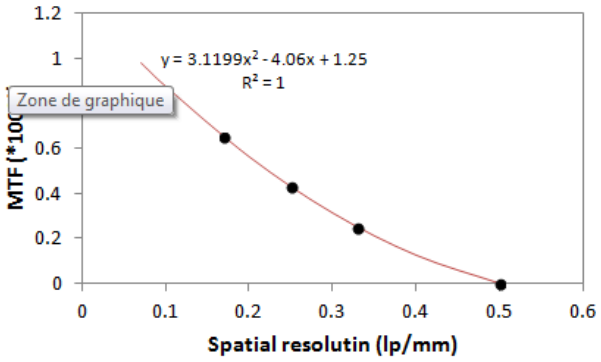

Figure 5.71. Measured MTF values (black dot), and second order polynomial fitting to the measured data (red line) with displayed equation and least square correlation coefficient.

The MTFs for each set of holes are calculated for the reconstructed image at focus plane of 68 mm distance. ***Figure 5.71*** plots these MTF values versus the spatial resolution (black dots). A second order polynomial fitting was applied to the measured data (red line). According to the fitting, low MTF (<10%) is recorded at ~ 0.4 lp/mm. This resolution can be considered as the cut-off frequency of the system: objects of size smaller than 0.4 lp/mm is considered to be un-resolvable.

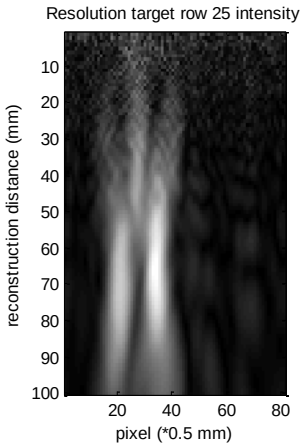

Figure 5.72. Cross section of reconstructed images at pixel 25 of vertical axis while changing reconstruction distance (d).

The depth resolution of the system can be estimated from ***Figure 5.72*** in which a cross section of 3 mm apertures is shown while the reconstructed plane is moved along the propagation direction. ***Figure 5.72*** is the cross section cut at the pixel 25 of vertical axis of the reconstructed images while changing the reconstruction distance. The cross section imaged is the red line indicated in ***Figure 5.70***(b) as "line 25". From the ***Figure 5.72*** we can see that the diffraction spot size of one aperture (e.g. the one on the right) is approximate to 30 mm, so the depth resolution of the system would be ~ 15 mm which again, corresponds to what had been predicted as the beam waist diameter in propagation direction is of 14 mm (equation (4.5), Chapter 4).

5.3.3. Thickness measurement

In this sub-section, the above THz system (***Figure 5.68***) was used to record THz phase-stepping holograms of a wedge shaped object made of Teflon. A caliper gauge was used to measure the dimensions of the wedge and the result shows that its inclined angle is of $\sin^{-1}(11/45)$ as schematically illustrated in ***Figure 5.73***.

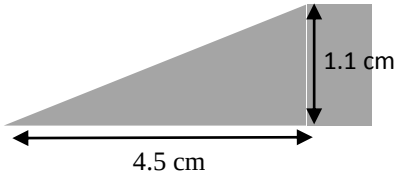

Figure 5.73. Illustration of inclined angle of Teflon wedge object.

Two sets of holograms were recorded in 4 successive phase-steps (0, π/2, π, 3π/2) when there was with and without the object. The holograms have the same size of 81 x 81 pixels, with pixel size is of 0.5 mm. ***Figure 5.74***(*a, b*) shows the recorded holograms (at 0.375 THz) when there was without the object (air reference), and with the object. Holograms of each state (with and without the object) are reconstructed separately using convolution approach at reconstruction distance of 60 mm. From the reconstruction, the object waveforms are obtained.

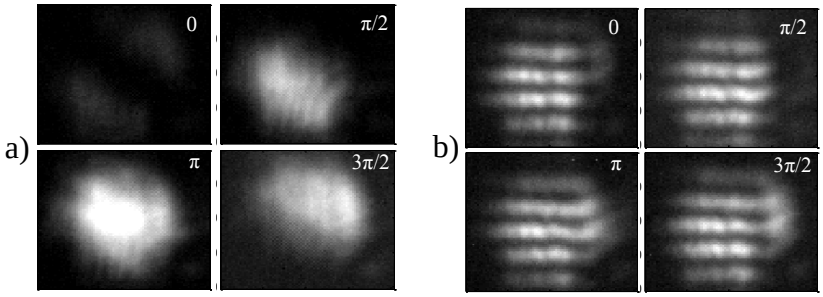

Figure 5.74. Four recorded holograms at four different phase-steps of air reference (a) and of wedge object (b).

Next, the phases of two states are reconstructed using the equation (5.3) and equation (5.4), and are shown in *Figure 5.75*(*a,b*) with the removal of 10% modulation amplitude threshold. The two phases are then combined to make an interference phase (or phase difference) by subtracting them together (*Figure 5.75*(c)). This phase difference contains deformation information between two recorded states, which is the thickness of the wedge. However, as all the interferometric methods which use wavelength as scaled length, the interference phase calculated in this case is ambiguous to a multiple of 2π radians. In order to get continuous phase information, the interference phase is unwrapped as shown in *Figure 5.75*(*d*) for 2D view and *Figure 5.75*(*e*) for 3D view (Delaunay interpolation was used) of the unwrapped phase. The

thickness can then be calculated using equation (2.25) (Chapter 2) in which the refractive index of Teflon is 1.46.

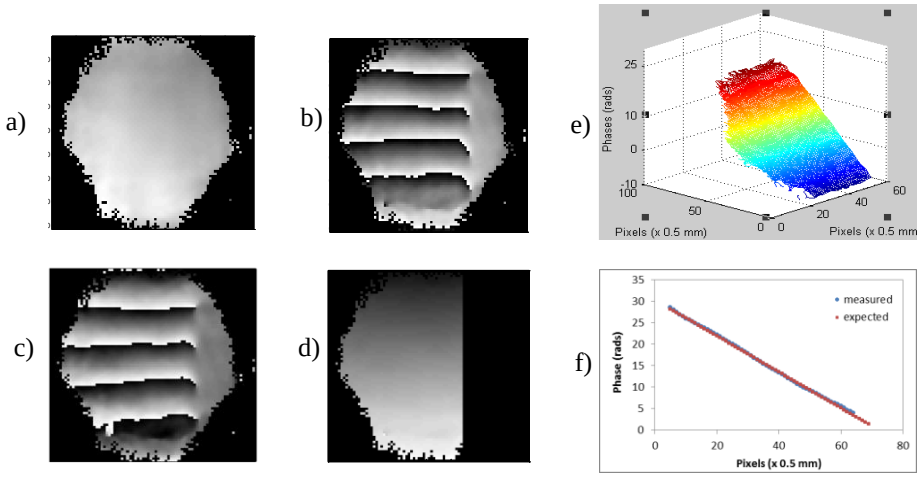

Figure 5.75. Reconstructions with 10% of modulation amplitude removal of phases of air reference (a) and of wedge object (b), phase difference (c), unwrapped phase in 2D (d) and pseudo 3D perspective using Delaunay interpolation (e), comparing a cross-section through centre of the unwrapped phase with the expected values (f).

Figure 5.75(f) comparing the measured phase of a cross-section through the centre of the unwrapped phase with the expected values. The expected values are calculated from the physical shape of the wedge measured by a caliper (which has a resolution of 0.01 mm). The rms phase noise (SD) between the measured and expected phase is 0.175 rad (equivalent to 2π/36) which is the source for thickness measurement uncertainty of 40 μm (λ/20). The cause for this error can be due to several factors and can be resumed in ***Table 5.3***.

Potential error sources		
Detector error	Low I_{mod}	External noise
2%	5% ÷ 95%	~2%

Table 5.3. Contribution of sources of error to the thickness measurement.

Detector error in intensity measurement at each recorded phase-step of holograms is 0.003 V (studied in Chapter 4) which can introduce ~ 0.003 rad in phase noise. Low modulation amplitude introduces noise to the phase measurement as already studied in

Chapter 4 in which the noise level can be as small as 0.01 rad in the middle of the beam, or as big as 0.25 rad near the edge of the beam (after removing 10% of modulation amplitude threshold). Finally, external noise like air turbulence and vibrations can also contribute as one of the error sources to the measurement [168].

5.3.4. NDT of internal defaults

In this section, application of the THz phase-shifting DHI in non-destructive testing of internal default is presented. The object was made of two Teflon blocks, which are 11 mm thick and are combined together at a fixed distance of 10 mm as depicted in ***Figure 5.76***(a). Two designed defaults were round shaped in face side as shown in ***Figure 5.76***(b) (THz beam was transmitted perpendicular to this plane side), with axial length of 11 mm each. The two defaults are called D_1 and D_2 to mark their positions as shown in the figure. Defaults have diameters of 4.6 ± 0.01 mm and 5.0 + 0.01 mm for D1 and D2 respectively, measured by a caliper.

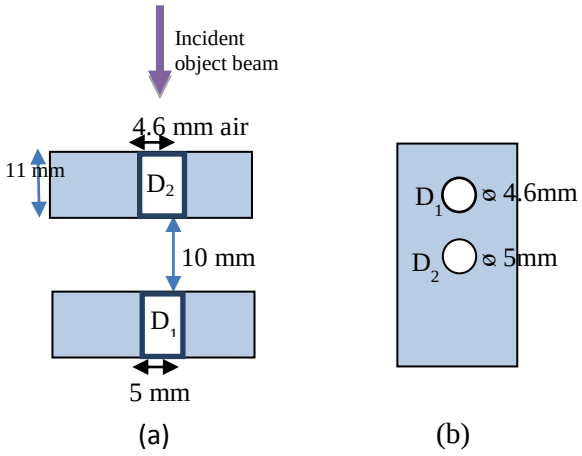

Figure 5.76. Teflon object with air defaults at side view from the top of the object (a) and face view (b).

The object was placed in the object beam of the Mach-Zehnder interferometer (***Figure 5.68***). Four phase-stepping holograms were recorded successively at 0, π/2, π, 3π/2 rads by placing the reference mirror. The recorded holograms are 81x81 pixels in size with pixel size of 0.5 mm.

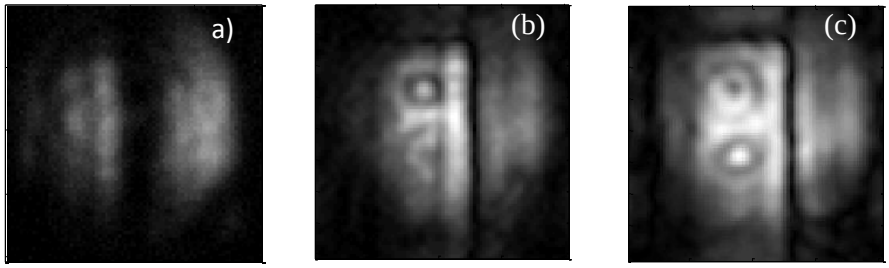

Figure 5.77. A typical recorded hologram of the object without phase-shift (a); reconstructed amplitudes from the recorded phase-stepping holograms at d = 54 cm distance (corresponds to the focusing plane of default D1) (b), and at d = 74 mm distance (corresponds to the focusing plane of default D2) (c).

Figure 5.77(a) shows a typical recorded hologram without phase-shift of the object. The reconstruction process was performed using convolution approach as mentioned above. ***Figure 5.77***(b) and (c) are the reconstructed amplitudes of the object at 54 mm and 74 mm distance, which correspond to the focused distances of default D_1 and default D_2 respectively. These reconstructed distances correspond to the real object-detector distance measured from the experimental setup.

Figure 5.78(a) shows the reconstruction of a cross-section across vertical profile and at the horizontal position x = 35 versus the (digitally scanned) reconstruction distance in the optical axis. This vertical profile crosses the two defaults on the object. The vertical profile reconstructed at 54 mm and 74 mm are noted by the red and blue lines respectively. The red and blue ovals mark the positions of the two defaults in optical axis after the reconstruction. According to the reconstruction in the ***Figure 5.78***(a), these two defaults are separated at a distance of $\Delta d = 20$ mm ± 5 mm in optical direction, which is matched with the real physical shape of the object (***Figure 5.76***). The uncertainty of ± 5 mm is due to the large depth resolution of the system. In addition, the lateral and axial sizes of these defaults can be measured. In ***Figure 5.78***(*b*,*c*), the intensity distribution of the vertical profile reconstructed at 54 and 74 mm distances (the red and blue lines noted in ***Figure 5.78***(a)) are shown. From these graphs, the lateral positions and sizes of the defaults can be tracked. The intensity peaks correspond to the two defaults are located at around 30 and 50 mm in vertical axis y. Those peaks have lateral dimensions of 4.5 ± 0.5 mm and 4.9 ± 0.5 mm for 54 and 74 mm profiles respectively. These sizes are matched with the numbers given by the calliper measurement with an uncertainty of ± 0.5 mm. The noise in the measured size of two

defaults may be due to the low contrast, which comes from the distraction with its neighbouring intensity peaks.

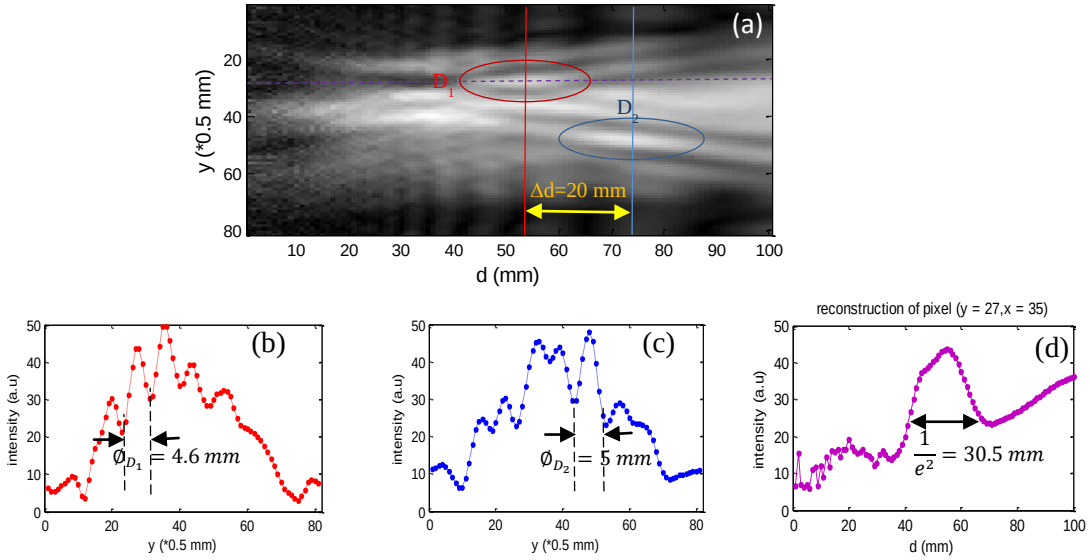

Figure 5.78. Amplitude reconstruction of a cross-section profile along the vertical cut of the object versus the reconstructed distance d (a); reconstructed intensity of the same vertical profile (at pixel x = 35) at 54 mm (b) and 74 mm (c) reconstruction distance; reconstructed intensity of a cross-section profile along the horizontal cut of the object at pixel y = 27, x = 35 (d).

Figure 5.78(d) shows the intensity contribution of the reconstruction of one point at the pixel (x = 27, y = 35) along the axial axis is shown (scanning d distance). This profile (along the axial axis) of the point is also noted in ***Figure 5.77***(d) as a purple dotted line across the default D_1. The graph shows an intensity peak around the position of the focusing plane of D_1. The size of this peak is actually measured Airy disk size of the default D_1 in axial axis. While the real length of D_1 is 10 mm, the measured value is 30.5 ± 0.5 mm. This is understandable as the axial resolution of the system is ~15 mm (Chapter 4 and in Section 5.3.2).

5.5. CONCLUSION

Some potential applications of the phase-shifting DH and DHI have been studied for the first time in the THz region, using a THz-multiplier and the scanning of a one point pyroelectric detector. Applications include phase measurement (for thickness/ deformation measurement) and non-destructive testing of internal defaults of a transparent object. The results show that the reconstruction images of DHI has the axial

resolution of ~1.88 mm and of 15 mm in axial direction. These measured resolutions correspond with the theoretical calculation and with that have been predicted in Chapter 4 (the beam waist size). In the current experiments, recording time for one set of phase-shifting holograms (4 holograms for 4 phase-steps algorithm) is 6 hours.

The advantage of DHI is that not only the amplitude but also the phase can be reconstructed, and also the depth (the object-detector distance) can be determined digitally. One of the current directions for the research in THz field is to develop 2D room temperature operation detector (focal plane array, 2D pyroelectric detector etc…). When the technology is ready and is applied to THz DHI, recording time of holograms could be reduced considerably, and the technique will play an important role in industry metrology and/or non-destructive testing and evaluation. For example, any object that is transparent to THz beam of a narrowband source could be imaged and reconstructed with a sub-wavelength axial resolution. Much information can be extracted from the reconstructed images such as stress-induced birefringence or vibration of the objects as the recording time will be short [30].

Chapter 6

CONCLUSION

The purpose of the research was to explore the potential applications of newly available THz technologies, including THz sources and detectors. Hence a comprehensive understanding of the state-of-the art and future direction in the field is needed. From the course of the literature review, THz-TDS has been widely used in most research works and applications in the THz domain. Among the other potential applicable THz sources, an all-optical THz intra-cavity OPO laser was chosen for performing initial research on metrology in order to access future full-field application. It has advantage properties which are suitable for interferometry application and it was new on the commercial market. For the first time, an all-optical THz source was used in thickness measurement using multi-wavelength interferometry technique to overcome the conventional 2π ambiguity in the depth measurements. The source has also been implemented in spectroscopy to investigate the transmission properties of some materials of our future interest. The results showed that 0.65 mm thick alumina ceramic specimen has a transmission of 20-40% in a window in the frequency tuneable range of the laser, which was 1.2 – 1.65 THz. With other specimens, the results weren't positive. Though the laser was demonstrated to be able to apply in the interferometric measurements, the limited technology at the time of the tests limited the chosen for an appropriate non-linear crystal for the laser's OPO process. Therefore, the laser presented to be unstable during the course of the experiments, which made it unsuitable for full-field metrology applications (the problem has now fixed with new technology). So a traditional electronic source was chosen for performing the experiments. That was a THz multiplier/mixer source from Virginia Diodes.

In Chapter 4, a new THz multiplier/mixer source was fully characterised together with a new pyroelectric detector in our lab. The characterisation concentrated on the operating parameters of the source combined with the detector and on the profile of the output beam. Studies on the stability of the measuring system were particularly focused. The linear parameters of the dependence of the phase noise to the inversed modulation amplitude are in agreement with the calculated theory. Experiment on temporal stability

of the system during 12 hours was taken and the results showed that the phase noise kept stable during the measured period. Study during this long period is needed as one phase-stepping DHI measurement takes several hours while scanning with one point pyroelectric detector. Therefore, the THz multiplier source and the pyroelectric detector are suitable for the full-field application in the THz DHI applications.

Phase-shifting DHI has been applied in the THz domain for the first time using a THz-multiplier source and scanning one point pyroelectric detector. Holograms of the resolution target and the test objects were recorded at 4 different phase-steps. Both phase and amplitude of the objects were reconstructed digitally using the already developed mathematical algorithms. The reconstructed images have a lateral resolution of 1.8 ± 0.3 mm and an axial resolution of 15 ± 5 mm. These measured resolutions are matched up with the theoretical calculation in Chapter 4 (the beam waist size).

In conclusion, the main contributions of the thesis research are: (i) Applying successfully multi-wavelength interferometry technique to overcome the conventional 2π ambiguity in the depth measurements using an all-optical THz source; (ii) Exploring potential spectroscopic application of the intra-cavity OPO THz laser on some specific ceramic types which have industrial interests; (iii) Studying phase-shifting digital DHI in THz domain where the technique was implemented for the first time at THz frequency in which both intensity and phase were reconstructed. The phase-shifting technique was applied to remove automatically the unwanted spectral orders so the quality of the reconstructed image is enhanced compared to non-phase-shifting holography.

Finally, each technology has its own advantages and disadvantages which make it suitable for each type of application. By now, commercial systems of THz radiation are becoming more and more common on the market; the applications of THz frequency are entering many industrial fields as well as everyday life. Hence THz metrology is becoming an emergent field as it will allow reliable measurements to support qualification control and manufacturing. From the author's point of view for the potential future full-field metrology applications, the sources of choice could be the THz QCLs when new technology is available to reach lower frequencies and room temperature operation because the price will be low and solid sources are typically toughen and stable. At present, pyroelectric detector is still a promising technology to be able to upgrade to 1 line or 2D detector. Micro-bolometer array could also be a good candidate to work with THz QCLs when it is available as the laser typical output power

is sufficiently large. For applications which do not require high spatial resolution, electronic sources like multiplier source used above are also a good choice. With current technology, THz intra-cavity OPO lasers still have exceptional features for metrology applications as the newest technology now has fixed the old problem.

With phase-shifting THz DHI, not only the shape, the thickness or the depth can be known from the DHI measurements, but more information can be extracted from the reconstructed images such as the refractive index, the stress, etc. Therefore, future research can be directed toward applying the technique for 3D refractive index determination and constrain measurement of the materials of industrial interest. In the current experiments, recording time for one set of phase-shifting holograms (4 holograms for 4 phase-steps algorithm) was 6 hours. When the technology is ready for 2D detector, recording time of holograms could be reduced to the scale of second or millisecond, and the technique will play an important role in full-field applications in industry metrology and/or non-destructive testing and evaluation.

Appendices

Internet link references are listed below.

A.1. List of THz and mm-wave synthesizers and sweepers from Insight Product

http://www.insight-product.com/products3.htm

THz & mm-wave Frequency Synthesizers & Sweepers: **36-2850 GHZ**	Wide Band THz Frequency Synthesizers from 36 to 1250 GHz Wide Band Ultra-fast THz Sweepers from 36 to 1250 GHz THz Frequency Synthesizer 0.45 THz to 2.85 THz
THz & mm-wave Vacuum Tube Based Sources: **36-1250 GHz**	BWO sources from 36 to 178 GHz BWO sources from 179 to 1250 GHz Power Supplies for BWO sources Automated power supply IPPS 2-6/60 Orotron (High-Power BWO) sources from 120 to 370 GHz Pulse Magnetrons up to 220 GHz and peak power up to 30 kW CW Microwave Magnetrons 915 MHz and 2450 MHz up to 100 kW Traveling Wave Tubes (TWTs) up to 26 GHz with peak power of 500 Watt Room Temperature Gyrotrons from 15 to 35 GHz Cryogenic Gyrotron Systems at 37.5 & 83 GHz Gyro-Klystrons at 34 GHz and 93 GHz Gyro-TWT at 34 GHz with 3.4 GHz bandwidth
Frequency Counters & Spectrum Analyzers: **70-170 GHz**	Millimeter Wave Frequency Counter 70-170 GHz Millimeter Wave Spectrum Analyzers, 35-178 GHz
Photon Counter/ Photon Registration System	Multi-Channel Optical Photon Registration System

THz & mm-wave Mixers, Detectors & Filters: **100 GHz - 70 THz**	Hot Electron Bolometer Mixers/Receivers up to 2.5 THz Hot Electon Bolometer Detectors up to 70 THz Room Temperature Detectors from 37.5 GHz up to 996 THz: Golay Cells Sensitive Terahertz Detectors: Cooled and Room Temperature Terahertz (THz) Detectors Mesh Filters from 0.9 to15 THz
mm-wave IMPATT Diodes: **30-140 GHz**	CW mm-wave IMPATT diodes from 30 to 140 GHz Pulse mm-wave IMPATT diodes from 30 to 140 GHz
Microwave and mm-wave PIN diodes: **1-140 GHz**	High-speed switching diodes from 33 to 140 GHz Microwave switching diodes from 1 to 40 GHz Microwave Variable-Capacitance diodes from 1 to 40 GHz Pulse P-I-N IMPATT Limiters 0.7-9.55 GHz Microwave Silicon Limiter PIN Diodes Miniature Silicon Diode Temperature Sensors Microwave hight temperature 4HSiC PIN Diode Microwave packaged hight temperature 4HSiC PIN Diode
Solid State Sources, CW & Pulsed: **26.5-280 GHz**	CW Cavity stabilized IMPATT from 26.5 to 140 GHz Pulsed IMPATT-based Generators from 26.5 to 140 GHz Cavity stabilized GUNN from 40 to 140 GHz Voltage controlled GUNN from 26.5 to 60 GHz Noise Generator at 94 GHz

EPR/ ESR/ DNP related sources:	Pulsed ESR/EPR: Pulse IMPATT power amplifier 26.5-140 GHz with up to 30 watt output power Pulsed and CW ESR/EPR: Quasi-continuous powerful millimeter (mm-wave) and sub-millimeter (sub-mm wave) Orotron Generator Pulse and CW ESR/EPR: Synthesizer up to 140 GHz Pulsed and CW ESR/EPR and DNP: Synthesizer 26.5-140 GHz with output power up to 30 watt Pulsed DNP: High-Power Pulsed Magnetron-based generators at 94 GHz
Solid State Power Amplifiers: 2.025 GHz to 14.5 GHz:	Solid State Power Amplifiers 2-14.5 GHz with up to 1000 Watt output power
THz Camera:	Compact 256 Pixel, 50 GHz to 0.7 THz Camera for Quality Control, NDT, and Screening on Conveyor Belt
Solid State Amplifiers: **26-178 GHz**	Pulse Amplifiers 26.5 to 140 GHz with up to 30 Watt output power Monolithic Balanced Mixers with an Intermediate Frequency, 26 to 178 GHz Low-Noise Parametric Amplfiers Monolithic Integrated Circuits (MIC) based

Contact:

Company E-mail:	**InsightProduct@yahoo.com**
Phone:	**(617) 965-8151**
Business Development:	**Arkady Gershteyn, V.P. Business Development; E-mail: ArkadyGer@gmail.com**

A.2. THz-multipliers series from Virginia Diodes

http://vadiodes.com/index.php/en/

High Power Multipliers (D Series)

The D-series multipliers are VDI's line of high-power / narrow-band varactor doublers. We offer D-series multipliers from ~50GHz to 500GHz with varying 3dB bandwidth, peak efficiency, and RF input power rating. VDI continues to make developments to its D-series products.

Please contact VDI for D-series multiplier recommendations based upon your frequency and power requirements. Click here to go to full band (WR series) multiplier page.

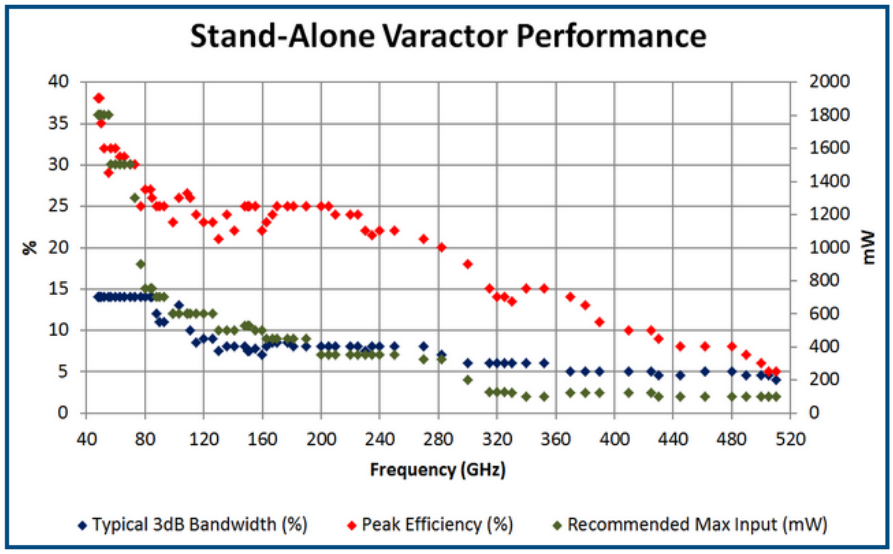

Relevant Links

- Broadband Multipliers
- Custom Sources and Receivers
- Signal Generator Extension Modules (SGX)

A.3. Golay Cell detectors from Tydex

http://www.tydexoptics.com/products/thz_optics/golay_cell

Golay Detectors

Golay Detector is one of the most efficient devices detecting THz radiation. It has excellent sensitivity at room temperature and flat optical response over a wide wavelength range. Tydex detectors are completely in-

house manufactured and calibrated. Every model is available from stock. Delivery includes a detector head and a power supply unit. A mount for the filters can be supplied as on option.

The various THz optical components and devices (e.g. low pass filters, band pass filters, polarizers, attenuators, windows, lenses, mirrors, waveplates, spectral splitters, and beam splitters) can be supplied as a useful complement for THz applications. Please find relevant chapters at our web site.

Tydex offers 3 models of Golay detectors:

1. GOLAY CELL GC-1P (detector with HDPE window)

2. GOLAY CELL GC-1T (detector with TPX window)

Due to polyethylene window exchange to TPX one, GC-1T detectors have a wider operation wavelength range spreading down to visible/UV. They can be considered a good substitute to Diamond window model as TPX has higher transmittance in THz than Diamond and surely cheaper than the latter one. So GC-1T model is only slightly expensive than GC-1P detector.

3. GOLAY CELL GC-1D (detector with diamond window)

Due to polyethylene window exchange to Diamond one, GC-1D detectors have a wider operation wavelength range spreading down to visible. They are usually used when not only THz and VIS ranges but also MIR is necessary. GC-1D model is a bit more expensive than GC-1T detector.

For price quotation and delivery please fax or e-mail us.

MODEL		GC-1P	GC-1T	GC-1D
Application: monitoring and control of		MIR and THz radiation	UV-NIR and THz radiation	VIS-THz radiation
Material of entrance window		High-Density Polyethylene (HDPE)	Polymethylpentene (TPX)	Diamond
Operating wavelength range, μm		15 ÷ 8000	0.3 ÷ 6.5 & 13 ÷ 8000	0.4 ÷ 8000
Diameter of entrance cone, mm		11.0		
Diameter of entrance window, mm		6.0		
Recommended detected power, W, not more than		1×10^{-3}		
For higher power THz attenuators are recommended		ATS-5-25.4, ATS-5-50.8		
Optimum modulation frequency, Hz:		15 ± 5		
Noise-equivalent power @ 15Hz, W/Hz$^{1/2}$:	typical	1.4×10^{-10}		
	min	0.8×10^{-10}		
Optical responsivity @ 15Hz, V/W:	typical	1×10^{3}		
	max	1.5×10^{3}		
Response rate, ms:	typical	30		
	min	25		
Detectivity (D*) at entrance cone aperture, cm x Hz$^{1/2}$ /W:	typical	7.0×10^{9}		
	max	11.0×10^{9}		
Ambient operating pressure range, mm Hg		$760 \div 10^{-3}$		
Operational and storage temperature range, °C		5 ÷ 40		
Humidity, %		0 ÷ 80		
Vibration		avoid vibrations at 1÷100 Hz		
Rated voltage, VAC		100/115±10%, 220/230±10%		
Line frequency, Hz		50 ÷ 60		
Overall dimensions, LxWxH, mm		126x45x87		
Weight, kg		0.8		

16 Domostroitelnaya str.
194292 St. Petersburg, Russia
www.tydex.ru

Phones: 7-812-3318702
Fax: 7-812-3092958
E-mail: optics@tydex.ru

TYDEX®

http://www.mtinstruments.com/downloads/Golay%20Cell%20Datasheet%20Revised.pdf

MICROTECH instruments, inc.

THz DETECTORS – GOLAY CELLS

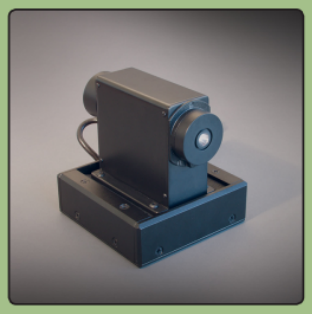

Product description:

Golay Cell is an opto-acoustic detector designed for operation in the spectral range 0.02-20 THz. It is equipped with a 6 mm diameter polyethylene input window that provides for high transparency at frequencies up to 20 THz. Golay Cell includes a built-in preamplifier. Operation of a Golay Cell requires a three-unit power supply delivering the following: +15 V, -15 V and 32 mA. Such a power supply is also available as an option. Performance of Golay Cells is detrimentally affected by mechanical vibrations. Addressing this problem, our Golay Cells are mounted on proprietary vibration-isolating bases.

Technical Specifications:

PARAMETER	VALUE
Responsivity at 12.5 Hz modulation	10^4 V/W
Sensitivity at 12.5 Hz modulation	10^{-8} W/H$^{1/2}$
Maximum modulation frequency	50 Hz
Dynamic range	100 nW - 1 mW
Rise time	25 ms
Maximum output voltage	3.0 V
Input window diameter	6 mm
Dimensions	135 x 115 x 120 mm

Operating Conditions:

PARAMETER	VALUE
Value Temperature	+15 to +25 °C
Pressure	8.4 x 10^4 to 10.7 x 10^4 Pa
Humidity	45 -80 %

Application Notes:

The Golay Cell can be used to detect both CW and pulsed THz radiation. However, due to a 25 ms response time, only average power can be measured for short pulse/high repetition rate THz sources.

Spectral response is lowered by transmission charactersistics of the input window.

Typical Golay Cell Responsivity Spectrum

GOLAY CELL WITH POLYETHYLENE WINDOW.
SN 190744

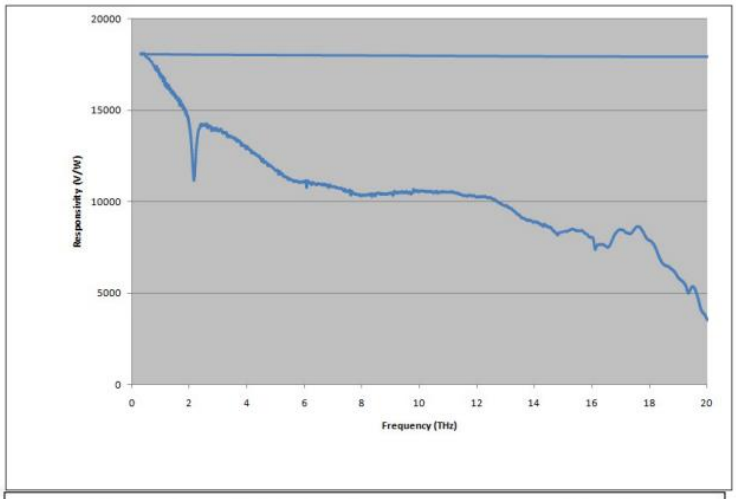

GOLAY CELL WITH DIAMOND WINDOW.
SN 180770

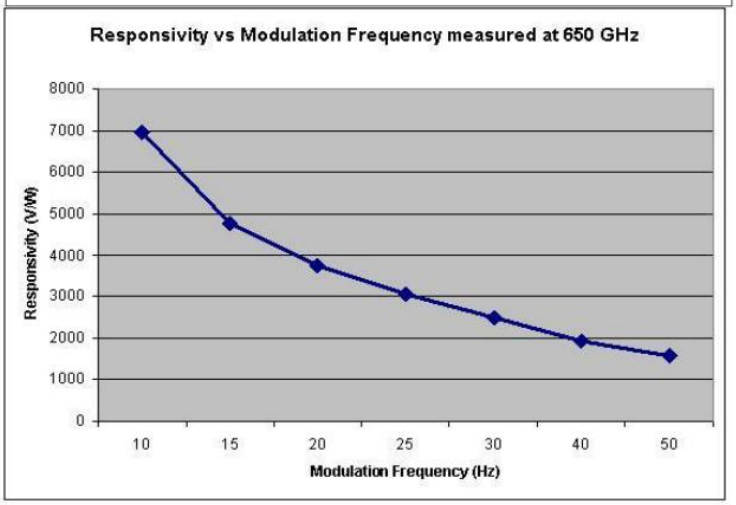

NOTES:

- Golay Cell responsivity was measured for a unit with 2 mm thick polyethylene input window at modulation frequency of 12.5 Hz.

Pricing information is available on request at sales@mtinstruments.com

858 W. Park St., Eugene, OR 97401, USA
Phone: 541-683-6505
Fax: 541-610-1825
www.mtinstruments.com

MICROTECH® instruments, inc.

A.4. Energy detectors

http://gentec-eo.com/Content/downloads/white-papers/Gentec-EO_HW_Energy_2014_V1.0.pdf

HOW IT WORKS

ENERGY DETECTORS

ENERGY DETECTORS AT GENTEC-EO

Gentec Electro Optics provides a full range of products to meet your pulse energy measurement needs. They range from the lean and portable QE12 and QE25 series, the large aperture QE50, QE65 and QE95 series to our large world class custom calorimeters. Having introduced the first pyroelectric joulemeter over 40 years ago Gentec-EO is well established as an experienced source of energy measurement expertise. Be it in the laboratory or an OEM application Gentec-EO will have a solution.

HOW THEY WORK

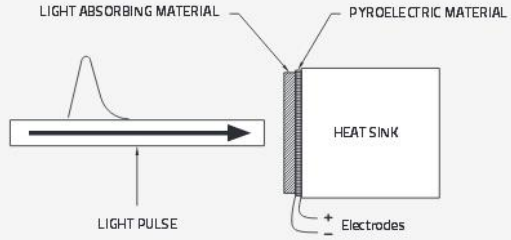

Figure 1. Joulemeter Construction

In the simplest terms, a pulse of light is absorbed by the surface of the detector and heats it up. That in turn, changes the temperature in a pyroelectric material underneath. This separates electrical charges in the pyroelectric which creates a voltage as the pulse of heat energy passes through it to a heat sink. The heat sink removes the heat energy to allow the pyroelectric to be ready for another pulse and to prevent it from over heating. The electrical voltage read by the measuring instrument is proportional to the energy. Figure 1 sketches out the basic structure of a pyroelectric joulemeter.

THE ABSORBER

The business end of the detector is the absorber that coats the side of the pyroelectric that is exposed to the laser. That material absorbs most of the light energy from the laser and converts it to heat. A small fraction is reflected. How much is shown by the spectral response curve for the material. The thermal mass of the absorber and its thickness determine how quickly the heat can flow to the pyroelectric detector and hence its response time. Lowering the thermal impedance by using an absorber with a lower thermal mass or reducing the thickness of the absorber will increase its speed. The metallic MT coating is a good example. It allows for a measurement of each pulse up to 4000-6000 Hz.

THE PYROELECTRIC

The heart of every Gentec-EO energy detector is a fast response pyroelectric material. It acts as a source of electrical current when subjected to changes in temperature provided by the absorber. Essentially it contains permanent electrical dipoles that are oriented in a specific direction. A rapid temperature change in the material will alter the orientation of these dipoles. That changes the internal electric field and causes an imbalance in electrical charge between the 2 large sides of the device. There are thin metal electrodes on these surfaces. They allow the charge to flow from one electrode into a circuit with a load resistor and then back to the crystal via the other electrode to eliminate the imbalance. The electrical current is converted into a voltage signal by the load resistor.

ENERGY DETECTORS

THE VOLTAGE RESPONSE

The result is a voltage pulse that rises quickly with the response time of the device to a level proportional to the laser energy (Figure 2). It then decays exponentially over a longer period of time that is a function of the pyroelectric device and load impedance. Figure 2 also shows that there is a longer recovery time to return to the initial state of the detector. This is a function of thermal phenomena and is not affected by the load impedance as are the rise and decay times. The integrated pulse energy over this period is proportional to the peak voltage.

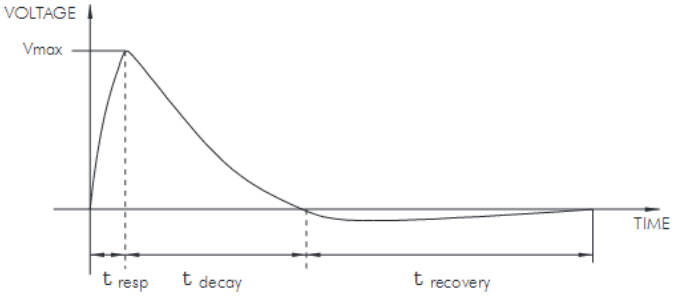

Figure 2.
Typical voltage response
of a Gentec-EO energy detector

THE MEASUREMENT

The laser energy is given by the change in voltage divided by the sensitivity (in Volts/Joule) of the detector. The measured voltage is the change from the initial reference voltage to the maximum voltage of the pulse. The sensitivity is provided by Gentec-EO on our NIST-traceable calibration certificate. We measure this with extreme care with a well known laser energy provided by an NIST standard. This sensitivity is for the specific load impedance that is requested. The user can measure the voltage on an oscilloscope or computer data acquisition system and use the sensitivity value to make the energy measurement. An easier option is to read it directly in Joules from a Gentec-EO MAESTRO or S-LINK monitor, or when using our new integra series.

THERMALLY ROBUST

The energy detector will make accurate measurements in spite of changing temperature in the environment or heating of the detector as long as the maximum voltage does not saturate. This is because it is the difference between the initial and peak voltages that measure the pulse energy. This relative measurement is good until the peak voltage is prevented from reaching its natural value by the maximum voltage available in the electronics.

DAMAGE THRESHOLDS

Excessive pulse energy that is concentrated into to a small area can damage energy detectors. For the most demanding laser beams we offer the broadband MB coating which has pulse energy density thresholds that are among the best in the world. Slight discoloration from short pulses is due to a modification of the organic material in the absorber that does not affect the detector calibration. If enough of the coating is removed by ablation to expose the metal electrode underneath, then the output voltage may be affected too much for the application. Too much average power, (that is above the manufacturer's specification) can cause the detector to overheat. Contamination on the absorber surface can also interfere with the measurement or damage the detector by concentrating too much energy in one spot. Grease, dust, and fingerprints are some of the common contaminants to avoid.

View our complete line of pyroelectric Energy Detectors on page 38

A.5. THz gas laser from Edinburgh Instruments

https://www.edinst.com/wp-content/uploads/2015/09/FIR-Series-Flyer.pdf

FIR Series of Products

FAR Infrared lasers/Terahertz lasers

EDINBURGH INSTRUMENTS
Photonics Division

With over 30 years expertise in designing and manufacturing a range of optically pumped FIR (Terahertz) lasers, our products are used in applications where coherent radiation in the range of 40 µm to 1.22mm (0.25 –7.5 THz) is required. When combined with our PL Series of CO_2 lasers the FIR laser becomes a powerful tool for taking laser line measurement at high peak powers.

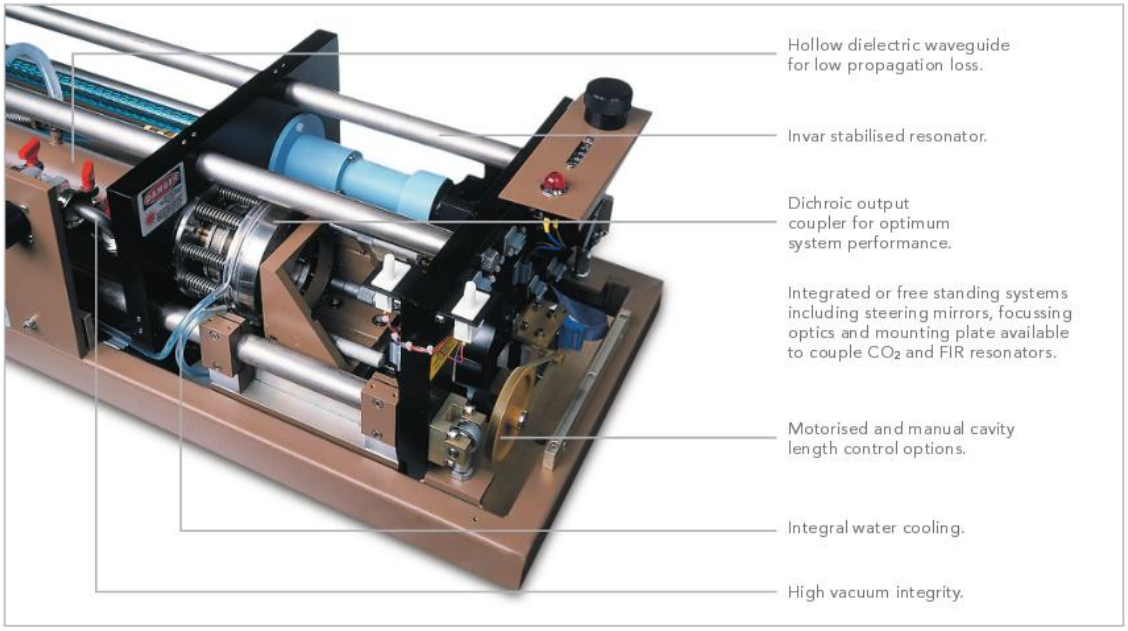

295

This model 295 is a stand-alone FIR laser designed for operation with high power CO_2 lasers. Guaranteed powers of 150mW when pumped by the PL5, and 500mW when pumped by the PL6, are available at 118.8µm and 184.3µm.

The 295 has a 3 bar invar support frame and features the same optical design as used in the FIRL 100. It has been engineered to allow UHV pumping for extended sealed operation, maximum power and number of lines.

395 Twin Laser

The model 395 features two identical FIR laser cavities within a single 5 bar invar stabilised frame. This is particularly designed for applications where two FIR outputs are required such as Plasma diagnostics, with one frequency offset from the other by up to a few MHz.

Both FIR cavities of the 395 are pumped by a single PL6 Laser to ensure optimum stability of the Intermediate Frequency (IF). A 50/50 beam splitter is used to generate the two identical pump beams required.

The output couplers of both FIR sections are mounted on precision linear translation stages for individual optimisation and to generate the cavity length difference for frequency offset.

FIRL 100

The model FIRL100 has both the CO_2 pump laser and the FIR laser housed in an integrated structure combining a highly efficient optically pumped FIR system into a single compact unit. The lasers and coupling optics are mounted within a 5 bar invar rod frame for excellent thermal and mechanical stability.

The CO_2 section provides 80 lines between 9.1µm and 10.9µm and features a flowing gas single discharge tube giving more than 50W on the strongest lines. Mode performance (M^2 <1.25) is assured by internal profiling of the tube and the use of high quality optics. The resonator design is based on the proven PL5 laser with diffraction grating, two ZnSe Brewster windows and piezo ceramic mounted ZnSe output coupler.

The CO_2 laser output is coupled into the FIR laser via two steering mirrors and a ZnSe focussing lens. Access to the CO_2 radiation beam diagnostics for Infrared experiments is available via a precision, two position sliding mirror mechanism.

FIRL 100 far infrared output specification

λ(μm)	FIR Molecule	CO_2 pump line	Typical Power
96.5	CH_3OH	9R10	60mW
118.8	CH_3OH	9P36	150mW
184.3	CH_2F_2	9R32	150mW
432.6	HCOOH	9R20	30mW
513.0	HCOOH	9R28	10mW

FIR laser frequencies arise from rotational transitions in an excited vibrational state of a polar gas molecule at low pressure. The optically pumped FIR laser relies on the selective absorption of tunable infrared radiation to create a population inversion between rotational states and hence generation laser action. In practice, a few molecules are chosen to provide discrete frequencies across the entire FIR spectrum from 40μm upwards. Tables of FIR lines are available on request.

A wide range of accessories are available for the FIR Series which include:

Laser stabilisers –
For applications demanding excellent medium and long term stability, an active stabiliser may be required. This will compensate for laser output fluctuations caused by changes in ambient conditions and lock the variation in laser frequency or power to a value close to the passive jitter.

Edinburgh Photonics has designed a family of active stabilisation techniques appropriate to the type of laser and operating conditions.

Laser Pumping and Refilling Systems –
All flowing gas laser systems are supplied with the necessary valves, gauges and vacuum couplings for simple connection to the system vacuum pump. A range of turbo molecular and dry scrolling pumps are available.

Gas Mixing Stations –
Designed to allow mixing and metering of up to 3 component gases from independent gas cylinders. These comprise of 3 inlet ports, each with their own needle valve control, with individual flow meters for gas mixing.

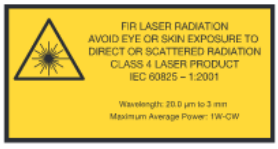

PROTECTIVE GLASSES ARE AVAILABLE FOR THE FIR SERIES OF CO_2 LASER

For more information contact us at **sales@edinst.com** or visit **www.edinburghphotonics.com**
T: +44(0) 1506 425 300
F: +44(0) 1506 425 320

Edinburgh Instruments
2 Bain Square,
Kirkton Campus,
Livingston,
EH54 7DQ
United Kingdom

Telephone
+44(0) 1506 425 300
Facsimile
+44(0) 1506 425 320

Email
sales@edinst.com
Website
www.edinburghphotonics.com

EDINBURGH INSTRUMENTS
Photonics Division

A.6. THz spectroscopy from TeraView

http://www.teraview.com/products/terahertz-pulsed-spectra-3000/terahertz-spectroscopy-modules/

Terahertz Spectroscopy Modules

Until now, FTIR spectroscopy with cooled Si bolometer (1.7 K) has provided the only means to access the terahertz spectral region. TeraView's terahertz spectrometers utilize powerful, ultra-fast Ti-Sapphire laser sources and semiconductor based detection systems to supply full access to the 0.06 – 4 THz (2 cm-1 - 120 cm-1) spectral region. Furthermore, TeraView's spectrometers do not require liquid helium cooling or any vacuum systems for its operation, enabling results to be obtained in a minute or less, all while operating under ambient temperature conditions.

TPS Spectra 3000

TPS Spectra 3000 from TeraView is the world's first commercial terahertz spectrometer capable of performing both transmission and attenuated total reflection (ATR) measurements. Its modular sample compartment also accepts reflectance imaging modules, variable temperature samples holders and cryostat accessories.

Key features:

- Terahertz transmission and reflectance measurements on solids, liquids, suspensions, slurries and films
- Spectral Range – 0.06 THz to 4 THz (2 cm^{-1} - 133 cm^{-1})
- Accommodates standard IR sampling accessories
- ATR modules for optimized measurements on as little as 1mg solid sample
- Solid-state emitter and detector for ambient temperature operation
- Bespoke optics casing with controlled alignment optics for system optimization

A.7. THz photomixers from Toptica

http://www.toptica.com/products/terahertz_generation/lasers_and_photomixers_for_cw_terahertz_generation/cw_terahertz_spectroscopy_extension.html

cw THz Packages: Lasers and Photomixers for Frequency-Domain THz Spectroscopy

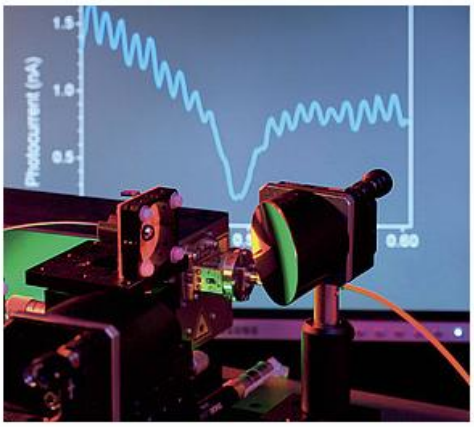

For frequency-domain terahertz spectroscopy, TOPTICA offers two "TopSeller" systems – TeraScan 1550 and TeraScan 780. Based on precisely tunable DFB lasers, digital control electronics, and latest GaAs and InGaAs photomixer technology, the TeraScan systems combine ease of use with best-in-class specifications.

A set of modular product packages extends the cw-terahertz product portfolio: The TeraBeam, a sub-system of the TeraScan, comprises two Distributed Feedback diode lasers with fiber-optic beam combination and digital driver electronics. The Tuning Range Extension pushes the useable bandwidth out to almost 3 THz, and the Phase Modulation Extension features two fiber stretchers for fast and accurate scanning of the terahertz phase. The packages can be combined and upgraded depending on the requirements of the experiment.

TOPTICA's cw terahertz systems have been developed in cooperation with some of the leading institutes in the world. Push-button terahertz spectroscopy has never been that easy!

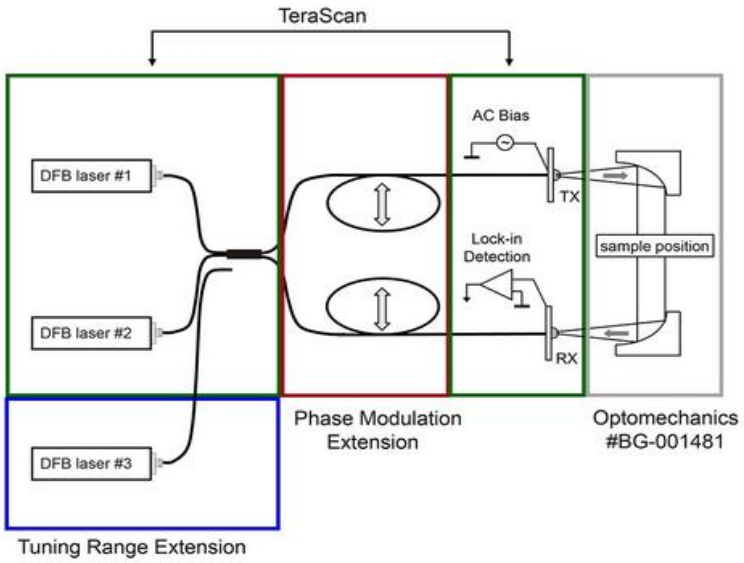

A.8. Breaking news on THz pasive cameras

http://www.esa.int/Our_Activities/Space_Engineering_Technology/TTP2/Space_camera_blazes_new_terahertz_trails

SPACE CAMERA BLAZES NEW TERAHERTZ TRAILS

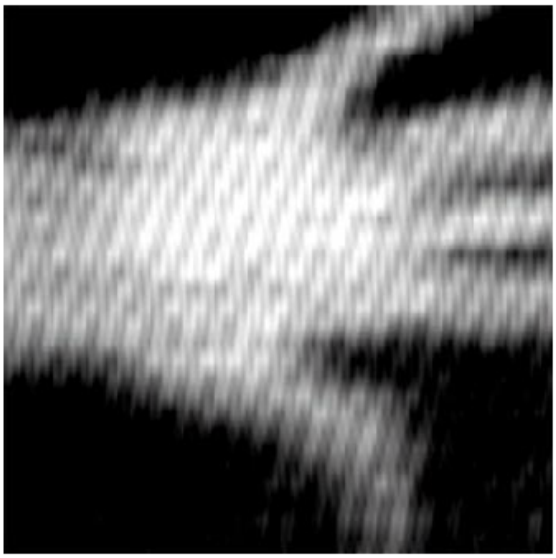

Terahertz reveals unexplored world

11 February 2003 New imaging technology came to life when ESA's StarTiger team captured the world's first terahertz picture of a human hand.

"When we started last June we set an ambitious goal: to build in four months the first compact submillimetre-wave imager with near real time image capturing using state-of-the-art micro-machining technology," said Peter de Maagt, ESA's StarTiger Project Manager, "we reached this goal when the first terahertz images were taken in September."

This breakthrough in terahertz imaging opens up the possibility for a new generation of applications, not only related to space but also in many non-space fields, including medicine, pharmaceuticals, security and aeronautics.

StarTiger is a new approach for conducting research and development (R&D) launched last year by ESA. The concept is to bring together a small group of highly motivated researchers, grant them full access to laboratory and production facilities, remove all administrative distractions, and let them work for an intense period of four to six months. The goal is to achieve a quantum increase in a promising and important technology within a short period of time.

The first project was started at CCLRC Rutherford Appleton Laboratory (RAL) in June 2002 and was scheduled for four months. RAL was chosen as the best location for this particular pilot project with its advanced laboratories and all support technology required, and its specific expertise in relevant fields.

http://www.embedded.com/print/4155522

ESA makes breakthrough in terahertz imaging technology

Stephanie Gordon - February 11, 2003

ESA makes breakthrough in terahertz imaging technology
The European Space Agency's (ESA) StarTiger research and development team has released pictures of what they claim is the world's first terahertz picture of a human hand.

According to Peter de Maagt, ESA's StarTiger project manager, the applications for terahertz imaging not only include space-related applications but also non-space fields including medicine, security and aeronautics.

"When we started last June we set an ambitious goal: to build in four months the first compact submillimetre-wave imager with near real time image capturing using state-of-the-art micro-machining technology," said de Maagt.

The imager built by the team of researchers based at the Rutherford Appleton Laboratory, takes pictures at 0.25 and 0.3THz, creating a two-colour picture to contrast between materials with different transmission and reflection properties. According to de Maagt, the main advantage of a terahertz imager is that it does not emit any radiation and it is a passive camera, capturing pictures of the natural terahertz rays emitted by almost all objects.

Occupying a portion of the spectrum between infrared and microwaves, from 10Â¹Â¹ to 10Â¹Â³ Hertz, terahertz waves can pass easily through some solid materials, like walls and clothes and can also be focused as light to create images of objects.

A working prototype of the imager was developed last September by the 11-member research team but the resolution of 8x8 pixels was too low and the time needed to acquire the image was too long. The team then took the techniques further and pushed the development of a lithographically and micro-machined detector array.

"The final version was an enhanced imaging system incorporating a two-colour 16-pixel detector array of the size of a postage stamp. This advanced system incorporated revolutionary silicon micro-electrical-mechanical systems (MEMs) technology," said project member, Chris Mann.

"The enhanced system delivered images that confirmed the mysterious nature of terahertz waves. An imager can show details of features under the skin, confirming the potential of this technique."

Attempts to construct a camera operating in the submillimetre wave range have so far resulted in very bulky solutions as these cameras have primarily been based on waveguide-based technology and usually assembled from discrete elements, according to the team. The recent advances in micro-machining offered the potential for the realisation of the same performance with much smaller physical dimensions.

"The StarTiger imager fits within a briefcase, is easy transportable. The core of the instruments is the size of a cigarette package," said Peter de Maagt. "Next generation instruments will go for another magnitude smaller size, by using electronic scanning."

The StarTiger project is a new method of R&D launched last year by the ESA to achieve increased productivity and results by providing researchers full access to laboratory and production facilities, removing all administrative distractions, and letting them work for an intense period of four to six months, according to the ESA.

"With StarTiger we want to dramatically reduce the turnaround time for state-of-the art technology developments. This we have demonstrated as possible with this first StarTiger project," said Niels Jensen, ESA's Head of Technology Programmes Department.

"Putting together a highly motivated team in the same laboratory for an intense period with everything they can possibly require, we can create a synergy not attainable to the same extent in conventional R&D. This provides a real chance to advance a well-defined key technology and reach a scientific breakthrough within a relative short period," said Jensen.

"We intend to use this approach for selected key technologies in the future. The location for projects will of course change from project to project. The objective is to select the best European laboratory for the each specific technology, to provide the best support for the teams," said Jensen.

http://www.digitalbarriers.com/sectors/

SMARTER SURVEILLANCE SOLUTIONS

Digital Barriers designs, develops, manufactures and sells visually intelligent surveillance technology to safeguard people, assets and infrastructure.

We operate globally and have customers in more than 50 countries, ranging from international homeland security and defence forces to customers in the global commercial market

COMMERCIAL SOLUTIONS

We protect public transportation systems, multi-national corporations and high-profile locations such as airports and oil and gas facilities.

Find out more

DEFENCE SOLUTIONS

Our innovative technology is proven in some of the world's most demanding environments to enhance the operations of law enforcement and the military as well as protect them from harm.

Find out more

About Us ›

SAFER. STRONGER. MORE SECURE.

How our solutions are helping organisations with surveillance, security and safety worldwide.

Our innovative new technology is used all over the world to enhance security as well as save time and money.

Sky News Coverage: Protecting public safety

Sky News Report: See how our passive camera ThruVis protects the public from terrorists by detecting suicide bombs and concealed weapons.

Find out more

Passive people screening at airports

How we enable airport authorities to add an extra layer of security without hindering internal staff from doing their job or adding to lengthening passenger queues.

Find out more

ThruVis wins Frost & Sullivan Award

Digital Barriers' unique passive people-screening camera has won a prestigious Frost & Sullivan Best Practices Award.

Find out more

Contact Us ›

A.9. Measuring laser power and energy output

http://www.coherent.com/downloads/AboutMeasuringLaserPowerndEnergyOutputFinal.pdf

COHERENT

Measuring Laser Power and Energy Output

Introduction

The most fundamental method of checking the performance of a laser is to measure its power or energy output. Laser output directly affects a laser's ability to perform a process. Measuring and monitoring this parameter is often very important from the time a laser is first manufactured, through system integration, and on to the final end customer who will be using the laser system in applications as far-ranging as medical, scientific, biomedical, and industrial applications.

There are several key decisions to be made when choosing the right measurement equipment for the job. Just as there are many different types of lasers with widely varying specifications, there are different measurement technologies available that are appropriate for specific types of lasers and matched to particular laser specifications. This paper will discuss the basics of laser power and energy measurement and guide you through the process of selecting the best instrument for the task.

It will be useful to define the terminology used to describe these devices within the photonics industry. These types of measurement systems usually involve two pieces of equipment that are often sold separately: First is a sensor that is placed into the laser beam and provides a signal output proportional to the laser input. The second component is the meter, which is an analysis and display instrument that will interpret the signal from the sensor, apply various analog and digital corrections (such as compensating for the difference between the calibration wavelength and the wavelength of the laser), and then provide a measurement. Some meters provide a measurement that must be viewed on the display, while other meters can provide more sophisticated data analysis and PC interfacing options.

Laser Power & Energy Technical Background

The first thing to take into consideration when shopping for a laser measurement system is the fundamental measurement that is needed – measurement of power or pulse energy.

First, it will be useful to cover what these two measurements are referring to. The power of a laser is measured in Watts (and often reported in terms of nW, mW, W, etc.). This is referring to the optical power output of the laser beam, which is the continuous power output of continuous wave (CW) lasers, or the average power of a pulsed or modulated laser.

The energy of a laser typically refers to the output of a pulsed laser and is related to the power output, where the energy (E) is the laser's peak power (P_{PEAK}) multiplied by the laser pulse duration (t):

$$E = P_{PEAK} \times t.$$

The average power of a pulsed laser (P_{AVG}) is the pulse energy (E) multiplied by the laser repetition rate (Hz):

$$P_{AVG} = E \times Hz$$

For example, an Excimer laser might have a 10 ns pulse width, energy of 10 mJ per pulse, and operates at a repetition rate of 10 pulses per second. This laser has a peak power of:

$$P_{PEAK} = 10\ mJ / 10\ ns = 1\ MW,$$

and average power of:

$$P_{AVG} = 10\ mJ \times 10\ (1/s) = 100\ mW.$$

The pulse length can be very short (i.e. picoseconds or femtoseconds) resulting in very high peak powers with relatively low pulse energy, or can be very long (i.e. milliseconds) resulting in low peak power and high pulse energy, while each of these conditions might have similar average power levels.

Throughout the rest of this paper when laser power is referred to, it is referencing the average power of pulsed lasers, or the power output of CW lasers.

Sensors Used to Measure Laser Power & Energy

Now that the fundamentals of laser power and energy have been covered it will be useful to describe the key types of measurement technologies commonly available in the market for measuring these different types of lasers. The most common measurement technologies are pyroelectric sensors that can only measure pulsed lasers, thermopiles that can measure pulsed or CW lasers, and semiconductor photodiodes (commonly referred to as optical sensors) that are sometimes restricted to CW-only lasers and can sometimes be used with both pulsed and CW lasers, depending upon the intended use.

A.10. Notes on lock-in amplifier from Stanford Research Systems

http://www.thinksrs.com

About Lock-In Amplifiers

Application Note #3

Lock-in amplifiers are used to detect and measure very small AC signals—all the way down to a few nanovolts. Accurate measurements may be made even when the small signal is obscured by noise sources many thousands of times larger. Lock-in amplifiers use a technique known as phase-sensitive detection to single out the component of the signal at a specific reference frequency and phase. Noise signals, at frequencies other than the reference frequency, are rejected and do not affect the measurement.

Why Use a Lock-In?

Let's consider an example. Suppose the signal is a 10 nV sine wave at 10 kHz. Clearly some amplification is required to bring the signal above the noise. A good low-noise amplifier will have about 5 nV/√Hz of input noise. If the amplifier bandwidth is 100 kHz and the gain is 1000, we can expect our output to be 10 µV of signal (10 nV × 1000) and 1.6 mV of broadband noise (5 nV/√Hz × √100 kHz × 1000). We won't have much luck measuring the output signal unless we single out the frequency of interest.

If we follow the amplifier with a band pass filter with a Q=100 (a VERY good filter) centered at 10 kHz, any signal in a 100 Hz bandwidth will be detected (10 kHz/Q). The noise in the filter pass band will be 50 µV (5 nV/√Hz × √100 Hz × 1000), and the signal will still be 10 µV. The output noise is much greater than the signal, and an accurate measurement can not be made. Further gain will not help the signal-to-noise problem.

Now try following the amplifier with a phase-sensitive detector (PSD). The PSD can detect the signal at 10 kHz with a bandwidth as narrow as 0.01 Hz! In this case, the noise in the detection bandwidth will be 0.5 µV (5 nV/√Hz × √.01 Hz × 1000), while the signal is still 10 µV. The signal-to-noise ratio is now 20, and an accurate measurement of the signal is possible.

What is Phase-Sensitive Detection?

Lock-in measurements require a frequency reference. Typically, an experiment is excited at a fixed frequency (from an oscillator or function generator), and the lock-in detects the response from the experiment at the reference frequency. In the following diagram, the reference signal is a square wave at frequency ω_r. This might be the sync output from a function generator. If the sine output from the function generator is used to excite the experiment, the response might be the signal waveform shown below. The signal is $V_{sig}\sin(\omega_r t + \theta_{sig})$ where V_{sig} is the signal amplitude, ω_r is the signal frequency, and θ_{sig} is the signal's phase.

Lock-in amplifiers generate their own internal reference signal usually by a phase-locked-loop locked to the external reference. In the diagram, the external reference, the lock-in's reference, and the signal are all shown. The internal reference is $V_L\sin(\omega_L t + \theta_{ref})$.

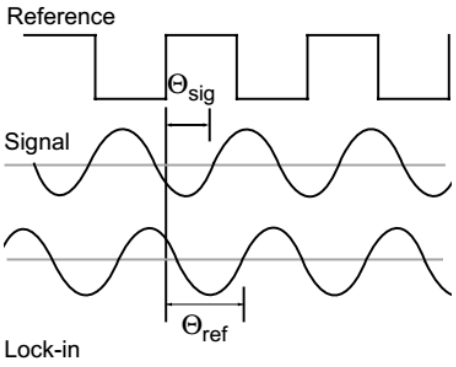

The lock-in amplifies the signal and then multiplies it by the lock-in reference using a phase-sensitive detector or multiplier. The output of the PSD is simply the product of two sine waves.

$$V_{psd} = V_{sig}V_L\sin(\omega_r t + \theta_{sig})\sin(\omega_L t + \theta_{ref})$$

$$= \tfrac{1}{2}V_{sig}V_L\cos([\omega_r - \omega_L]t + \theta_{sig} - \theta_{ref}) - \tfrac{1}{2}V_{sig}V_L\cos([\omega_r + \omega_L]t + \theta_{sig} + \theta_{ref})$$

The PSD output is two AC signals, one at the difference frequency ($\omega_r - \omega_L$) and the other at the sum frequency ($\omega_r + \omega_L$).

If the PSD output is passed through a low pass filter, the AC signals are removed. What will be left? In the general case, nothing. However, if ω_r equals ω_L, the difference frequency component will be a DC signal. In this case, the filtered PSD output will be:

$$V_{psd} = \tfrac{1}{2}V_{sig}V_L\cos(\theta_{sig} - \theta_{ref})$$

This is a very nice signal—it is a DC signal proportional to the signal amplitude.

It's important to consider the physical nature of this multiplication and filtering process in different types of lock-ins. In traditional analog lock-ins, the signal and reference are analog voltage signals. The signal and reference are multiplied in an analog multiplier, and the result is filtered with one or more stages of RC filters. In a digital lock-in, such as the SR830 or SR850, the signal and reference are represented by sequences of numbers. Multiplication and filtering are performed mathematically by a digital signal processing (DSP) chip. We'll discuss this in more detail later.

Narrow Band Detection

Let's return to our generic lock-in example. Suppose that instead of being a pure sine wave, the input is made up of signal plus noise. The PSD and low pass filter only detect

signals whose frequencies are very close to the lock-in reference frequency. Noise signals, at frequencies far from the reference, are attenuated at the PSD output by the low pass filter (neither $\omega_{noise} - \omega_{ref}$ nor $\omega_{noise} + \omega_{ref}$ are close to DC). Noise at frequencies very close to the reference frequency will result in very low frequency AC outputs from the PSD ($|\omega_{noise} - \omega_{ref}|$ is small). Their attenuation depends upon the low pass filter bandwidth and rolloff. A narrower bandwidth will remove noise sources very close to the reference frequency; a wider bandwidth allows these signals to pass. The low pass filter bandwidth determines the bandwidth of detection. Only the signal at the reference frequency will result in a true DC output and be unaffected by the low pass filter. This is the signal we want to measure.

Where Does the Lock-In Reference Come From?

We need to make the lock-in reference the same as the signal frequency, i.e. $\omega_r = \omega_L$. Not only do the frequencies have to be the same, the phase between the signals can not change with time. Otherwise, $\cos(\theta_{sig} - \theta_{ref})$ will change and V_{psd} will not be a DC signal. In other words, the lock-in reference needs to be phase-locked to the signal reference.

Lock-in amplifiers use a phase-locked loop (PLL) to generate the reference signal. An external reference signal (in this case, the reference square wave) is provided to the lock-in. The PLL in the lock-in amplifier locks the internal reference oscillator to this external reference, resulting in a reference sine wave at ω_r with a fixed phase shift of θ_{ref}. Since the PLL actively tracks the external reference, changes in the external reference frequency do not affect the measurement.

Internal Reference Sources

In the case just discussed, the reference is provided by the excitation source (the function generator). This is called an external reference source. In many situations the lock-in's internal oscillator may be used instead. The internal oscillator is just like a function generator (with variable sine output and a TTL sync) which is always phase-locked to the reference oscillator.

Magnitude and Phase

Remember that the PSD output is proportional to $V_{sig}\cos\theta$, where $\theta = (\theta_{sig} - \theta_{ref})$. θ is the phase difference between the signal and the lock-in reference oscillator. By adjusting θ_{ref} we can make θ equal to zero. In which case we can measure V_{sig} ($\cos\theta = 1$). Conversely, if θ is 90°, there will be no output at all. A lock-in with a single PSD is called a single-phase lock-in and its output is $V_{sig}\cos\theta$.

This phase dependency can be eliminated by adding a second PSD. If the second PSD multiplies the signal with the reference oscillator shifted by 90°, i.e. $V_L\sin(\omega_L t + \theta_{ref} + 90°)$, its low pass filtered output will be:

$$V_{psd2} = \tfrac{1}{2}V_{sig}V_L\sin(\theta_{sig} - \theta_{ref})$$

$$V_{psd2} \sim V_{sig}\sin\theta$$

Now we have two outputs: one proportional to $\cos\theta$ and the other proportional to $\sin\theta$. If we call the first output X and the second Y,

$$X = V_{sig}\cos\theta \qquad Y = V_{sig}\sin\theta$$

these two quantities represent the signal as a vector relative to the lock-in reference oscillator. X is called the 'in-phase' component and Y the 'quadrature' component. This is because when $\theta = 0$, X measures the signal while Y is zero.

By computing the magnitude (R) of the signal vector, the phase dependency is removed.

$$R = (X^2 + Y^2)^{1/2} = V_{sig}$$

R measures the signal amplitude and does not depend upon the phase between the signal and lock-in reference.

A dual-phase lock-in has two PSDs with reference oscillators 90° apart, and can measure X, Y and R directly. In addition, the phase (θ) between the signal and lock-in is defined as:

$$\theta = \tan^{-1}(Y/X)$$

Digital PSD vs. Analog PSD

We mentioned earlier that the implementation of a PSD is different for analog and digital lock-ins. A digital lock-in, such as the SR830, multiplies the signal with the reference sine waves digitally. The amplified signal is converted to digital form using a 16-bit A/D converter sampling at 256 kHz. The A/D converter is preceeded by a 102 kHz anti-aliasing filter to prevent higher frequency inputs from aliasing below 102 kHz.

This input data stream is multiplied, a point at a time, with the computed reference sine waves described previously. Every 4 µs the input signal is sampled, and the result is multiplied by both reference sine waves (90° apart).

The phase sensitive detectors (PSDs) in the digital lock-in act as linear multipliers; that is, they multiply the signal with a reference sine wave. Analog PSDs (both square wave and linear) have many problems associated with them. The main problems are harmonic rejection, output offsets, limited dynamic reserve, and gain error.

The digital PSD multiplies the digitized signal with a digitally computed reference sine wave. Because the reference sine waves are computed to 20 bits of accuracy, they have very low harmonic content. In fact, the harmonics are at the −120 dB level! This means that the signal is multiplied by a single reference sine wave (instead of a reference and its many harmonics), and only the signal at this single reference frequency is detected. The SR810, SR830 and SR850 digital lock-ins are completely insensitive to signals at harmonics of the reference. In contrast, a square wave multiplying lock-in will detect at all of the odd harmonics of the reference (a square wave contains many large odd harmonics).

Output offset is a problem because the signal of interest is a DC output from the PSD, and an output offset contributes to error and zero drift. The offset problems of analog PSDs are eliminated using the digital multiplier. There are no erroneous DC output offsets from the digital multiplication of the signal and reference. In fact, the actual multiplication is virtually error free.

The dynamic reserve of an analog PSD is limited to about 60 dB. When there is a large noise signal present, 1000 times (or 60 dB) greater than the full-scale signal, the analog PSD measures the signal with an error. The error is caused by non-linearity in the multiplication (the error at the output depends upon the amplitude of the input). This error can be quite large (10 % of full scale) and depends upon the noise amplitude, frequency and waveform. Since noise generally varies quite a bit in these parameters, the PSD error causes a lot of output uncertainty.

In the digital lock-in, dynamic reserve is limited by the quality of the A/D conversion. Once the input signal is digitized, no further errors are introduced. Certainly, the accuracy of the multiplication does not depend on the size of the numbers. The A/D converter used in the SR810, SR830 and SR850 is extremely linear, meaning that the presence of large noise signals does not impair its ability to correctly digitize a small signal. In fact, the dynamic reserve of these lock-ins can exceed 100 dB without any problems. We'll talk more about dynamic reserve a little later.

A linear, analog PSD multiplies the signal by an analog reference sine wave. Any amplitude variation in the reference amplitude shows up directly as a variation in the overall gain. Analog sine-wave generators are susceptible to amplitude drift: especially as a function of temperature. The digital reference sine wave has a precise amplitude and never changes. This avoids a major source of gain error common to analog lock-ins.

The overall performance of a lock-in amplifier is largely determined by the performance of its phase sensitive detectors. In virtually all respects, the digital PSD outperforms its analog counterparts.

What Does a Lock-In Measure?

So what exactly does the lock-in measure? Fourier's theorem basically states that any input signal can be represented as the sum of many sine waves of differing amplitudes, frequencies and phases. This is generally considered as representing the signal in the "frequency domain". Normal oscilloscopes display the signal in the "time domain". Except in the case of clean sine waves, the time domain representation does not convey very much information about the various frequencies which make up the signal.

A lock-in multiplies the signal by a pure sine wave at the reference frequency. All components of the input signal are multiplied by the reference simultaneously. Mathematically speaking, sine waves of differing frequencies are orthogonal, i.e. the average of the product of two sine waves is zero unless the frequencies are EXACTLY the same. The product of this multiplication yields a DC output signal proportional to the component of the signal whose frequency is exactly locked to the reference frequency. The low pass filter (which follows the multiplier) provides the averaging which removes the products of the reference with components at all other frequencies.

A lock-in amplifier, because it multiplies the signal with a pure sine wave, measures the single Fourier (sine) component of the signal at the reference frequency. Let's take a look at an example. Suppose the input signal is a simple square wave at frequency f. The square wave is actually composed of many sine waves at multiples of f with carefully related amplitudes and phases. A 2 Vpp square wave can be expressed as:

$$S(t) = 1.273\sin(\omega t) + 0.4244\sin(3\omega t) + 0.2546\sin(5\omega t) + ...$$

where $\omega = 2\pi f$. The lock-in, locked to f, will single out the first component. The measured signal will be $1.273\sin(\omega t)$, not the 2 Vpp that you'd measure on a scope.

In the general case, the input consists of signal plus noise. Noise is represented as varying signals at all frequencies. The ideal lock-in only responds to noise at the reference frequency. Noise at other frequencies is removed by the low pass filter following the multiplier. This "bandwidth narrowing" is the primary advantage that a lock-in amplifier provides. Only inputs with frequencies at the reference frequency result in an output.

RMS or Peak?

Lock-in amplifiers, as a general rule, display the input signal in volts rms. When a lock-in displays a magnitude of 1 V (rms), the component of the input signal (at the reference frequency) is a sine wave with an amplitude of 1 Vrms, or 2.8 Vpp.

Thus, in the previous example with a 2 Vpp square wave input, the lock-in would detect the first sine component, $1.273\sin(\omega t)$. The measured and displayed magnitude would be 0.90 Vrms (or $1.273/\sqrt{2}$).

Degrees or Radians?

In this discussion, frequencies have been referred to as f (Hz) and ω ($2\pi f$ radians/s). This is because people measure frequencies in cycles per second, and math works best in radians. For purposes of measurement, frequencies as measured in a lock-in amplifier are in Hz. The equations used to explain the actual calculations are sometimes written using ω to simplify the expressions.

Phase is always reported in degrees. Once again, this is more by custom than by choice. Equations written as $\sin(\omega t + \theta)$ are written as if θ is in radians, mostly for simplicity. Lock-in amplifiers always manipulate and measure phase in degrees.

Dynamic Reserve

The term "dynamic reserve" comes up frequently in discussions about lock-in amplifiers. It's time to discuss this

term in a little more detail. Assume the lock-in input consists of a full-scale signal at f_{ref} plus noise at some other frequency. The traditional definition of dynamic reserve is the ratio of the largest tolerable noise signal to the full-scale signal, expressed in dB. For example, if full scale is 1 µV, then a dynamic reserve of 60 dB means noise as large as 1 mV (60 dB greater than full scale) can be tolerated at the input without overload.

The problem with this definition is the word "tolerable". Clearly, the noise at the dynamic reserve limit should not cause an overload anywhere in the instrument—not in the input signal amplifier, PSD, low pass filter or DC amplifier. This is accomplished by adjusting the distribution of the gain. To achieve high reserve, the input signal gain is set very low so the noise is not likely to overload. This means that the signal at the PSD is also very small. The low pass filter removes the large noise components from the PSD output which allows the remaining DC component to be amplified (a lot) to reach 10 V full scale. There is no problem running the input amplifier at low gain. However, as we have discussed previously, analog lock-ins have a problem with high reserve because of the linearity of the PSD and the DC offsets of the PSD and DC amplifier. In an analog lock-in, large noise signals almost always disturb the measurement in some way.

The most common problem is a DC output error caused by the noise signal. This can appear as an offset or as a gain error. Since both effects are dependent upon the noise amplitude and frequency, they can not be offset to zero in all cases and will limit the measurement accuracy. Because the errors are DC in nature, increasing the time constant does not help. Most lock-ins define tolerable noise as levels which do not affect the output more than a few percent of full scale. This is more severe than simply not overloading.

Another effect of high dynamic reserve is to generate noise and drift at the output. This comes about because the DC output amplifier is running at very high gain, and low-frequency noise and offset drift at the PSD output or the DC amplifier input will be amplified and appear large at the output. The noise is more tolerable than the DC drift errors since increasing the time constant will attenuate the noise. The DC drift in an analog lock-in is usually on the order of 1000 ppm/°C when using 60 dB of dynamic reserve. This means that the zero point moves 1 % of full scale over 10 °C temperature change. This is generally considered the limit of tolerable.

Lastly, dynamic reserve depends on the noise frequency. Clearly noise at the reference frequency will make its way to the output without attenuation. So the dynamic reserve at f_{ref} is 0 dB. As the noise frequency moves away from the reference frequency, the dynamic reserve increases. Why? Because the low pass filter after the PSD attenuates the noise components. Remember, the PSD outputs are at a frequency of $|f_{noise} - f_{ref}|$. The rate at which the reserve increases depends upon the low pass filter time constant and rolloff. The reserve increases at the rate at which the filter rolls off. This is why 24 dB/oct filters are better than 6 or 12 dB/oct filters. When the noise frequency is far away, the reserve is limited by the gain distribution and overload level of each gain element. This reserve level is the dynamic reserve referred to in the specifications.

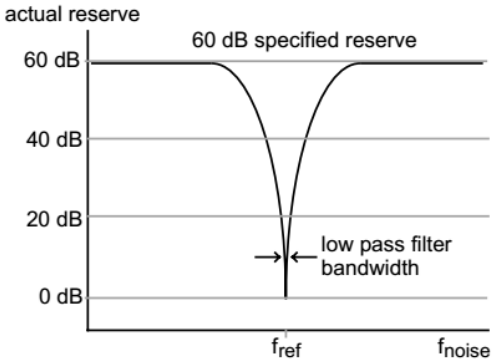

The above graph shows the actual reserve vs. the frequency of the noise. In some instruments, the signal input attenuates frequencies far outside the lock-in's operating range (f_{noise}>>100 kHz). In these cases, the reserve can be higher at these frequencies than within the operating range. While this creates a nice specification, removing noise at frequencies very far from the reference does not require a lock-in amplifier. Lock-ins are used when there is noise at frequencies near the signal. Thus, the dynamic reserve for noise within the operating range is more important.

Dynamic Reserve in Digital Lock-Ins

The SR810, SR830 and SR850, with their digital phase sensitive detectors, do not suffer from DC output errors caused by large noise signals. The dynamic reserve can be increased to above 100 dB without measurement error. Large noise signals do not cause output errors from the PSD. The large DC gain does not result in increased output drift.

In fact, the only drawback to using ultra-high dynamic reserves (>60 dB) is the increased output noise due to the noise of the A/D converter. This increase in output noise is only present when the dynamic reserve is increased above 60 dB *and* above the minimum reserve. (If the minimum reserve is 80 dB, then increasing to 90 dB may increase the noise. As we'll discuss next, the minimum reserve does not have increased output noise: no matter how large it is.)

To set a scale, the digital lock-in's output noise at 100 dB dynamic reserve is only measurable when the signal input is grounded. Let's do a simple experiment. If the lock-in reference is at 1 kHz, and a large signal is applied at 9.5 kHz, what will the lock-in output be? If the signal is increased to the dynamic reserve limit (100 dB greater than full scale), the output will reflect the noise of the signal at 1 kHz. The spectrum of any pure sine generator always has a noise floor, i.e. there is some noise at all frequencies. So even though the

applied signal is at 9.5 kHz, there will be noise at all other frequencies, including the 1 kHz lock-in reference. This noise will be detected by the lock-in and appear as noise at the output. This output noise will typically be greater than the lock-in's own output noise. In fact, virtually all signal sources will have a noise floor which will dominate the lock-in output noise. Of course, noise signals are generally much noisier than pure sine generators and will have much higher broadband noise floors.

If the noise does not reach the reserve limit, the digital lock-in's own output noise may become detectable at ultra-high reserves. In this case, simply lower the dynamic reserve and the DC gain will decrease, and the output noise will decrease also. In general, do not run with more reserve than necessary. Certainly don't use ultra-high reserve when there is virtually no noise at all.

The frequency dependence of dynamic reserve is inherent in the lock-in detection technique. The SR810, SR830 and SR850, by providing more low-pass filter stages, can increase the dynamic reserve close to the reference frequency. The specified reserve applies to noise signals within the operating range of the lock-in, i.e. frequencies below 100 kHz. The reserve at higher frequencies is actually greater but is generally not that useful.

Minimum Dynamic Reserve

The SR810, SR830 and SR850 always have a minimum amount of dynamic reserve. This minimum reserve changes with the sensitivity (gain) of the instrument. At high gains (full-scale sensitivity of 50 µV and below), the minimum dynamic reserve increases from 37 dB at the same rate as the sensitivity increases. For example, the minimum reserve at 5 µV sensitivity is 57 dB. In many analog lock-ins, the reserve can be lower. Why can't the digital lock-ins run with lower reserve at this sensitivity?

The answer to this question is: “Why would you want lower reserve?” In an analog lock-in, lower reserve means less output error and drift. In the SR800 series lock-ins, more reserve does not increase the output error or drift. But, more reserve can increase the output noise. However, if the analog signal gain before the A/D converter is high enough, the 5 nV/√Hz noise of the signal input will be amplified to a level greater than the input noise of the A/D converter. At this point, the detected noise will reflect the actual noise at the signal input and not the A/D converter's noise. Increasing the analog gain (decreasing the reserve) will not decrease the output noise. Thus, there is no reason to decrease the reserve. At a sensitivity of 5 µV, the analog gain is sufficiently high so that A/D converter noise is not a problem. Sensitivities below 5 µV do not require any more gain since the signal-to-noise ratio will not be improved (the front-end noise dominates). The SR800 series lock-ins do not increase their gain below the 5 µV sensitivity. Instead, the minimum reserve increases. Of course, the input gain can be decreased and the reserve increased; in which case, the A/D converter noise might be detected in the absence of any signal input.

Dynamic Reserve in Analog Lock-Ins

Because of the limitations of their PSDs, analog lock-in amplifiers must use different techniques to improve their dynamic reserve. The most common of these is the use of analog prefilters. The SR510 and SR530 have tunable, band-pass filters at their inputs. The filters are designed to automatically track the reference frequency. If an interfering signal is attenuated by a filter before it reaches the lock-in input, the dynamic reserve of the lock-in will be increased by that amount. For the SR510 and SR530, a dynamic reserve increase of up to 20 dB can be realized using the input band pass filter. Of course, such filters add their own noise and contribute to phase error: so they should only be used if necessary.

A lock-in can measure signals as small as a few nanovolts. A low-noise signal amplifier is required to boost the signal to a level where the A/D converter can digitize the signal without degrading the signal-to-noise. The analog gain in the SR850 ranges from roughly 7 to 1000. As discussed previously, higher gains do not improve signal-to-noise and are not necessary.

The overall gain (AC and DC) is determined by the sensitivity. The distribution of the gain (AC versus DC) is set by the dynamic reserve.

Input Noise

The input noise of the SR810, SR830 or SR850 signal amplifier is about 5 nVrms/√Hz. The SR530 and SR510 lock-ins have 7 nVrms/√Hz of input noise. What does this noise figure mean? Let's set up an experiment. If an amplifier has 5 nVrms/√Hz of input noise and a gain of 1000, then the output will have 5 µVrms/√Hz of noise. Suppose the amplifier output is low-pass filtered with a single RC filter (6 dB/oct rolloff) with a time constant of 100 ms. What will be the noise at the filter output?

Amplifier input noise and Johnson noise of resistors are Gaussian in nature. That is, the amount of noise is proportional to the square root of the bandwidth in which the noise is measured. A single stage RC filter has an equivalent noise bandwidth (ENBW) of 1/4T, where T is the time constant (R × C). This means that Gaussian noise at the filter input is filtered with an effective bandwidth equal to the ENBW. In this example, the filter sees 5 µVrms/√Hz of noise at its input. It has an ENBW of 1/(4 × 100 ms) or 2.5 Hz. The voltage noise at the filter output will be 5 µVrms/√Hz × √2.5 Hz, or 7.9 µVrms. For Gaussian noise, the peak-to-peak noise is about 5 times the rms noise. Thus, the output will have about 40 µVpp of noise.

Input noise for a lock-in works the same way. For sensitivities below about 5 µV full scale, the input noise will determine the output noise (at minimum reserve). The amount of noise at the output is determined by the ENBW of the low pass filter. The ENBW depends upon the time constant and filter rolloff. For example, suppose the lock-in is set to 5 µV full scale, with a 100 ms time constant, and 6 dB/oct of filter rolloff. The lock-in

will measure the input noise with an ENBW of 2.5 Hz. This translates to 7.9 nVrms at the input. At the output, this represents about 0.16 % of full scale (7.9 nV/5 µV). The peak-to-peak noise will be about 0.8 % of full scale.

All of this assumes that the signal input is being driven from a low impedance source. Remember resistors have Johnson noise equal to $0.13 \times \sqrt{R}$ nVrms/√Hz. Even a 50 Ω resistor has almost 1 nVrms/√Hz of noise! A signal source impedance of 2 kΩ will have a Johnson noise greater than the lock-in's input noise. To determine the overall noise of multiple noise sources, take the square root of the sum of the squares of the individual noise figures. For example, if a 2 kΩ source impedance is used, the Johnson noise will be 5.8 nVrms/√Hz. The overall noise at the lock-in's input will be $[5^2 + 5.8^2]^{½}$, or 7.7 nVrms/√Hz.

Noise Sources

What is the origin of the noise we've been discussing? There are two types of noise we have to worry about in laboratory situations: intrinsic noise and external noise. Intrinsic noise sources, like Johnson noise and shot noise, are inherent to all physical processes. Though we cannot get rid of intrinsic noise sources, by being aware of their nature we can minimize their effects. External noise sources are found in the environment—such as power line noise and broadcast stations. The effect of these noises sources can be minimized by careful attention to grounding, shielding, and other aspects of experimental design. We will first discuss some of the sources of intrinsic noise.

Johnson Noise

Every resistor generates a noise voltage across its terminals due to thermal fluctuations in the electron density within the resistor itself. These fluctuations give rise to an open-circuit noise voltage:

$$V_{noise}(rms) = (4k\,T\,R\,\Delta f)^{1/2}$$

where k=Boltzmann's constant (1.38×10^{-23} J/°K), T is the temperature in Kelvin (typically 300 °K), R is the resistance in ohms, and Δf is the bandwidth of the measurement in Hz.

Since the input signal amplifier in a lock-in typically has a bandwidth of approximately 300 kHz, the effective noise at the amplifier input is V_{noise}=70√R nVrms, or 350√R nVpp. This noise is broadband. So if the source impedance is large, it can determine the amount of dynamic reserve required.

The amount of noise measured by the lock-in is determined by the measurement bandwidth. Remember, the lock-in does not narrow its detection bandwidth until after the phase sensitive detectors. In a lock-in, the equivalent noise bandwidth (ENBW) of the low pass filter (time constant) sets the detection bandwidth. In this case, the measured noise of a resistor at the lock-in input, typically the source impedance of the signal, is simply:

$$V_{noise}(rms) = 0.13\sqrt{R}\sqrt{ENBW}\ nV$$

Shot Noise

Electric current has noise due to the finite nature of the charge carriers. There is always some non-uniformity in the electron flow which generates noise in the current. This noise is called "shot noise". This can appear as voltage noise when current is passed through a resistor, or as noise in a current measurement. The shot noise, or current noise, is given by:

$$I_{noise}(rms) = (2qI\,\Delta f)^{1/2}$$

where q is the electron charge (1.6×10^{-19} Coulomb), I is the rms AC current or DC current depending upon the circuit, and Δf is the bandwidth.

When the current input of a lock-in is used to measure an AC signal current, the bandwidth is typically so small that shot noise is not important.

1/f Noise

Every 10 Ω resistor, no matter what it is made of, has the same Johnson noise. However, there is excess noise in addition to Johnson noise which arises from fluctuations in resistance due to the current flowing through the resistor. For carbon composition resistors, this is typically 0.1 µV to 3 µV of rms noise per volt applied across the resistor. Metal film and wire-wound resistors have about 10 times less noise. This noise has a 1/f spectrum and makes measurements at low frequencies more difficult. Other sources of 1/f noise include noise found in vacuum tubes and semiconductors.

Total Noise

All of these noise sources are incoherent. The total random noise is the square root of the sum of the squares of all the incoherent noise sources.

External Noise Sources

In addition to the intrinsic noise sources discussed previously, there are a variety of external noise sources within the laboratory. Most of these noise sources are asynchronous, i.e. they are not related to the reference, and do not occur at the reference frequency or its harmonics. Examples include lighting fixtures, motors, cooling units, radios, computer screens, etc. These noise sources affect the measurement by increasing the required dynamic reserve or lengthening the time constant.

Some noise sources, however, are related to the reference, and if picked up in the signal, will add or subtract from the actual signal and cause errors in the measurement. Typical sources of synchronous noise are ground loops between the experiment, detector and lock-in; and electronic pick up from the reference oscillator or experimental apparatus.

Many of these noise sources can be minimized with good laboratory practice and experiment design. There are several ways in which noise sources are coupled into the signal path.

Capacitive Coupling

An AC voltage from a nearby piece of apparatus can couple to a detector via stray capacitance. Although C_{stray} may be very small, the coupled noise may still be larger than a weak experimental signal. This is especially damaging if the coupled noise is synchronous (at the reference frequency).

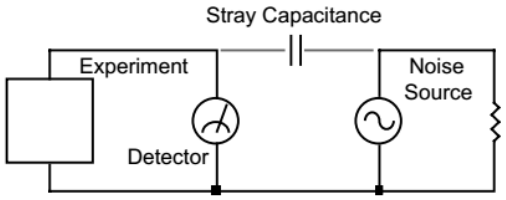

We can estimate the noise current caused by a stray capacitance by:

$$i = C_{stray}\frac{dV}{dt} = \omega C_{stray} V_{noise}$$

where ω is 2π times the noise frequency, V_{noise} is the noise amplitude, and C_{stray} is the stray capacitance.

For example, if the noise source is a power circuit, then f = 60 Hz and V_{noise} = 120 V. C_{stray} can be estimated using a parallel plate equivalent capacitor. If the capacitance is roughly an area of 1 cm^2 separated by 10 cm, then C_{stray} is 0.009 pF. The resulting noise current will be 400 pA (at 60 Hz). This small noise current can be thousands of times larger than the signal current. If the noise source is at a higher frequency, the coupled noise will be even greater.

If the noise source is at the reference frequency, the problem is much worse. The lock-in rejects noise at other frequencies, but pick-up at the reference frequency appears as signal!

Cures for capacitive noise coupling include:

1) Removing or turning off the noise source.

2) Keeping the noise source far from the experiment (reducing C_{stray}). Do not bring the signal cables close to the noise source.

3) Designing the experiment to measure voltages with low impedance (noise current generates very little voltage).

4) Installing capacitive shielding by placing both the experiment and detector in a metal box.

Inductive Coupling

An AC current in a nearby piece of apparatus can couple to the experiment via a magnetic field. A changing current in a nearby circuit gives rise to a changing magnetic field which induces an emf ($d\Phi_B/dt$) in the loop connecting the detector to the experiment. This is like a transformer with the experiment-detector loop as the secondary winding.

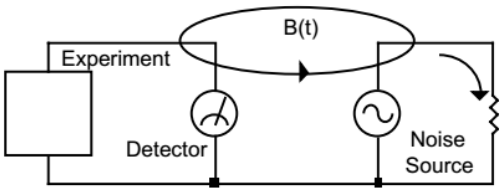

Cures for inductively coupled noise include:

1) Removing or turning off the interfering noise source.

2) Reduce the area of the pick-up loop by using twisted pairs or coaxial cables, or even twisting the two coaxial cables used in differential connections.

3) Using magnetic shielding to prevent the magnetic field from crossing the area of the experiment.

4) Measuring currents (not voltages) from high-impedance detectors.

Resistive Coupling or Ground Loops

Currents flowing through the ground connections can give rise to noise voltages. This is especially a problem with reference frequency ground currents.

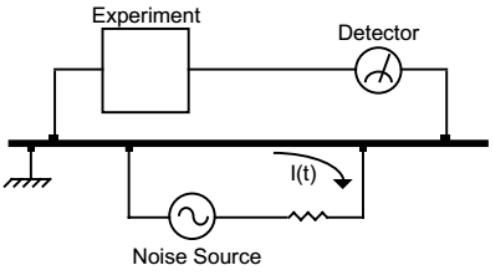

In this illustration, the detector is measuring the signal relative to a ground far from the rest of the experiment. The experiment senses the detector signal as well as the voltage from the noise source's ground return current, which passes through the finite resistance of the ground between the experiment and the detector. The detector and the experiment are grounded at different places which, in this case, are at different potentials.

Cures for ground loop problems include:

1) Grounding everything to the same physical point.

2) Using a heavy ground bus to reduce the resistance of ground connections.

3) Removing sources of large ground currents from the ground bus used for small signals.

Microphonics

Not all sources of noise are electrical in origin. Mechanical noise can be translated into electrical noise by microphonic effects. Physical changes in the experiment or cables (due to vibrations for example) can result in electrical noise over the entire frequency range of the lock-in.

For example, consider a coaxial cable connecting a detector to a lock-in. The capacitance of the cable is a function of its geometry. Mechanical vibrations in the cable translate into a capacitance that varies in time—typically at the vibration frequency. Since the cable is governed by Q=CV, taking the derivative yields:

$$C\frac{dV}{dt} + V\frac{dC}{dt} = \frac{dQ}{dt} = i$$

Mechanical vibrations in the cable which cause a dC/dt will give rise to a current in the cable. This current affects the detector and the measured signal.

Some ways to minimize microphonic signals are:

1) Eliminate mechanical vibrations near the experiment.

2) Tie down cables carrying sensitive signals so they do not move.

3) Use a low noise cable that is designed to reduce microphonic effects.

Thermocouple Effects

The emf created by junctions between dissimilar metals can give rise to many microvolts of slowly varying potentials. This source of noise is typically at very low frequency since the temperature of the detector and experiment generally changes slowly. This effect is large on the scale of many detector outputs, and can be a problem for low frequency measurements: especially in the mHz range. Some ways to minimize thermocouple effects are:

1) Hold the temperature of the experiment or detector constant.

2) Use a compensation junction, i.e. a second junction in reverse polarity which generates an emf to cancel the thermal potential of the first junction. This second junction should be held at the same temperature as the first junction.

Input Connections

In order to achieve the best accuracy for a given measurement, care must be taken to minimize the various noise sources which can be found in the laboratory. With intrinsic noise (Johnson noise, 1/f noise or input noise), the experiment or detector must be designed with these noise sources in mind. These noise sources are present regardless of the input connections. The effect of noise sources in the laboratory (such as motors, signal generators, etc.), and the problem of differential grounds between the detector and the lock-in, can be minimized by careful input connections.

There are two basic methods for connecting a voltage signal to the lock-in amplifier; the single-ended connection is more convenient while the differential connection eliminates spurious pick-up more effectively.

Single-Ended Voltage Connection (A)

In the first method, the lock-in uses the A input in a single-ended mode. The lock-in detects the signal as the voltage between the center and outer conductors of the A input only. The lock-in does not force the shield of the A cable to ground. Rather, it is internally connected to the lock-in's ground via a resistor. The value of this resistor is typically between 10 Ω and 1 kΩ. The SR810, SR830 and SR850 let you choose the value of this resistor. This avoids ground loop problems between the experiment and the lock-in due to differing ground potentials. The lock-in lets the shield 'quasi-float' in order to sense the experiment ground. However, noise pickup on the shield will appear as noise to the lock-in. This is bad since the lock-in cannot reject this noise. Common mode noise, which appears on both the center and shield, is rejected by the 100 dB CMRR of the lock-in input, but noise on only the shield is not rejected at all.

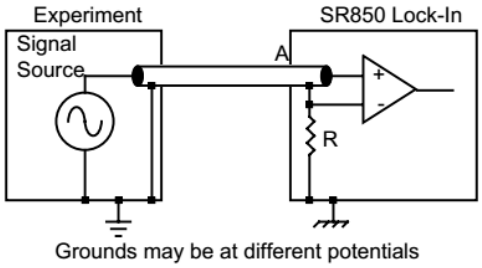

Differential Voltage Connection (A–B)

The second method of connection is the differential mode. The lock-in measures the voltage difference between the center conductors of the A and B inputs. Both of the signal connections are shielded from spurious pick-up. Noise pickup on the shields does not translate into signal noise since the shields are ignored.

When using two cables, it is important that both cables travel the same path between the experiment and the lock-in. Specifically, there should not be a large loop area enclosed by

the two cables. Large loop areas are susceptible to magnetic pickup.

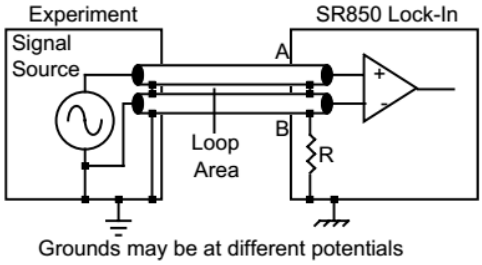

Common Mode Signals

Common mode signals are those signals which appear equally on both center and shield (A) or both A and B (A–B). With either connection scheme, it is important to minimize both the common mode noise and the common mode signal. Notice that the signal source is held near ground potential in both illustrations above. If the signal source floats at a nonzero potential, the signal which appears on both the A and B inputs will not be perfectly cancelled. The common mode rejection ratio (CMRR) specifies the degree of cancellation. For low frequencies, the CMRR of 100 dB indicates that the common mode signal is canceled to 1 part in 10^5. Even with a CMRR of 100 dB, a 100 mV common mode signal behaves like a 1 µV differential signal! This is especially bad if the common mode signal is at the reference frequency (this happens a lot due to ground loops). The CMRR decreases by about 6 dB/oct (20 dB/decade) starting at around 1 kHz.

The Lock-In as a Noise Measurement Device

Lock-in amplifiers can be used to measure noise. Noise measurements are generally used to characterize components and detectors. Remember that the lock-in detects signals close to the reference frequency. How close? Input signals within the detection bandwidth set by the low-pass-filter time constant and rolloff appear at the output at a frequency $f = f_{sig} - f_{ref}$. Input noise near f_{ref} appears as noise at the output with a bandwidth of DC to the detection bandwidth.

The noise is simply the standard deviation (root of the mean of the squared deviations) of the measured X, Y or R. You can measure this noise exactly by recording a sequence of output values and then calculating the standard deviation directly. The noise, in volts/√Hz, is simply the standard deviation divided by the square root of the equivalent noise bandwidth of the time constant.

For Gaussian noise, the equivalent noise bandwidth (ENBW) of a low pass filter is the bandwidth of the perfect rectangular filter which passes the same amount of noise as the real filter.

Noise Estimation

The above technique, while mathematically sound, can not provide a real-time output or an analog output proportional to the measured noise. Lock-ins (such as the SR510, SR530, SR810, SR830 and SR850) do provide these features, however. The quantity X_{noise} is computed from the measured values of X using the following algorithm. The moving average of X is computed. This is the mean value of X over some past history. The present mean value of X is subtracted from the present value of X to find the deviation of X from the mean. Finally, the moving average of the absolute value of the deviations is calculated. This calculation is called the mean average deviation, or MAD. This is not the same as an rms calculation. However, if the noise is Gaussian in nature, the rms noise and the MAD noise are related by a constant factor.

SRS lock-in amplifiers use the MAD method to estimate the rms noise quantities Xn, Yn and Rn. The advantage of this technique is its numerical simplicity and speed. For most applications, noise estimation and standard deviation calculations yield the same answer. Which method you use depends upon the requirements of the experiment.

A.11. Specification of the used translation stages

http://www.thorlabs.com/newgrouppage9.cfm?objectgroup_id=2131

Item #	NRT100(/M)
Translation	
Travel Range	100 mm (3.9")
Bidirectional Repeatability[a]	1 µm
Backlash[b]	<3 µm
Maximum Velocity[c]	30 mm/s
Velocity Stability	±0.1 mm/s
Maximum Acceleration[c]	30 mm/s^2
Minimum Achievable Incremental Movement[d]	0.10 µm
Minimum Repeatable Incremental Movement[e]	2 µm
Accuracy	
Calibrated Absolute On-Axis Accuracy	2.0 µm (Typical) 5.0 µm (Max)
Absolute On-Axis Accuracy[f]	15.29 µm
Maximum Percentage Accuracy[g]	0.09%
Home Location Accuracy	±0.6 µm
Pitch	<0.008° (140 µrad)
Yaw	<0.05° (873 µrad)
Load Capacity	
Horizontal Load Capacity	<12 kg (26 lbs) (Recommended) 20 kg (44 lbs) (Max)
Vertical Load Capacity	<4 kg (9 lbs) (Recommended) 5 kg (11 lbs) (Max)
General	
Weight	2.2 kg (4.9 lbs)
Dimensions	362.7 mm x 100.0 mm x 43.5 mm (14.28" x 3.94" x 1.71")

a. The average of the repeatability when a set position is approached from both directions.
b. When a stage is moved to a position and then returned to its original position, some motion is lost due to the lead screw mechanism. This loss is known as backlash.
c. Measured Using Thorlabs Benchtop Stepper Motor Controllers.
d. The measured minimum incremental motion that the stage can achieve, also referred to as the minimum step size.
e. The minimum incremental motion that the stage can repeatedly achieve within its standard error.
f. Accuracy when calibration files are not used. Calibration files are measured at the factory and come with each stage.
g. This is the maximum discrepancy between commanded position and absolute position expressed as a percentage of the commanded position.

References

1. Kerecman, A.J., *Real time millimeter wave imaging.* Soc of Photo-opt Instrum Eng Semin Proc, 1973. **32**: p. 69-73.
2. Fleming, J.W., *Precise submillimeter-wave spectrometry of gases.* IEEE Transactions on Instrumentation and Measurement, 1976. **IM-25**(4): p. 286-289.
3. Auston, D.H., *Subpicosecond electro-optic shock waves.* Applied Physics Letters, 1983. **43**(8): p. 713-715.
4. Smith, P.R., D.H. Auston, and M.C. Nuss, *Subpicosecond photoconducting depole antennas.* IEEE Journal of Quantum Electronics, 1988. **24**(2): p. 255-260.
5. Auston, D.H., *Picosecond optoelectronic switching and gating in silicon.* Applied Physics Letters, 1975. **26**(3): p. 101-103.
6. Chen, J., et al., *Absorption coefficients of selected explosives and related compounds in the range of 0.1-2.8 THz.* Optics Express, 2007. **15**(19): p. 12060-12067.
7. Chen, Y., et al., *THz spectroscopic investigation of 2,4-dinitrotoluene.* Chemical Physics Letters, 2004. **400**(4–6): p. 357-361.
8. Dorney, T.D., R.G. Baraniuk, and D.M. Mittleman, *Material parameter estimation with terahertz time-domain spectroscopy.* Journal of the Optical Society of America A, 2001. **18**(7): p. 1562-1571.
9. Hu, B.B. and M.C. Nuss, *Imaging with terahertz waves.* Optics Letters, 1995. **20**(16): p. 1716-1718.
10. Mittleman, D.M., R.H. Jacobsen, and M.C. Nuss, *T-ray imaging.* IEEE Journal on Selected Topics in Quantum Electronics, 1996. **2**(3): p. 679-692.
11. Arbab, M.H., et al. *Characterization of burn injuries using terahertz time-domain spectroscopy*. 2011.
12. Löffler, T., et al., *Visualization and classification in biomedical terahertz pulsed imaging.* Physics in Medicine and Biology, 2002. **47**(21): p. 3847-3852.
13. Reid, C.B., et al., *Terahertz Time-Domain Spectroscopy of Human Blood.* Biomedical and Health Informatics, IEEE Journal of, 2013. **17**(4): p. 774-778.
14. Krishnamurthy, S., et al., *Characterization of thin polymer films using terahertz time-domain interferometry.* Applied Physics Letters, 2001. **79**(6): p. 875-877.
15. Peier, P., et al., *Imaging of THz waves in 2D photonic crystal structures embedded in a slab waveguide.* New Journal of Physics. **12**.
16. Muller, E.R., http://www.coherent.com/downloads/opticallypumpedlaser.pdf, Optically-pumped THz laser technology
17. Kawase, K., et al., *Coherent tunable THz-wave generation from LiNbO3 with monolithic grating coupler.* Applied Physics Letters, 1996. **68**(18): p. 2483-2485.
18. Kawase, K., et al., *Characteristics of THz-wave radiation using a monolithic grating coupler on a LiNbO3 crystal.* International Journal of Infrared and Millimeter Waves, 1996. **17**(11): p. 1839-1849.
19. Edwards, T.J., et al., *Compact source of continuously and widely-tunable terahertz radiation.* Optics Express, 2006. **14**(4): p. 1582-1589.
20. Kawase, K., et al., *Terahertz Rays to Detect Drugs of Abuse*, in *Terahertz Frequency Detection and Identification of Materials and Objects*, R. Miles, et al., Editors. 2007, Springer Netherlands. p. 241-250.
21. Kawase, K., et al., *Non-destructive terahertz imaging of illicit drugs using spectral fingerprints.* Optics Express, 2003. **11**(20): p. 2549-2554.
22. Kodo, K., et al., *Terahertz parametric sources and imaging applications.* Semiconductor Science and Technology, 2005. **20**(7): p. S258.

23. Watanabe, Y., et al., *Component spatial pattern analysis of chemicals using terahertz spectroscopic imaging.* Applied Physics Letters, 2003. **83**(4): p. 800-802.
24. Gallerano, G. and S. Biedron. *Overview of terahertz radiation sources*. in *Proceedings of the 2004 FEL Conference*. 2004.
25. Eisele, H. and G.I. Haddad, *Two-terminal millimeter-wave sources.* IEEE Transactions on Microwave Theory and Techniques, 1998. **46**(6): p. 739-746.
26. Maiwald, F., et al. *THz frequency multiplier chains based on planar Schottky diodes*. in *Proceedings of SPIE - The International Society for Optical Engineering*. 2002.
27. Maestrini, A., et al., *A 1.7-1.9 THz local oscillator source.* IEEE Microwave and Wireless Components Letters, 2004. **14**(6): p. 253-255.
28. Maestrini, A., et al., *Design and characterization of a room temperature all-solid-state electronic source tunable from 2.48 to 2.75 THz.* IEEE Transactions on Terahertz Science and Technology, 2012. **2**(2): p. 177-185.
29. Ward, J., et al. *Capability of THz sources based on Schottky diode frequency multiplier chains*. in *Microwave Symposium Digest, 2004 IEEE MTT-S International*. 2004.
30. Heimbeck, M.S., et al., *Terahertz digital holography using angular spectrum and dual wavelength reconstruction methods.* Optics Express, 2011. **19**(10): p. 9192-9200.
31. Földesy, P., *Terahertz single-shot quadrature phase-shifting interferometry.* Optics Letters, 2012. **37**(19): p. 4044-4046.
32. Koch, M., *The search continues for efficient terahertz sources.* Laser Focus World, 1 November 2005.
33. Chaschina, O.I., et al., *Real-time speckle metrology using terahertz free electron laser radiation.* Nuclear Instruments and Methods in Physics Research Section A: Accelerators, Spectrometers, Detectors and Associated Equipment, 2009. **603**(1–2): p. 50-51.
34. Ferguson, B. and X.C. Zhang, *Materials for terahertz science and technology.* Nature Materials, 2002. **1**(1): p. 26-33.
35. Dragoman, D. and M. Dragoman, *Terahertz fields and applications.* Progress in Quantum Electronics, 2004. **28**(1).
36. Siegel, P.H., *Terahertz technology in biology and medicine.* IEEE Transactions on Microwave Theory and Techniques, 2004. **52**(10): p. 2438-2447.
37. Siegel, P.H., *Terahertz technology.* IEEE Transactions on Microwave Theory and Techniques, 2002. **50**(3): p. 910-928.
38. Abo-Bakr, M., et al., *Brilliant, coherent far-infrared (THz) synchrotron radiation.* Physical Review Letters, 2003. **90**(9): p. 094801/1-094801/4.
39. Wang, F., et al., *Coherent THz synchrotron radiation from a storage ring with high-frequency RF system.* Physical Review Letters, 2006. **96**(6).
40. Williams, G.P., et al., *High-power terahertz synchrotron sources.* Philosophical Transactions of the Royal Society A: Mathematical, Physical and Engineering Sciences, 2004. **362**(1815): p. 403-414.
41. Knyazev, B.A., G.N. Kulipanov, and N.A. Vinokurov, *Novosibirsk terahertz free electron laser: Instrumentation development and experimental achievements.* Measurement Science and Technology, 2010. **21**(5).
42. Dayton, J.A., et al., *Submillimeter backward wave oscillators.* International Journal of Infrared and Millimeter Waves, 1987. **8**(10): p. 1257-1268.
43. Ives, L., et al. *Development of Backward Wave Oscillators for Terahertz Applications*. in *Proceedings of SPIE - The International Society for Optical Engineering*. 2003.
44. Alekseev, E. and D. Pavlidis, *GaN Gunn diodes for THz signal generation.* IEEE MTT-S International Microwave Symposium Digest, 2000. **3**: p. 1905-1908.
45. Mukherjee, M., et al., *GaN IMPATT diode: A photo-sensitive high power terahertz source.* Semiconductor Science and Technology, 2007. **22**(12): p. 1258-1267.
46. Sollner, T.C.L.G., et al., *Resonant tunneling through quantum wells at frequencies up to 2.5 THz.* Applied Physics Letters, 1983. **43**(6): p. 588-590.

47. Brown, E.R., et al., *Oscillations up to 712 GHz in InAs/AlSb resonant-tunneling diodes.* Applied Physics Letters, 1991. **58**(20): p. 2291-2293.
48. Vodopyanov, K., *Terahertz technologies and applications.* Stanford course in Electrical Engineering, 2008.
49. Huei, W., et al., *Power-amplifier modules covering 70-113 GHz using MMICs.* Microwave Theory and Techniques, IEEE Transactions on, 2001. **49**(1): p. 9-16.
50. Maestrini, A., et al. *A 2.5-2.7 THz room temperature electronic source*. in *22nd International Symposium on Space Terahertz Technology 2011, ISSTT 2011*. 2011.
51. Chattopadhyay, G., et al., *An all-solid-state broad-band frequency multiplier chain at 1500 GHz.* IEEE Transactions on Microwave Theory and Techniques, 2004. **52**(5): p. 1538-1547.
52. Louhi, J.T., A.V. Raeisaenen, and N.R. Erickson, *Cooled Schottky varactor frequency multipliers at submillimeter wavelengths.* IEEE Transactions on Microwave Theory and Techniques, 1993. **41**(4): p. 565-571.
53. Mueller, E.R., *Submillimeter wave lasers*, in *Wiley encyclopedia of Electrical and Electronics Engineering*. 1999, Wiley: New York. p. 597-615.
54. Kawase, K., et al., *Arrayed silicon prism coupler for a terahertz-wave parametric oscillator.* Applied Optics, 2001. **40**(9): p. 1423-1426.
55. Kawase, K., et al. *Injection seeded THz-wave parametric generator (TPG) with wide tunability*. in *Pacific Rim Conference on Lasers and Electro-Optics, CLEO - Technical Digest*. 2001.
56. Kawase, K., et al., *Injection-seeded terahertz-wave parametric generator with wide tunability.* Applied Physics Letters, 2002. **80**(2): p. 195-197.
57. Kawase, K., J.I. Shikata, and H. Ito, *Terahertz wave parametric source.* Journal of Physics D: Applied Physics, 2002. **35**(3): p. R1-R14.
58. Stothard, D.J.M., et al., *Line-narrowed, compact, and coherent source of widely tunable terahertz radiation.* Applied Physics Letters, 2008. **92**(14).
59. Walsh, D., et al., *Injection-seeded intracavity terahertz optical parametric oscillator.* Journal of the Optical Society of America B: Optical Physics, 2009. **26**(6): p. 1196-1202.
60. Auston, D.H., A.M. Glass, and A.A. Ballman, *Optical rectification by impurities in polar crystals.* Physical Review Letters, 1972. **28**(14): p. 897-900.
61. Auston, D.H. and A.M. Glass, *Optical generation of intense picosecond electrical pulses.* Applied Physics Letters, 1972. **20**(10): p. 398-399.
62. Kleinman, D.A. and D.H. Auston, *Theory of electrooptic shock radiation in nonlinear opical media.* IEEE Journal of Quantum Electronics, 1984. **QE-20**(8): p. 964-970.
63. Auston, D.H., K.P. Cheung, and P.R. Smith, *Picosecond photoconducting Hertzian dipoles.* Applied Physics Letters, 1984. **45**(3): p. 284-286.
64. Hu, B.B., et al., *Optically steerable photoconducting antennas.* Applied Physics Letters, 1990. **56**(10): p. 886-888.
65. Siegel, P.H., *Terahertz pioneer: David H. Auston.* IEEE Transactions on Terahertz Science and Technology, 2011. **1**(1): p. 6-8.
66. Bass, M., et al., *Optical rectification.* Physical Review Letters, 1962. **9**(11): p. 446-448.
67. Auston, D.H. and M.C. Nuss, *Electrooptic generation and detection of femtosecond electrical transients.* IEEE Journal of Quantum Electronics, 1988. **24**(2): p. 184-197.
68. Morris, J.R. and Y.R. Shen, *Far-infrared generation by picosecond pulses in electro-optical materials.* Optics Communications, 1971. **3**(2): p. 81-84.
69. Siegel, P.H., *Terahertz pioneers: A series of interviews with significant contributors to terahertz science and technology.* IEEE Transactions on Terahertz Science and Technology, 2015. **5**(1): p. 6.
70. Siegel, P.H., *Terahertz pioneer: Michael bass "the THz light at the end of the tunnel".* IEEE Transactions on Terahertz Science and Technology, 2014. **4**(4): p. 410-417.

71. Duvillaret, L., F. Garet, and J.L. Coutaz, *A reliable method for extraction of material parameters in terahertz time-domain spectroscopy.* IEEE Journal on Selected Topics in Quantum Electronics, 1996. **2**(3): p. 739-745.
72. Faist, J., et al., *Quantum cascade laser.* Science, 1994. **264**(5158): p. 553-556.
73. Williams, B.S., *Terahertz quantum-cascade lasers.* Nat Photon, 2007. **1**(9): p. 517-525.
74. Shore, K.A., *Quantum Cascade Lasers, by Jérôme Faist.* Contemporary Physics, 2013. **54**(6): p. 301-302.
75. Kohler, R., et al., *Terahertz semiconductor-heterostructure laser.* Nature, 2002. **417**(6885): p. 156-159.
76. Lee, A.W.M., et al., *Real-time terahertz imaging over a standoff distance (>25meters).* Applied Physics Letters, 2006. **89**(14): p. 141125.
77. Scalari, G., et al., *Electrically switchable, two-color quantum cascade laser emitting at 1.39 and 2.3THz.* Applied Physics Letters, 2006. **88**(14): p. 141102.
78. Williams, B., et al., *Operation of terahertz quantum-cascade lasers at 164 K in pulsed mode and at 117 K in continuous-wave mode.* Optics Express, 2005. **13**(9): p. 3331-3339.
79. Tonouchi, M., *Cutting-edge terahertz technology.* Nature Photonics, 2007. **1**(2): p. 97-105.
80. Auston, D.H., et al., *An amorphous silicon photodetector for picosecond pulses.* Applied Physics Letters, 1980. **36**(1): p. 66-68.
81. Valdmanis, J.A., G. Mourou, and C.W. Gabel, *Picosecond electro-optic sampling system.* Applied Physics Letters, 1982. **41**(3): p. 211-212.
82. Valdmanis, J., G.A. Mourou, and C.W. Gabel, *Subpicosecond electrical sampling.* Quantum Electronics, IEEE Journal of, 1983. **19**(4): p. 664-667.
83. Wu, Q. and X.C. Zhang, *Free-space electro-optic sampling of terahertz beams.* Applied Physics Letters, 1995. **67**(24): p. 3523-3525.
84. Wu, Q. and X.C. Zhang, *Ultrafast electro-optic field sensors.* Applied Physics Letters, 1996. **68**(12): p. 1604-1606.
85. Hubers, H.W., *Terahertz Heterodyne Receivers.* Selected Topics in Quantum Electronics, IEEE Journal of, 2008. **14**(2): p. 378-391.
86. Siegel, P. and R. Dengler, *Terahertz heterodyne imaging Part I: Introduction and techniques.* International Journal of Infrared and Millimeter Waves, 2006. **27**(4): p. 465-480.
87. Siegel, P. and R. Dengler, *Terahertz Heterodyne Imaging Part II: Instruments.* International Journal of Infrared and Millimeter Waves, 2006. **27**(5): p. 631-655.
88. Llombart, N., et al. *THZ Heterodyne Imaging Applicatiions, Instruments and Directions*. in *Microwave Conference, 2008. EuMC 2008. 38th European*. 2008.
89. For example Gentect electro-optics from Canada, Q.U., or recently pyrosensor.de from Germany, as well the suppliers Edinburgh Instruments, Microtech instruments, laser2000 etc... .
90. Huang, F., et al., *Terahertz study of 1,3,5-trinitro-s-triazine by time-domain and Fourier transform infrared spectroscopy.* Applied Physics Letters, 2004. **85**(23): p. 5535-5537.
91. Ning, L., et al., *Study on the THz spectrum of methamphetamine.* Optics Express, 2005. **13**(18): p. 6750-6755.
92. Walther, M., et al., *Far-infrared vibrational spectra of all-trans, 9-cis and 13-cis retinal measured by THz time-domain spectroscopy.* Chemical Physics Letters, 2000. **332**(3–4): p. 389-395.
93. Korter, T.M., et al., *Terahertz spectroscopy of solid serine and cysteine.* Chemical Physics Letters, 2006. **418**(1–3): p. 65-70.
94. Watanabe, Y., et al., *Component analysis of chemical mixtures using terahertz spectroscopic imaging.* Optics Communications, 2004. **234**(1–6): p. 125-129.
95. Hunsche, S., et al., *THz near-field imaging.* Optics Communications, 1998. **150**(1–6): p. 22-26.

96. Awad, M.M. and R.A. Cheville, *Transmission terahertz waveguide-based imaging below the diffraction limit.* Applied Physics Letters, 2005. **86**(22): p. 221107.
97. Serita, K., et al., *Scanning laser terahertz near-field imaging system.* Optics Express, 2012. **20**(12): p. 12959-12965.
98. Blanchard, F., et al., *Real-time terahertz near-field microscope.* Optics Express, 2011. **19**(9): p. 8277-8284.
99. Macfaden, A.J., et al., *3 μm aperture probes for near-field terahertz transmission microscopy.* Applied Physics Letters, 2014. **104**(1): p. 011110.
100. John, F.F., et al., *Terahertz near-field imaging.* Physics in Medicine and Biology, 2002. **47**(21): p. 3727.
101. Chen, H.-T., R. Kersting, and G.C. Cho, *Terahertz imaging with nanometer resolution.* Applied Physics Letters, 2003. **83**(15): p. 3009-3011.
102. Wai Lam, C., D. Jason, and M.M. Daniel, *Imaging with terahertz radiation.* Reports on Progress in Physics, 2007. **70**(8): p. 1325.
103. Takayanagi, J., et al., *High-resolution time-of-flight terahertz tomography using a femtosecond fiber laser.* Optics Express, 2009. **17**(9): p. 7533-7539.
104. Yasuda, T., et al., *Real-time two-dimensional terahertz tomography of moving objects.* Optics Communications, 2006. **267**(1): p. 128-136.
105. Recur, B., et al., *Investigation on reconstruction methods applied to 3D terahertz computed tomography.* Optics Express, 2011. **19**(6): p. 5105-5117.
106. Brahm, A., et al., *Volumetric spectral analysis of materials using terahertz-tomography techniques.* Applied Physics B, 2010. **100**(1): p. 151-158.
107. Quast, H. and T. Loffler. *3D-terahertz-tomography for material inspection and security*. in *Infrared, Millimeter, and Terahertz Waves, 2009. IRMMW-THz 2009. 34th International Conference on*. 2009.
108. Wang, S. and X.C. Zhang, *Pulsed terahertz tomography.* Journal of Physics D: Applied Physics, 2004. **37**(4): p. R1.
109. Robert, B., *Terahertz imaging: a report on progress.* Sensor Review, 2009. **29**(1): p. 6-12.
110. Zhang, L., et al., *Terahertz multiwavelength phase imaging without 2? ambiguity.* Optics Letters, 2006. **31**(24): p. 3668-3670.
111. Duvillaret, L., F. Garet, and J.-L. Coutaz, *Highly precise determination of optical constants and sample thickness in terahertz time-domain spectroscopy.* Applied Optics, 1999. **38**(2): p. 409-415.
112. Duvillaret, L., F. Garet, and J.L. Coutaz, *A reliable method for extraction of material parameters in terahertz time-domain spectroscopy.* Selected Topics in Quantum Electronics, IEEE Journal of, 1996. **2**(3): p. 739-746.
113. Groves, R.M., et al., *2D and 3D non-destructive evaluation of a wooden panel painting using shearography and terahertz imaging.* NDT & E International, 2009. **42**(6): p. 543-549.
114. Ocket, I., et al. *Characterization of speckle/despeckling in active millimeter wave imaging systems using a first order 1.5D model*. 2006.
115. Jaeger, I., et al., *Comparison of speckle reduction diversity tools for active millimeter-wave imaging.* Journal of the Optical Society of America A, 2008. **25**(7): p. 1716-1721.
116. Nikolai, A.V., et al., *Speckle pattern of the images of objects exposed to monochromatic coherent terahertz radiation.* Quantum Electronics, 2009. **39**(5): p. 481.
117. Chen, J.C. and S. Kaushik, *Terahertz Interferometer That Senses Vibrations Behind Barriers.* Photonics Technology Letters, IEEE, 2007. **19**(7): p. 486-488.
118. Buersgens, F., G. Acuna, and R. Kersting, *Acoustic phase imaging with terahertz radiation.* Optics Express, 2007. **15**(8): p. 4427-4434.
119. Buersgens, F., G. Acuna, and R. Kersting, *Millimeter wave probing of the acoustic phase for concealed object detection.* Optics Express, 2007. **15**(14): p. 8838-8843.

120. Wang, Y., et al., *Continuous-wave terahertz phase imaging using a far-infrared laser interferometer.* Applied Optics, 2011. **50**(35): p. 6452-6460.
121. Nguyen, T.D., J.D.R. Valera, and A.J. Moore, *Optical thickness measurement with multi-wavelength THz interferometry.* Optics and Lasers in Engineering, 2014. **61**: p. 19-22.
122. Wang, X., L. Hou, and Y. Zhang, *Continuous-wave terahertz interferometry with multiwavelength phase unwrapping.* Applied Optics, 2010. **49**(27): p. 5095-5102.
123. Mahon, R.J., J.A. Murphy, and W. Lanigan, *Digital holography at millimetre wavelengths.* Optics Communications, 2006. **260**(2): p. 469-473.
124. Mahon, R., A. Murphy, and W. Lanigan. *Terahertz holographic image reconstruction and analysis*. in *Conference Digest of the 2004 Joint 29th International Conference on Infrared and Millimeter Waves and 12th International Conference on Terahertz Electronics*. 2004.
125. Ulf, S. and P.O.J. Werner, *Digital recording and numerical reconstruction of holograms.* Measurement Science and Technology, 2002. **13**(9): p. R85.
126. Goodman, J.W., *Introduction to Fourier Optics*. 1996: McGraw-Hill.
127. Cherkassky, V.S., et al. *Terahertz imaging and holography with a high-power free electron laser*. in *The Joint 30th International Conference on Infrared and Millimeter Waves and 13th International Conference on Terahertz Electronics, 2005. IRMMW-THz 2005*. 2005.
128. Tamminen, A., J. Ala-Laurinaho, and A.V. Raisanen. *Indirect holographic imaging at 310 GHz*. in *Radar Conference, 2008. EuRAD 2008. European*. 2008.
129. Sun, W., X. Wang, and Y. Zhang, *Continuous wave terahertz phase imaging with three-step phase-shifting.* Optik, 2013. **124**(22): p. 5533-5536.
130. Gabor, D., *A new microscopic principle.* Nature, 1948. **161**(4098): p. 777-778.
131. Gabor, D., *Microscopy by reconstructed wave fronts: II.* Proceedings of the Physical Society. Section B, 1951. **64**(6): p. 449-469.
132. Leith, E.N. and J. Upatnieks, *Reconstructed Wavefronts and Communication Theory.* Journal of the Optical Society of America, 1962. **52**(10): p. 1123-1128.
133. Kreis, T., *Handbook of Holographic Interferometry: Optical and Digital Methods*. 2005: Wiley.
134. Skarman, B., J. Becker, and K. Wozniak, *Simultaneous 3D-PIV and temperature measurements using a new CCD-based holographic interferometer.* Flow Measurement and Instrumentation, 1996. **7**(1): p. 1-6.
135. Yamaguchi, I. and T. Zhang, *Phase-shifting digital holography.* Optics Letters, 1997. **22**(16): p. 1268-1270.
136. Zhang, T. and I. Yamaguchi, *Three-dimensional microscopy with phase-shifting digital holography.* Optics Letters, 1998. **23**(15): p. 1221-1223.
137. Yamaguchi, I., et al., *Image formation in phase-shifting digital holography and applications to microscopy.* Applied Optics, 2001. **40**(34): p. 6177-6186.
138. Yamaguchi, I., J.-i. Kato, and S. Ohta, *Surface Shape Measurement by Phase-Shifting Digital Holography.* Optical Review, 2001. **8**(2): p. 85-89.
139. Carré, P., *Installation et Utilisation du Comparateur Photoelectrique et Interferentiel du Bureau International des Poids de Mesures.* Metrologia, 1996. **2**(13).
140. Matysiak, M., *Optical techniques for non-destructive detection of flaws in ceramic components*, in *School of Engineering and Physical Sciences*. 2012, Heriot-Watt University: Heriot-Watt University.
141. White, J., et al., *Time-Domain Terahertz Mapping of Thickness and Degradation of Aircraft Turbine Blade Thermal Barrier Coatings*, in *2008 Conference on Lasers and Electro-Optics & Quantum Electronics and Laser Science Conference, Vols 1-9*. 2008. p. 1115-1116.
142. Fukuchi, T., et al., *Measurement of Topcoat Thickness of Thermal Barrier Coating for Gas Turbines Using Terahertz Waves.* Electrical Engineering in Japan, 2013. **183**(4): p. 1-9.

143. Watanabe, M., et al., *Electromagnetic properties of plasma sprayed thermal barrier coatings in terahertz range*, in *34th International Conference on Infrared, Millimeter, and Terahertz Waves,*. 2009, IEEE: Busan.
144. Inoue, S. and R. Oldenbourg, *Microscopes*, in *Handbook of Optics: Devices, Measurements and Properties*, M. Bass, Editor. 1995, McGraw-Hill.
145. *Stanford Research System application note, "About Lock-In Amplifier", http://www.thinksrs.com.*
146. Wiik, R., et al., *Continuous wave terahertz spectrometer as a noncontact thickness measuring device.* Applied Optics, 2008. **47**(16): p. 3023-3026.
147. Spickermann, G., et al., *High signal-to-noise-ratio electro-optical terahertz imaging system based on an optical demodulating detector array.* Optics Letters, 2009. **34**(21): p. 3424-3426.
148. Siegman, A.E., *Lasers.* University Science Books, 1986: p. 664–669. ISBN 0-935702-11-3.
149. Surrel, Y., *Additive noise effect in digital phase detection.* Applied Optics, 1997. **36**(1): p. 271-276.
150. Creath, K., *V Phase-Measurement Interferometry Techniques*, in *Progress in optics*. 1988. p. 349-393.
151. van Wingerden, J., H.J. Frankena, and C. Smorenburg, *Linear approximation for measurement errors in phase shifting interferometry.* Applied Optics, 1991. **30**(19): p. 2718-2729.
152. Creath, K. *Phase-shifting speckle interferometry*. in *29th Annual Technical Symposium*. 1985: International Society for Optics and Photonics.
153. Goldstein, R.M., H.A. Zebker, and C.L. Werner, *Satellite radar interferometry: Two-dimensional phase unwrapping.* Radio Science, 1988. **23**(4): p. 713-720.
154. Ghiglia, D.C. and M.D. Pritt, *Two-dimensional phase unwrapping: theory, algorithms, and software*. 1998: Wiley.
155. Mann, C.J., et al., *High-resolution quantitative phase-contrast microscopy by digital holography.* Optics Express, 2005. **13**(22): p. 8693-8698.
156. Verrier, N. and C. Fournier, *Digital holography super-resolution for accurate three-dimensional reconstruction of particle holograms.* Optics Letters, 2015. **40**(2): p. 217-220.
157. Osten, W., et al., *Recent advances in digital holography Invited.* Applied Optics, 2014. **53**(27): p. G44-G63.
158. Xu, L., et al., *Studies of digital microscopic holography with applications to microstructure testing.* Applied Optics, 2001. **40**(28): p. 5046-5051.
159. Schnars, U., *Direct phase determination in hologram interferometry with use of digitally recorded holograms.* Journal of the Optical Society of America a-Optics Image Science and Vision, 1994. **11**(7): p. 2011-2015.
160. Pedrini, G. and H.J. Tiziani, *Quantitative evaluation of two-dimensional dynamic deformations using digital holography.* Optics and Laser Technology, 1997. **29**(5): p. 249-256.
161. Picart, P., et al., *2D full field vibration analysis with multiplexed digital holograms.* Optics Express, 2005. **13**(22): p. 8882-8892.
162. Picart, P., et al., *Some opportunities for vibration analysis with time averaging in digital Fresnel holography.* Applied Optics, 2005. **44**(3): p. 337-343.
163. Kemper, B. and G. von Bally, *Digital holographic microscopy for live cell applications and technical inspection.* Applied Optics, 2008. **47**(4): p. A52-A61.
164. Kim, M.K., *Tomographic three-dimensional imaging of a biological specimen using wavelength-scanning digital interference holography.* Optics Express, 2000. **7**(9): p. 305-310.
165. Popescu, G., et al., *Fourier phase microscopy for investigation of biological structures and dynamics.* Optics Letters, 2004. **29**(21): p. 2503-2505.

166. Shannon, C.E., *Communication theory of secrecy systems. 1945.* M.D. computing : computers in medical practice, 1998. **15**(1): p. 57-64.
167. Kilpatrick, J.M., et al., *Measurement of complex surface deformation by high-speed dynamic phase-stepped digital speckle pattern interferometry.* Optics Letters, 2000. **25**(15): p. 1068-1070.
168. Creath, K., *Phase-measurement interferometry techniques.* Progress in optics, 1988. **26**(26): p. 349-393.
169. Creath, K., *Phase-shifting speckle interferometry.* Applied Optics, 1985. **24**(18): p. 3053-3058.